



---

Johannes Gutenberg–Universität  
Mainz  
Institut für Kernphysik

---



# Study of the Helicity Dependence of Single Pion Photoproduction on the Deuteron

Ph.D. Thesis  
of  
Mauricio Martínez Fabregate  
Born in Valencia  
(Spain)

May 8, 2007

*Tag der mündlichen Prüfuns: 18. Juli 2007*

*Dedicado a Cris,  
mi Frau*

## Abstract

The first experimental test of the GDH sum rule on the proton was carried out in 1998 at the MAMI accelerator facility in Mainz University. A pilot experiment with a polarized deuteron target was also performed. In 2003 the same collaboration carried out a dedicated experiment on the deuteron with the aim to investigate the GDH sum rule on the neutron. The setup used in both experiments allows not only to measure total cross sections, but also to study partial reaction channels.

In this thesis, data from the 1998 pilot experiment on the deuteron are analyzed. A study of the helicity dependence of the differential cross section on three single pion photoproduction channels on the deuteron in the upper half of the  $\Delta$ -resonance will be presented. These results are compared with a theoretical model. A reasonably good agreement was obtained for unpolarized reactions, while some small discrepancies are observed in the polarized channels.

The target degree of polarization is one of the relevant parameters required for an absolute normalization of the cross section. The analysis of this parameter for the 2003 data is given in this work.

A Frozen Spin Target is under construction in Mainz. It will be used with the Crystal Ball detector and it will provide a polarized proton and polarized deuteron target for future experiments. The preparation of the different subsystems needed for the setup was an important part of this thesis. The basic principles of this technique and the actual status of the target will be presented in some detail.

## Zusammenfassung

Der erste experimentelle Test der GDH-Summenregel für das Proton wurde 1998 am MAMI-Beschleuniger der Universität Mainz durchgeführt. Ferner wurde ein Pilot-Experiment mit einem polarisierten Deuteron-Target vorgenommen. Dieselbe Kollaboration führte 2003 ein auf das Deuteron ausgerichtetes Experiment durch mit der Absicht, die GDH-Summenregel für das Neutron zu untersuchen. Der in beiden Experimenten verwendete Aufbau erlaubt nicht nur die Messung des totalen Wirkungsquerschnitts, sondern auch gleichzeitig einzelne Teilreaktionen zu studieren.

In dieser Arbeit werden die Daten des Deuteron-Pilot-Experiments von 1998 analysiert. Desweiteren wird eine Studie der Helizitätsabhängigkeit der differentiellen Wirkungsquerschnitte für drei Pion-Photoproduktionskanäle des Deuterons in der oberen Hälfte der  $\Delta$ -Resonanz präsentiert. Diese Ergebnisse werden mit einem theoretischen Modell verglichen. Dabei wurde eine hinreichend gute Übereinstimmung für die unpolarisierten Reaktionen gefunden, während für die polarisierten Kanäle kleinere Diskrepanzen beobachtet wurden.

Der Targetpolarisationsgrad ist einer der relevanten Parameter, der für eine absolute Normalisierung der Wirkungsquerschnitte notwendig ist. Die Analyse dieses Parameters für die 2003er Daten wird in der vorliegenden Arbeit vorgestellt.

Zur Zeit ist in Mainz ein Frozen-Spin-Target im Bau. Es wird als Target für polarisierte Protonen oder polarisierte Deuteronen für zukünftige Experimente mit dem Crystal Ball zur Verfügung stehen. Die Vorbereitungen der verschiedenen Subsysteme dieses Aufbaus stellten einen wichtigen Teil dieser Arbeit dar. Die fundamentalen Grundlagen der Methode und deren technische Umsetzung, sowie der momentane Status der Aufbauarbeiten am Target werden im Detail präsentiert.



# Contents

---

---

<b>1</b>	<b>Introduction</b>	<b>1</b>
1.1	Historical Context . . . . .	1
1.2	Outline . . . . .	4
<b>2</b>	<b>Theoretical Model</b>	<b>7</b>
2.1	Introduction . . . . .	7
2.2	Kinematic Formalism . . . . .	9
2.3	The Transition Matrix . . . . .	10
2.4	The Differential Cross Section Including Polarization Symmetries . . . . .	12
2.5	Semiexclusive Differential Cross Section for Three Specific Reaction Channels	13
2.5.1	Differential Cross Section of the $\vec{\gamma} + \vec{d} \rightarrow n + p + \pi^0$ Reaction . . .	14
2.5.2	Differential Cross Section of the $\vec{\gamma} + \vec{d} \rightarrow n + n + \pi^+$ Reaction . . .	14
2.5.3	Differential Cross Section of the $\vec{\gamma} + \vec{d} \rightarrow p + p + \pi^-$ Reaction . . .	15
<b>3</b>	<b>Experimental Setup</b>	<b>17</b>
3.1	Introduction . . . . .	17
3.2	The Photon Beam . . . . .	18
3.2.1	MAMI . . . . .	18
3.2.2	Glasgow-Mainz Tagger Spectrometer . . . . .	19
3.2.3	Photon Flux . . . . .	21
3.2.4	Møller Polarimetry . . . . .	22
3.3	Detector Setup . . . . .	25
3.3.1	DAPHNE Detector . . . . .	27
3.3.2	MIDAS Detector . . . . .	30
3.3.3	Čerenkov Detector . . . . .	32

---

3.3.4	Forward Components . . . . .	32
3.3.5	Data Acquisition . . . . .	33
3.4	Unpolarized Target . . . . .	34
3.5	Theoretical Principles of the Frozen Spin Target Technique . . . . .	35
3.5.1	Thermal Equilibrium Polarization . . . . .	35
3.5.2	Dynamical Nuclear Polarization . . . . .	37
3.5.3	Nuclear Magnetic Resonance Technique . . . . .	41
3.5.4	Frozen Spin Target Principle . . . . .	46
3.5.5	Cryostat . . . . .	47
3.5.6	Superconductivity . . . . .	54
3.6	The Bonn Frozen Spin Target . . . . .	56
3.6.1	Target Material . . . . .	56
3.6.2	Refrigerator . . . . .	56
3.6.3	Polarizing Magnet . . . . .	57
3.6.4	Internal Holding Coil . . . . .	57
3.6.5	Microwave System . . . . .	58
3.6.6	NMR System . . . . .	58
3.6.7	Control System . . . . .	59
3.7	The Mainz Frozen Spin Target . . . . .	59
3.7.1	Refrigerator . . . . .	59
3.7.2	Polarizing Magnet . . . . .	65
3.7.3	Microwaves System . . . . .	67
3.7.4	NMR System . . . . .	70
3.7.5	Control System . . . . .	70
3.8	Analysis of the Target Polarization in the GDH Experiment 2003 . . . . .	77
3.8.1	Polarization Analysis . . . . .	78
3.8.2	Error Calculations . . . . .	79
3.8.3	Results . . . . .	80
<b>4</b>	<b>Analysis</b>	<b>83</b>
4.1	Introduction . . . . .	83
4.2	Target Parameters . . . . .	85
4.3	Number of Selected Events . . . . .	86
4.4	General Geometrical Conditions . . . . .	87



4.4.1	Polar Angular Acceptance . . . . .	87
4.4.2	Azimuthal Angular Acceptance . . . . .	88
4.4.3	Definition of the Target Geometry . . . . .	89
4.4.4	Effective Target Length . . . . .	91
4.4.5	Random Subtraction . . . . .	92
4.5	Energy Binning . . . . .	94
4.6	Identification Methods for Charged Particles . . . . .	94
4.6.1	The $\Delta E/E$ -Method . . . . .	94
4.6.2	The Range Fit Method . . . . .	96
4.6.3	The Geometrical Range Method . . . . .	98
4.7	Partial Channel Analysis . . . . .	100
4.8	Analysis of the $\gamma + d \Rightarrow p_{spect} + p + \pi^-$ Reaction . . . . .	101
4.9	Analysis of the $\gamma + d \Rightarrow n_{spect} + n + \pi^+$ Reaction . . . . .	103
4.10	Analysis of the $\gamma + d \Rightarrow n_{spect} + p + \pi^0$ Reaction . . . . .	104
4.11	Analysis of the Double Polarization Data . . . . .	105
4.12	Detector Simulation . . . . .	105
4.13	Systematic Errors . . . . .	106
<b>5</b>	<b>Results</b>	<b>109</b>
5.1	Introduction . . . . .	109
5.2	Unpolarized Channels . . . . .	110
5.2.1	Results of the $\gamma + d \Rightarrow p_{spect} + p + \pi^-$ Reaction . . . . .	110
5.2.2	Results of the $\gamma + d \Rightarrow n_{spect} + n + \pi^+$ Reaction . . . . .	110
5.2.3	Results of the $\gamma + d \Rightarrow n_{spect} + p + \pi^0$ reaction . . . . .	110
5.3	Polarized Channels . . . . .	111
5.3.1	Results of the Polarized $\vec{\gamma} + \vec{d} \Rightarrow p_{spect} + p + \pi^-$ Reaction . . . . .	111
5.3.2	Results of the Polarized $\vec{\gamma} + \vec{d} \Rightarrow n_{spect} + n + \pi^+$ Reaction . . . . .	112
5.3.3	Results of the Polarized $\vec{\gamma} + \vec{d} \Rightarrow n_{spect} + p + \pi^0$ Reaction . . . . .	112
5.4	Unpolarized Results . . . . .	113
5.5	Polarized Results . . . . .	120
<b>6</b>	<b>Conclusions and outlook</b>	<b>127</b>
6.1	Conclusions . . . . .	127
6.2	Outlook . . . . .	128



---

---

# Chapter 1

## Introduction

---

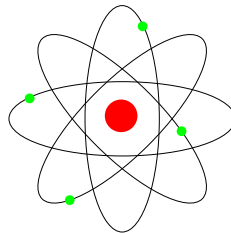
---

*Neo, sooner or later,  
you are going to realize just as I did...  
there is a difference between knowing the path  
and walking the path.*

Morpheus, The Matrix.

### 1.1 Historical Context

The first nuclear scattering experiment was performed by Geiger and Marsden in 1909 and explained by Rutherford two years later with his nowadays very popular atomic model. In this model, that every child learns at school, the positive nucleus contains most of the atomic mass and is surrounded by the negatively charged electrons. Since this time our knowledge about the atom and the nucleus has greatly increased. High energetic and exotic beams, many different and complex targets together with new detectors have been developed since this time, while the original idea of shooting on a target with a beam in order to look inside the matter remains unchanged.



In the last century some historical experiments and theoretical works have been developed and modified our understanding of nuclear matter.

Deuterium was predicted in 1926 by Walter Russell and first detected in late 1931 by Harold Urey. The existence of deuterium is one of the arguments in favor of the big bang theory. Stellar fusion destroys deuterium, and there are no known natural processes other than the big bang nucleosynthesis, which might have produced it at anything close to the observed natural abundance. Nowadays it is used in nuclear fusion reactions. The discovery of deuterium, that took place even before the discovery of the neutron in 1932, was an experimental shock to theory. The deuterium is a very interesting object by itself, and understanding it better could help for the understanding of the origin of the universe and to find new sources of energy. In addition, since it is the simplest bound nucleus, it can be used as a neutron target in scattering experiments in order to obtain information about the nucleon structure and the nuclear interaction.

The measurement of the nuclear magnetic moment of the proton in 1933 showed that it is not a point-like particle, but it possesses a complex internal structure. The theoretical work of Yukawa predicted in 1935 the existence of the  $\pi$ -meson as the interacting boson of the strong force. This meson was later discovered in 1946 by Powell from cosmic rays. The pion plays an important role in the study of the nucleon internal structure as it will be shown later in this thesis.

In the fifties and sixties, thanks to the development of the big accelerator facilities, a lot of new particles were discovered. In 1964 the theoretical work of Gell-Mann and Zweig with their quark model could put some order into the "zoo of nuclear particles". Nowadays the standard model explains most of the effects seen in the experiments. The matter is divided into hadrons, like the proton or the neutron, and leptons, like the electron. The hadrons are formed by quarks. There are two sub-groups: the baryons, composed by three quarks, and the mesons, containing a quark-antiquark pair. The quarks and the leptons are divided into three families. Today, as far as we know, both quarks and leptons are believed to be point-like particles without internal structure.

The theory that explains the nuclear strong interaction of the quarks is the quantum chromodynamics (QCD). This is the most successful theory that has been developed up to now, and it has been tested with very high precision in many experiments. Unfortunately, the perturbative approach used at high energies is applicable at high momentum transfer only, where the interaction strength is relatively weak, and cannot be used at energies comparable to the proton mass. Hence, up to now, the QCD theory can not fully explain the static properties of the nucleon from its constituent quarks.

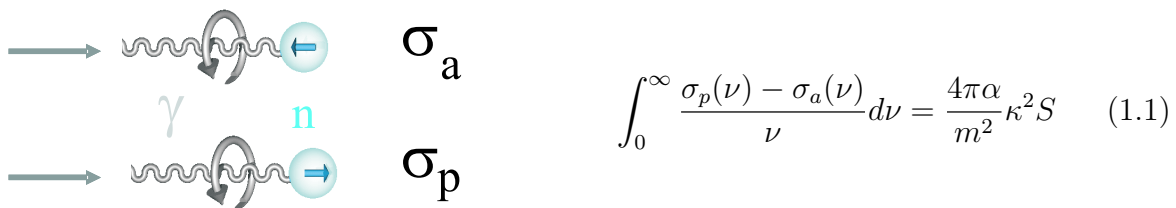
In this medium energy region many models based on the effective degrees of freedom have been developed. A completely model-independent partial wave analysis for pseudoscalar meson photoproduction will require the measurement of seven observables: the differential cross section, three single polarization observables (beam asymmetry, target asymmetry and recoil nucleon polarization) and three independent double polarization observables. Until now not enough "doubly polarized" data have been measured, hence this lack must be compensated by additional model dependent constraints. In this thesis

new data from doubly polarized experiments will be presented. As it will be shown, the development of new target techniques is important to obtain these double polarization observables.

In 1987 an experiment performed at CERN by the EMC [Ash88] showed that the three constituent quarks carry only 30% of the spin of the nucleon. This puzzling result, that was corroborated by many other experiments at CERN (EMC [Ash89] and SMC [Ada97] [Ade98]), SLAC ([Ant96], [Abe98] and [Abe97]) and DESY ([Ack98] and [Air98]), tells us that our understanding of the nucleon structure is still incomplete. This was called the spin crisis. The nucleon is composed of not only the three constituent quarks and the gluons that they exchange, but also of sea-quarks that come in quark-antiquark pairs and gluons that are constantly being created and annihilated. The HERMES experiment [Ack99] has shown that the sea-quark contribution to the nucleon spin is negligible. Some evidence is arising for a gluon contribution to the nucleon spin, which could solve this crisis [Air00].

In these experiments the nucleon spin structure is studied using polarized lepton scattering on the nucleon. The theoretical description is done by using the spin structure function, primarily the  $g_1(x)$  function, where  $x$  is the Bjorken scaling variable. In the sixties and seventies several sum rules based on general assumptions have been deduced for  $g_1(x)$ . Two examples are the Bjorken sum rule, experimentally verified within 10%, and the Ellis-Jaffe sum rule, where the experimental data show significant disagreement with the predicted values.

In the case of real photon absorption on the nucleon the Gerasimov-Drell-Hearn (GDH) sum rule is of special interest. It relates static properties of the nucleon like its mass  $m$ , spin  $S$  and anomalous magnetic moment  $\kappa$  to its dynamical structure. It can be measured by studying the scattering of circularly polarized photons on longitudinally polarized nucleons. Depending on the relative orientation a parallel,  $\sigma_p$ , and an anti-parallel,  $\sigma_a$ , cross section can be defined. The GDH sum rule reads:



$$\int_0^\infty \frac{\sigma_p(\nu) - \sigma_a(\nu)}{\nu} d\nu = \frac{4\pi\alpha}{m^2} \kappa^2 S \quad (1.1)$$

where  $\nu$  is the energy of the incoming photon and  $\alpha$  the fine structure constant.

This sum rule was first derived for the proton by Gerasimov in 1966 [Ger66], and independently by Drell and Hearn [Dre66] the same year. Later it was generalized to any spin particle ([Sai69] and [Fri77]). It is model independent and based on very basic principles, like Lorentz and gauge invariance, causality, unitarity, Low's theorem and

on the generally accepted no-subtraction hypothesis. Due to a lack in technology this sum rule could not be tested until 30 years later. In 1993 an international GDH sum rule collaboration was founded with the participation of many universities and research centers around the world, and some experiments in different facilities were proposed. In 1998 the first measurement of the GDH integrand was performed at the MAMI facility in Mainz with photon energies from 200 up to 800 MeV ([Ahr00] and [Ahr01]). In 2001 and 2002 another experiment carried out at the ELSA accelerator in Bonn studied the sum rule from 800 MeV up to 3 GeV ([Dut03], [Dut04] and [Dut05]). In 2003 a second experiment at Mainz was done, but this time focusing on the deuteron. The main goal was to learn about the sum rule on the deuteron and try to obtain the neutron contribution.

The GDH experiments of 1998 and 2003 at Mainz were performed using the DAPHNE detector, which allows partial channel analysis. This is very useful for discriminating between theoretical models, that predict different contributions of the partial channels to the total cross section.

Within this context, this thesis has three main points of interest. First, some partial channel analysis of the data from the polarized and unpolarized deuteron target taken during the GDH sum rule pilot experiment carried out at Mainz in 1998 was made. Second, the target polarization analysis corresponding to the 2003 GDH experiment will be presented. The target degree of polarization is of major importance since it contributes directly not only to the GDH sum rule evaluation, but also to the partial channels. The analysis of this target degree of polarization is one of the primary results of this work. Last, but not least, the actual status of the new polarized frozen spin target that is being built in Mainz will be explained in some detail. This target will offer the opportunity to perform doubly polarized experiments, using the Crystal Ball detector setup, that will bring new information about the internal structure of the nucleon. The preparations for this target were one of the main works of this thesis.

## 1.2 Outline

In this work new data from doubly polarized experiments will be presented. Using the circularly polarized photon beam from the MAMI facility and the Bonn frozen spin proton target the first test of the GDH sum rule was carried out at Mainz in 1998 . The main objectives of the experiment were to investigate the GDH sum rule on the proton and to study of the helicity dependence cross section of the different partial channels. In addition a pilot experiment on the deuteron was performed. Using the DAPHNE detector, partial channel analysis can be done. In this thesis three unpolarized and polarized partial channels on the single pion photoproduction on the deuteron in the upper half of the  $\Delta$ -resonance will be studied:

$$\begin{aligned}\gamma + d &\Rightarrow p_{spect} + p + \pi^- \\ \gamma + d &\Rightarrow n_{spect} + n + \pi^+ \\ \gamma + d &\Rightarrow n_{spect} + p + \pi^0\end{aligned}$$

In the last 50 years some theoretical models of the pion photoproduction on the deuteron have been developed (see section 2.1). The data obtained in this thesis will be compared with the latest calculation based on the model of A. Fix and H. Arenhövel [Fix05].

The development of a polarized target is technically one of the most challenging parts in building up an experiment to test the GDH sum rule. Currently, a new frozen spin target is being developed in Mainz. It could be used either as polarized proton or deuteron target. This will give us the opportunity to study not only the nucleon structure but also the nuclear interaction. In addition, investigations on target material properties, or development of new materials can be performed. Together with polarized beam and recoil polarimeter this target will offer the possibility to carry out a complete pion photoproduction experiment in the next years.

In the second chapter of this thesis the theoretical model of the pion photoproduction on the deuteron developed by A. Fix and H. Arenhövel, that will be compared with the data obtained in the 1998 GDH pilot experiment, is presented. The setup of this experiment is presented in chapter 3. The Bonn polarized frozen spin target will be described in some details. Additionally the actual status of the new Mainz polarized frozen spin target is extensively explained. This chapter finishes showing the analysis of the target polarization of the 2003 GDH experiment carried out at Mainz. Chapter 4 is devoted to the analysis procedure used to extract the data. The results of the polarized and unpolarized channels are presented in chapter 5, and compared with the theoretical model explained in chapter 2. The thesis finishes with conclusions and an outlook.





---

---

# Chapter 2

## Theoretical Model

---

---

*We should consider every day lost  
on which we have not danced at least once.  
And we should call every truth false  
which was not accompanied by at least one laugh.*

Friedrich Nietzsche.

### 2.1 Introduction

Pion photoproduction on the deuteron has many complementary points of interest. First of all it is an excellent tool for the study of nucleon resonances. On the other hand its small binding energy offers the opportunity to study the elementary reaction on the neutron. Since no free neutron target is available the deuteron can be used as an effective neutron target. A prerequisite for this is that one has reliable control of the off-shell and medium effects. It can provide information about the influence of the nuclear environment on the elementary production amplitude. Last but not least, since it is the simplest nucleus it can provide a lot of information about the nucleon interaction. In the last years new technological developments have opened the opportunity to perform a new generation of experiments with much more accurate data and including spin-dependent observables.

The pion photoproduction on the free nucleon has been studied in the last fifty years. Kroll and Ruderman [Kro54] were the first to derive model-independent predictions in the threshold region, so-called low-energy theorems (LET), by applying gauge and Lorentz invariance to the reaction  $\gamma N \rightarrow \pi N$ . The general formalism for this process was developed by Chew *et al.* [Che57] (CGLN-amplitudes). Fubini *et al.* [Fub65] extended the predictions of LET by including also the hypothesis of a partially conserved axial current (PCAC). Berends *et al.* [Ber67] analyzed the existing data in terms of multipole decomposition and presented tables of the various multipole amplitudes constructed in the region up to

excitation energies of 500 MeV.

For many years the model of Olsson and Osypowski ([Ols75] and [Ols78]) has been the standard model for pion photoproduction on the nucleon. In practice a model that has been more extensively used for comparison with data is the one of Blomqvist and Laget [Blo77], which is a non-relativistic reduction of the model of Olsson and Osypowski. It uses a different parametrization for neutral and charged pion photoproduction and it gives a satisfactory description of the charged pion data, but not of the neutral channel. In 1990 Nozawa *et al.* [Noz90] proposed a new model for pion photoproduction on the nucleon in the  $\Delta$ -region.

First investigations on photoproduction of pions on the deuteron go back to the fifties ([Che51] and [Lax52]). In the seventies a more systematic calculation of pion photoproduction on the deuteron was done by Blomqvist and Laget ([Blo77], [Lag77], [Lag78] and [Lag82]). They studied the influence of pion rescattering ( $\pi N$ ) and nucleon-nucleon (NN) final state interaction (FSI). These calculations are in good agreement with experimental data of Benz *et al.* [Ben77] in the  $\gamma d \rightarrow \pi^- pp$  reaction. They found that the final state interaction effects are small for the charged pion photoproduction reactions in comparison with the neutral channel.

Schmidt *et al.* [Sch96] also studied the pion photoproduction on the deuteron in the impulse approximation, but neglecting all kinds of final state interactions and other two body operators. This prediction does not provide a good description of the experimental data on the  $\pi^-$ , neither on the  $\pi^0$  photoproduction data of Krusche *et al.* [Kru99]. This reinforces the idea that the effect of NN rescattering is important in the incoherent pion photoproduction, especially for the neutral channel.

Levchuk *et al.* [Lev96] studied the  $d(\gamma, \pi^0)np$  reaction using the photoproduction operator of Blomqvist and Laget, and they found a good agreement with the results of the Laget model. Later, Levchuk *et al.* [Lev00] modified their calculations using a more realistic elementary production operator and including the charged pion production channels. The elementary production operator is taken in on-shell form and calculated using the SAID [Arn02] and MAID [MAID] multipoles analysis. They include the  $NN$  and  $\pi N$  rescattering in the final state. The influence of NN FSI was confirmed, and good agreement with experimental data was achieved.

The effect of  $\pi N$  rescattering and nucleon-nucleon interaction on polarization observables has been investigated in [Lev96] for the GDH sum rule in the  $\pi^0$  channel, as well as in [Log00] for target asymmetries in the  $\pi^-$  reaction. Subsequently, various polarization asymmetries of the semiexclusive differential cross section were studied by Darwish *et al.* [Dar03].

Recently, A.Fix and H. Arenhövel [Fix05] have presented a work on the incoherent pion photoproduction on the deuteron including polarization observables. It uses an elementary production operator from the MAID model. In this work the role of the nucleon-nucleon

( $NN$ ) and pion-nucleon ( $\pi N$ ) final state interaction, and the importance of polarization observables are studied. This model will be compared with the experimental data obtained in this thesis. In the next section a brief description of the model is given, for more details refer to [Fix05]. At the end of the chapter the necessary modifications to properly compare model and data are explained.

## 2.2 Kinematic Formalism

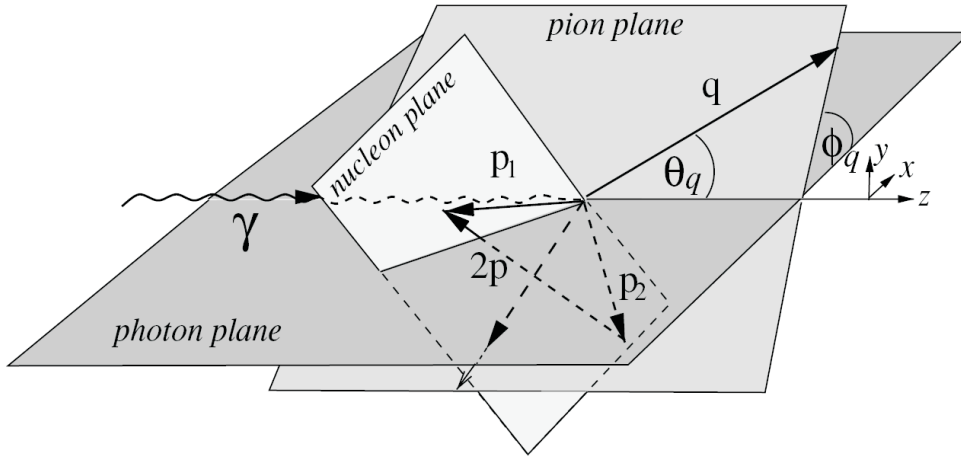


**Figure 2.1:** Kinematics of the pion photoproduction on the deuteron in the laboratory frame.

First of all, we consider the kinematic formalism of the pion photoproduction on the deuteron:

$$\gamma(k, \vec{\varepsilon}_\mu) + d(p_d) \rightarrow \pi(q) + N_1(p_1) + N_2(p_2) \quad (2.1)$$

where as standard notation  $k$ ,  $p_d$ ,  $q$ ,  $p_1$  and  $p_2$  are the four-momenta of photon, deuteron, pion, first and second nucleon respectively. The circular polarization vector of the photon is denoted by  $\vec{\varepsilon}_\mu$  with  $\mu = \pm 1$ . The following mathematical developments will not depend on the reference frame, however for explicit applications and comparison with experimental data the laboratory frame is used. The independent variables chosen for the description of the final state are, in general, the outgoing pion momentum  $\vec{q} = (q, \theta_q, \phi_q)$  and the spherical angles  $\Omega_p = (\theta_p, \phi_p)$  of the relative momentum  $\vec{p} = (\vec{p}_1 - \vec{p}_2)/2 = (p, \Omega_p)$  of the two outgoing nucleons. For specific channels other variables can be chosen, as it will be

explained in section 2.5. The coordinate system is chosen as right handed with the z-axis along the photon momentum  $\vec{k}$ .

In general, three planes can be defined:

(i) *the photon plane* spanned by the photon momentum and the direction of maximal linear photon polarization, which defines the direction of the x-axis,

(ii) *the pion plane*, spanned by the photon and pion momenta, which intersects the photon plane along the z-axis with an angle  $\phi_q$ ,

(iii) *the nucleon plane* spanned by the momenta of the two outgoing nucleons intersecting the pion plane along the total momentum of the two nucleons.

Fig.2.1 illustrates these planes for the laboratory frame. In section 2.5 it will be shown that for particular channels some other plane definitions can be more useful. In the case where the linear photon polarization vanishes, one can choose  $\phi_q = 0$ , then the photon and pion planes are the same.

## 2.3 The Transition Matrix

All observables are determined by the T-matrix elements of the electromagnetic pion production current  $\vec{J}_{\gamma\pi}$  between the initial deuteron and the final  $\pi NN$  states. In a general frame it is given as:

$$T_{sm_s, \mu m_d} = -^{(-)} \langle \vec{p}_1 \vec{p}_2 sm_s, \vec{q} | \vec{\varepsilon}_\mu \cdot \vec{J}_{\gamma\pi}(0) | \vec{p}_d 1m_d \rangle \quad (2.2)$$

where  $s$  and  $m_s$  denote the total spin and its projection on the relative momentum  $\vec{p}$  of the outgoing two nucleons, and  $m_d$  is correspondingly the deuteron spin projection on the z-axis as quantization axis.

For the calculations of the T-matrix first the impulse approximation (IA), which describes the photoproduction of the pion on one nucleon while the other acts as a spectator, is considered. Later the contributions of the  $NN$  and  $\pi N$  rescattering are added. Possible two-body contributions to the electromagnetic interaction are neglected. The T-matrix is given by the sum of all these contributions:

$$T_{sm_s, \mu m_d} = T_{sm_s, \mu m_d}^{IA} + T_{sm_s, \mu m_d}^{NN} + T_{sm_s, \mu m_d}^{\pi N} \quad (2.3)$$

On one side, the IA contribution can be written as:

$$\begin{aligned} T_{sm_s, \mu m_d}^{IA} &= \langle \vec{q}, \vec{p}, sm_s | [t_{\gamma\pi}(1) + t_{\gamma\pi}(2)] | 1m_d \rangle \\ &= \sum_{m'_s} [\langle sm_s | \langle \vec{p}_1 | t_{\gamma\pi}(W_{\gamma N_1}) | - \vec{p}_2 \rangle \phi_{m'_s m_d}(\vec{p}_2) | 1m'_s \rangle - (1 \leftrightarrow 2)] \end{aligned}$$

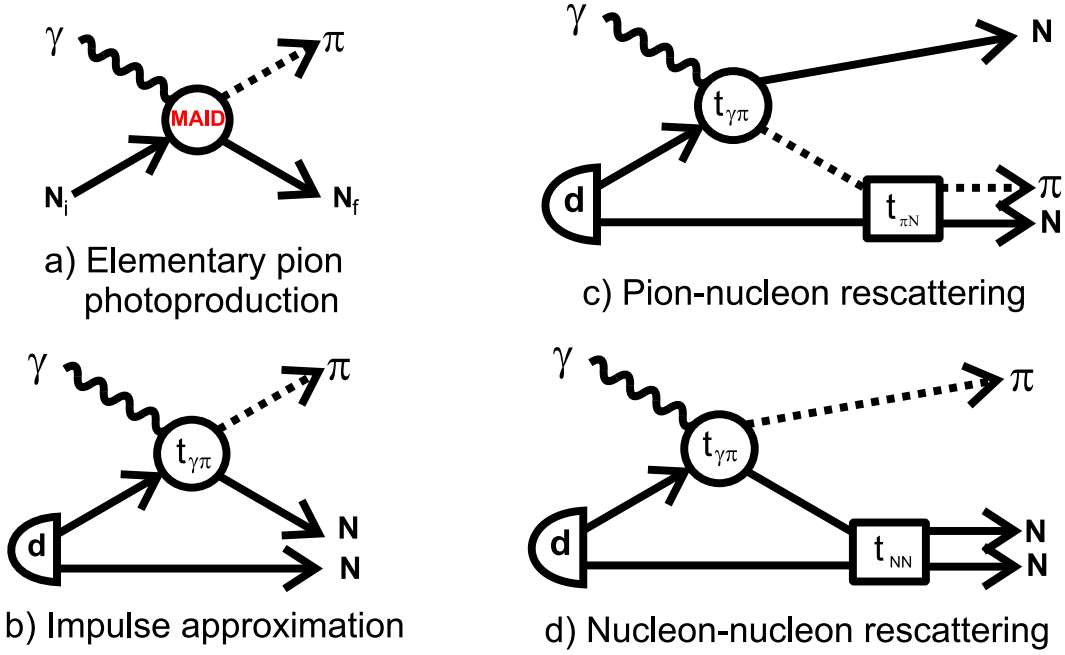


**Figure 2.2:** Feynman diagrams taken into account by the model. a) The elementary pion photoproduction. b) The impulse approximation in which the photon interacts with one nucleon in the deuteron while the other acts as spectator. c) The pion-nucleon rescattering. d) The nucleon-nucleon rescattering.

where  $t_{\gamma\pi}$  denotes the elementary pion photoproduction operator, which is taken from the MAID model [MAID],  $W_{\gamma N_1}$  is the invariant energy of the  $\gamma N$  system, and  $\phi_{m'_s m_d}$  is related to the internal deuteron wave function in momentum space by:

$$\begin{aligned} \langle \vec{p}, 1m_s | 1m_d \rangle &= \phi_{m'_s m_d} \\ &= \sum_{L=0,2} \sum_{m_L} i^L (L m_L 1 m_s | 1 m_d) u_L(p) Y_{L m_L}(\hat{p}) \end{aligned}$$

On the other hand, the nucleon-nucleon and pion-nucleon rescattering contributions have a similar structure:

$$T_{sm_s, um_d}^{NN} = \langle \vec{q}, \vec{p}, sm_s | t_{NN} G_{NN} [t_{\gamma\pi}(W_{\gamma N_1}) + t_{\gamma\pi}(W_{\gamma N_2})] | 1m_d \rangle \quad (2.4)$$

$$T_{sm_s, um_d}^{\pi N} = \langle \vec{q}, \vec{p}, sm_s | t_{\pi N} G_{\pi N} [t_{\gamma\pi}(W_{\gamma N_1}) + t_{\gamma\pi}(W_{\gamma N_2})] | 1m_d \rangle \quad (2.5)$$

where  $t_{NN}$  and  $t_{\pi N}$  denote the nucleon-nucleon and the pion-nucleon scattering matrices respectively.  $G_{NN}$  and  $G_{\pi N}$  are the corresponding free two-body propagators. Fig.2.2 shows the Feynman diagrams of the elementary pion photoproduction and the three mechanisms taken into account.

For the calculation of the  $NN$ -rescattering contribution the realistic Paris potential ([Hai84] and [Sch85]) was chosen. All partial waves up to  ${}^3D_3$  were included. The deuteron wave function was also calculated with this potential. The  $\pi N$  rescattering is evaluated using the model of S. Nozawa *et al.* [Noz90], taking into account all partial waves up to  $l = 2$ . The elementary pion photoproduction amplitude is taken from the MAID2003 model.

## 2.4 The Differential Cross Section Including Polarization Symmetries

The general expression for the differential cross section reads:

$$\frac{d^5\sigma}{dq d\Omega_q d\Omega_p} = c(\omega, q, \Omega_q, \Omega_p) \text{tr}(T^\dagger T \rho_i) \quad (2.6)$$

where  $c(\omega, q, \Omega_q, \Omega_p)$  stands for the kinematic phase space factor,  $T$  denotes the reaction matrix and  $\rho_i$  the density matrix for the spin degrees of the initial system. The trace refers to all initial and final state spin degrees of freedom comprising incoming photon, target deuteron and final nucleons.

The density matrix  $\rho_i$  is a direct product of the density matrices  $\rho^\gamma$  of the photon and  $\rho^d$  of the deuteron:

$$\rho_i = \rho^\gamma \otimes \rho^d. \quad (2.7)$$

The photon density matrix has the form:

$$\rho_{\mu\mu'}^\gamma = (1 + \mu P_c^\gamma) \delta_{\mu\mu'} - P_l^\gamma \delta_{\mu, -\mu'} e^{2i\mu\phi_q} \quad (2.8)$$

where  $P_c^\gamma$  and  $P_l^\gamma$  are the degrees of circular and linear photon polarization respectively.

The corresponding deuteron density matrix  $\rho^d$  can be expressed in terms of irreducible spin operators  $\tau^{[I]}$  with respect to the deuteron spin space

$$\rho_{m_d m_d'}^d = \frac{1}{3} \sum_{IM} (-)^M \widehat{I} \langle 1m_d | \tau_M^{[I]} | 1m_d' \rangle P_{I-M}^d \quad (2.9)$$

where  $P_{00}^d = 1$  and  $P_{1M}^d$  and  $P_{2M}^d$  describe vector and tensor polarization components of the deuteron, respectively, that can be written as

$$P_{IM}^d(\vec{z}) = P_I^d e^{iM\phi_d} d_{M0}^I(\theta_d) \quad (2.10)$$

where  $d_{mm'}^j$  denotes the small rotation matrix [Ros57]. The deuteron target is characterized by four parameters, namely the vector and tensor polarization parameters  $P_1^d$  and  $P_2^d$ , respectively, and by the orientation angles  $\theta_d$  and  $\phi_d$  with respect to the coordinate system associated with the photon plane in the lab frame.

Using the definitions above mentioned and doing some calculations one finds the following expression of the differential cross section for the semiexclusive reaction  $\vec{d}(\vec{\gamma}, \pi)NN$  in which only the produced pion is detected:

$$\begin{aligned} \frac{d^3\sigma}{dq d\Omega_q} = \frac{d^3\sigma_0}{dq d\Omega_q} & \left[ 1 + P_I^\gamma \left\{ \tilde{\Sigma}^l \cos 2\phi_q + \sum_{I=0}^2 P_I^d \sum_{M=-I}^I \tilde{T}_{IM}^l \cos[\psi_M - \delta_{I1} \frac{\pi}{2}] d_{M0}^I(\theta_d) \right\} \right. \\ & \left. + \sum_{I=1}^2 P_I^d \sum_{M=0}^I \left( \tilde{T}_{IM}^0 \cos[M\phi_{qd} - \delta_{I1} \frac{\pi}{2}] + P_c^\gamma \tilde{T}_{IM}^c \sin[M\phi_{qd} + \delta_{I1} \frac{\pi}{2}] \right) d_{M0}^I(\theta_d) \right] \quad (2.11) \end{aligned}$$

where  $\phi_{qd} = \phi_q - \phi_d$ . In this expression  $\tilde{\Sigma}^l$  denotes the photon asymmetry for linearly polarized photons and unpolarized deuterons,  $\tilde{T}_{11}^0$  the target asymmetry for vector polarized deuterons and unpolarized photons,  $\tilde{T}_{2M}^0$  the target asymmetries for tensor polarized deuterons and unpolarized photons,  $\tilde{T}_{1M}^c$  the beam-target asymmetries for circularly polarized photons and vector polarized deuterons,  $\tilde{T}_{2M}^c$  the beam-target asymmetries for circularly polarized photons and tensor polarized deuterons,  $\tilde{T}_{1M}^l$  the beam-target asymmetries for linearly polarized photons and vector polarized deuterons, and  $\tilde{T}_{2M}^l$  the beam-target asymmetries for linearly polarized photons and tensor polarized deuterons. Explicit expressions of these asymmetries are listed in appendix of [Fix05].

Within the framework of this thesis three different pion photoproduction reactions were studied. The analysis procedure and results will be explained in chapters 4 and 5 respectively. In order to compare the presented model and the experimental data some small modification of equation 2.11 must be performed for each specific channel. The next section will explain these changes.

## 2.5 Semiexclusive Differential Cross Section for Three Specific Reaction Channels

The general form of the differential cross section  $d^3\sigma/dq d\Omega_q$  including beam and target degree of polarization is given in Eq. 2.11. Here we will write a differential cross section that can be better compared with the experimental data presented in this thesis. We consider a circularly polarized photon beam. Hence, there is no linear polarization contribution,

$P_l^\gamma = 0$ , and additionally  $\phi_q = 0$ . The target asymmetries for unpolarized photons  $\tilde{T}_{IM}^0$  do not cancel since the degree of photon polarization of the beam is not 100%, but it has an unpolarized contribution. The deuterium target is polarized parallel or antiparallel to the axis of the incoming photon beam, which means  $\theta_d = 0^\circ$  and  $\phi_d = 0^\circ$ , hence,  $\phi_{qd} = \phi_q - \phi_d = 0^\circ$ . Taking all this into account, and writing down the specific value of the d-functions [Ros57] in the case of  $\theta_d = 0^\circ$ , the differential cross section for the semiexclusive reaction  $\vec{\gamma} + \vec{d} \Rightarrow N + N + \pi$  in which only the pion is detected can be written as:

$$\frac{d^3\sigma}{dq d\Omega_q} = \frac{d^3\sigma_0}{dq d\Omega_q} \left( 1 + P_2^d \tilde{T}_{20}^0 + P_1^d P_c^\gamma \tilde{T}_{10}^c \right)$$

where there is a tensor and a vector polarization contribution, in addition to the unpolarized cross section. The tensor polarization term cancels with the helicity dependent differential cross section (Eq. 4.3) that will be studied in this thesis. In principle, measuring the cross section of both parallel and antiparallel orientations, as well as the unpolarized cross section the experimental value of the tensor polarization could be obtained. The main drawback in that in this measurement is that the unpolarized background has to be determined.

### 2.5.1 Differential Cross Section of the $\vec{\gamma} + \vec{d} \rightarrow n + p + \pi^0$ Reaction

In the case of the  $\pi^0$  channel only the proton is detected, not the pion. The mathematical formalism is the same, but replacing the pion by the proton. In Fig. 2.1 the *pion plane* will become the *proton plane* which is spanned by proton and photon momenta. The unmeasured neutron ( $p_1$ ) and the pion ( $q$ ) momenta span the *nucleon-pion plane*. In the expression 2.11 it would mean just to exchange the subindex  $q$  of the pion with the  $p_2$  of the measured proton.

$$q \longrightarrow p_2 \tag{2.12}$$

### 2.5.2 Differential Cross Section of the $\vec{\gamma} + \vec{d} \rightarrow n + n + \pi^+$ Reaction

In the  $\pi^+$  photoproduction channel only the pion trajectory is measured, but not its momentum. Then the corresponding differential cross section  $d^2\sigma/d\Omega_q$  is given by an expression formally analogous to Eq.2.11, in which the unpolarized cross section and asymmetries are replaced by:

$$\frac{d^3\sigma_0}{dq d\Omega_q} \longrightarrow \frac{d^2\sigma_0}{d\Omega_q} = \int_{q_{min}(\theta_q)}^{q_{max}(\theta_q)} dq \frac{d^3\sigma_0}{dq d\Omega_q} \tag{2.13}$$



$$\frac{d^3\sigma_0}{dq d\Omega_q} \tilde{T}_{IM}^\alpha(q, \theta_q) \longrightarrow \frac{d^2\sigma_0}{d\Omega_q} T_{IM}^\alpha(\theta_q) = \int_{q_{min}(\theta_q)}^{q_{max}(\theta_q)} dq \frac{d^3\sigma_0}{dq d\Omega_q} \tilde{T}_{IM}^\alpha(q, \theta_q), \alpha \in \{0, c\} \quad (2.14)$$

The upper and lower integration limits are given by:

$$q_{max}(\theta) = \frac{1}{2b} \left( a\omega \cos(\theta_q) + E_{\gamma d} \sqrt{a^2 - 4bm_\pi^2} \right) \quad (2.15)$$

$$q_{min}(\theta) = \max \left\{ 0, \frac{1}{2b} \left( a\omega \cos(\theta_q) - E_{\gamma d} \sqrt{a^2 - 4bm_\pi^2} \right) \right\} \quad (2.16)$$

where

$$a = W_{\gamma d}^2 + m_\pi^2 - 4m_N^2 \quad (2.17)$$

$$b = W_{\gamma d}^2 + \omega^2 \sin^2(\theta_q) \quad (2.18)$$

$$W_{\gamma d}^2 = m_d(m_d + 2\omega) \quad (2.19)$$

$$E_{\gamma d} = m_d + \omega \quad (2.20)$$

### 2.5.3 Differential Cross Section of the $\vec{\gamma} + \vec{d} \rightarrow p + p + \pi^-$ Reaction

For the  $\pi^-$  reaction channel the trajectory of the pion and the momentum of the proton are measured. The differential cross section equation is similar to the one for the  $\pi^+$  channel, but taking into account the measured momentum of the proton.



---

---

# Chapter 3

## Experimental Setup

---

---

*Nothing can add more power to your life  
than concentrating all your energies  
on a limited set of targets.*

Nido Qubein.

### 3.1 Introduction

This chapter will explain the main parts of the experimental setup used for the first GDH experiment performed at Mainz in 1998. The analysis of these data will be described in detail in the next chapter. The present chapter will also illustrate the actual status of the different parts of the new polarized frozen spin target (FST) that is currently being built in Mainz. At the end of the chapter the results of the analysis of the degree of polarization of the target for the 2003 nGDH experiment carried out in Mainz will be expounded.

In this chapter the photon beam produced via bremsstrahlung from the electrons accelerated in the MAMI microtron will be explained briefly. The Mainz-Glasgow tagger spectrometer is used to identify the energy of the photons. A lead glass and a pair detector give a precise and continuous measurement of the photon flux. The degree of polarization of the beam is obtained by a Møller polarimeter. The components of the detector setup will be presented: DAPHNE, MIDAS, Čerenkov, STAR and FFW. The two different target setups employed in the 1998 GDH experiment will be described. The first can be run as unpolarized hydrogen or deuterium target, while the frozen spin target uses butanol or deuterated butanol material as polarized proton or deuteron target. This work will focus on the deuterium and polarized deuterated butanol material since its data analysis will be presented as one result of this thesis.

Since the first GDH experiment was done in 1998 many PhD theses, Diploma theses and papers have described this setup. For this reason the present chapter will give a short

overview only, without going into details. For more information refer to [Bra99], [Hei00], [Ahr01], [Pre01], [Hol01], [Rov02], [Lang04], [Lan04], [Ros05], [Jah05] and the references therein.

## 3.2 The Photon Beam

### 3.2.1 MAMI

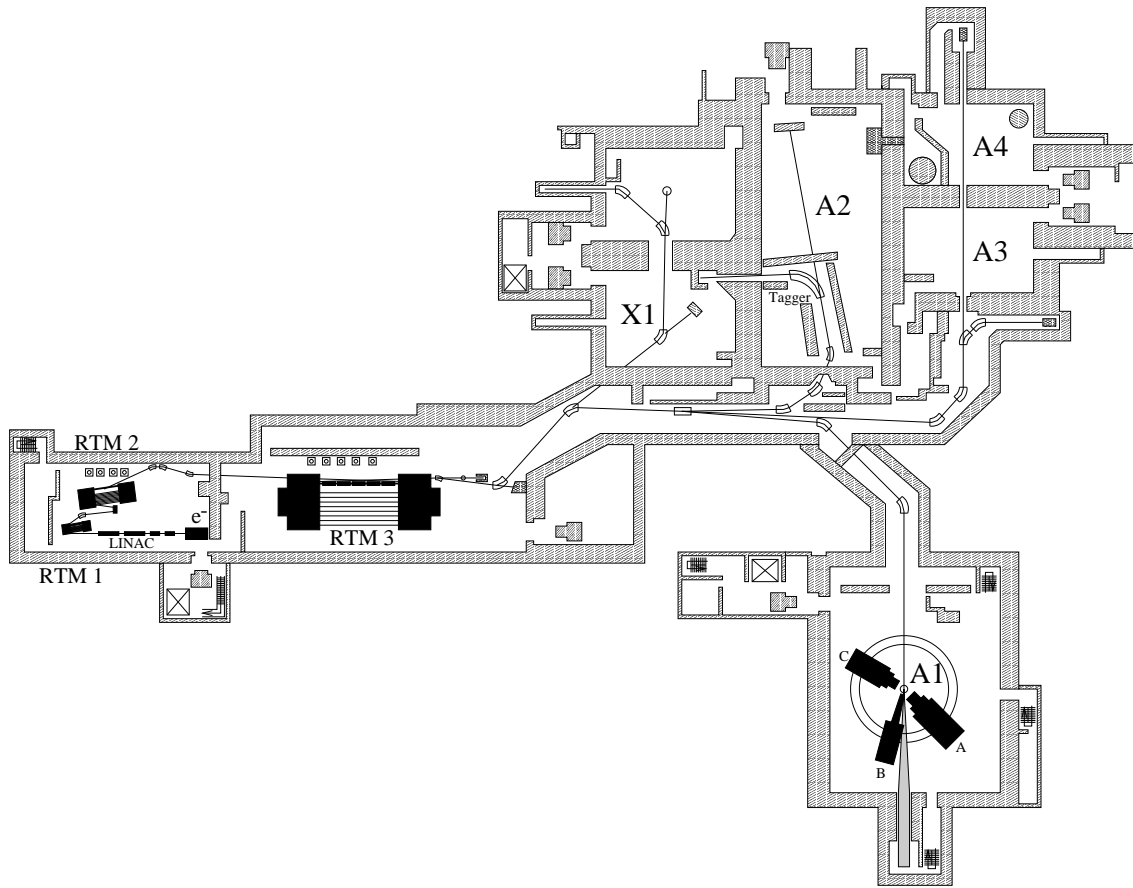


**Figure 3.1:** Floor plan of the MAMI-B accelerator facility.

The MAInz MIcrotron, MAMI ([Her76] and [Her89]), at the Institute for Nuclear Physics at the Johannes Gutenberg University, Mainz, was built in 1979. The first stage was MAMI-A1 where the exploitation of the microtron principle lead to a maximum electron energy of 14 MeV. It was followed by MAMI-A2 in 1983 when the 183 MeV

facility was put in operation. In 1991 MAMI-B was completed, producing electrons up to 855 MeV. The last upgrade, MAMI-C, was done in 2006. In December of this year a 1508 MeV electron beam was obtained after 43 turns in the new Harmonic Double Sided Microtron (HDSM). As the GDH measurements were performed at MAMI-B, we further concentrate on this version of the accelerator.

MAMI-B is a continuous wave electron accelerator with 100% duty cycle, a maximum current of 100  $\mu\text{A}$  and maximum energy of 855 MeV. A 3.5 MeV LINAC injects the electrons into a cascade of 3 Race Trace Microtrons (RTM), Fig. 3.1. The LINAC is fed either with 100 keV unpolarized electrons from a thermionic source, or with linearly polarized electrons originating from a  $\text{GaAs}_{0.95}\text{P}_{0.5}$  crystal photo-cathode which is irradiated by circularly polarized 830 nm laser light from a Titanium-Sapphire laser [Aul99]. The maximum current of the polarized source is 30  $\mu\text{A}$  with a degree of polarization of about 75%. During the experiment the direction of the polarization was changed every second in order to reduce systematic errors. Table 3.1 shows the important parameters of the 3 race track microtrons (RTM) and the new harmonic double sided microtron (HDSM). By extracting the electron from an intermediate recirculation trajectory of the last microtron (RTM3) the energy can be tuned as  $E_0 = 180 + 2n(7.5)\text{MeV}$  with  $n = 1, \dots, 45$ .

	RTM1	RTM2	RTM3	HDSM
Input energy (MeV)	3.455	14.35	179.5	854.6
Output energy (MeV)	14.35	179.5	854.6	1508.0
Recirculations	18	51	90	43
Energy gain per recirculation (MeV)	0.599	3.24	7.5	15.2

**Table 3.1:** MAMI RTM and HDSM parameters

### 3.2.2 Glasgow-Mainz Tagger Spectrometer

Once the electron beam leaves the RTM3 it is guided to the different experiment halls. In the A2 hall, where the GDH experiment was performed, the primary electron beam is converted into a photon beam via bremsstrahlung on a radiator foil. In the Coulomb field of radiator nuclei the electrons irradiate Bremsstrahlung photons. Typical radiator materials are nickel and aluminium. During the GDH experiment a polarized Vacoflux radiator was also employed. The produced photon beam is collimated towards the target and the detectors.

For the experiment it is a prerequisite to know the energy of the photon that induces the studied reaction. These photons are tagged by means of the Glasgow-Mainz photon tagging spectrometer ([Ant91] and [Hal96]). The technique for bremsstrahlung tagging

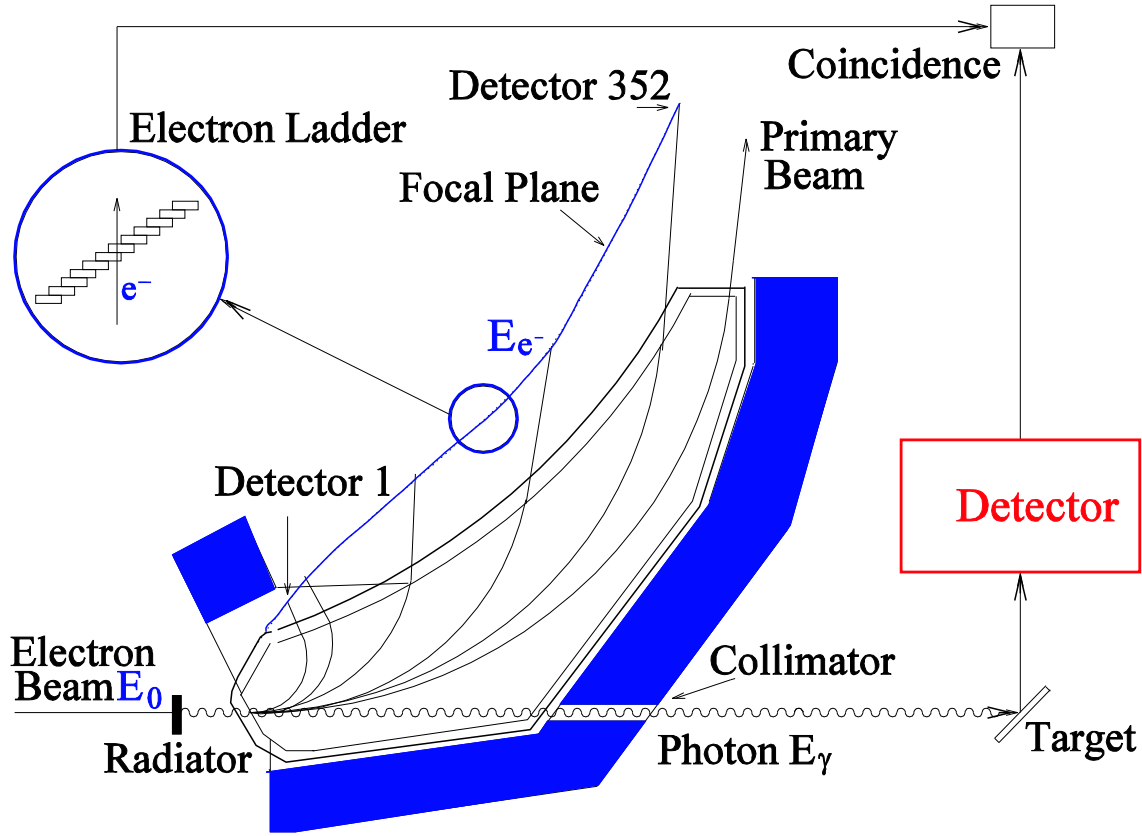


Figure 3.2: The Glasgow-Mainz Tagger.

is well established. Its most important features are the high photon flux and the good energy resolution that can be obtained.

Figure 3.2 shows a schematic diagram of the Glasgow-Mainz tagger. A homogeneous 1 Tesla dipole magnet bends the primary beam (electrons that did not interact with the radiator) to a Faraday cup, that is calibrated to monitor the electron beam current. The electrons that have radiated a photon possess less energy  $E_e$  and therefore the radii  $R$  of their bend trajectories are different:

$$R = \frac{E_e}{ecB} \quad (3.1)$$

where  $e$  is the electron charge,  $c$  the speed of light and  $B$  the magnetic field of the spectrometer. A set of 353 overlapping plastic detectors is positioned in the focal plane of the magnet. The overlap between neighboring detectors is used to generate coincidences between them in order to increase the energy resolution to 2 MeV and to minimize random signals. A coincident signal in 2 of these detectors will define the radius  $R$  of its trajectory

and therefore the energy of the electron  $E_e$ . Knowing the energy  $E_0$  of the primary electron beam from MAMI the energy of the tagged photon is:

$$E_\gamma = E_0 - E_e \quad (3.2)$$

The recoil energy of the nucleon in the bremsstrahlung process is negligible. The covered photon energy range for an electron beam of 855 MeV lies between 115 and 795 MeV. The bremsstrahlung photon spectrum is governed by a  $1/E_\gamma$  behavior. For the GDH experiment the tagger was operating at a tagged photon intensity of  $\sim 10^6$   $\gamma/s$ .

### 3.2.3 Photon Flux

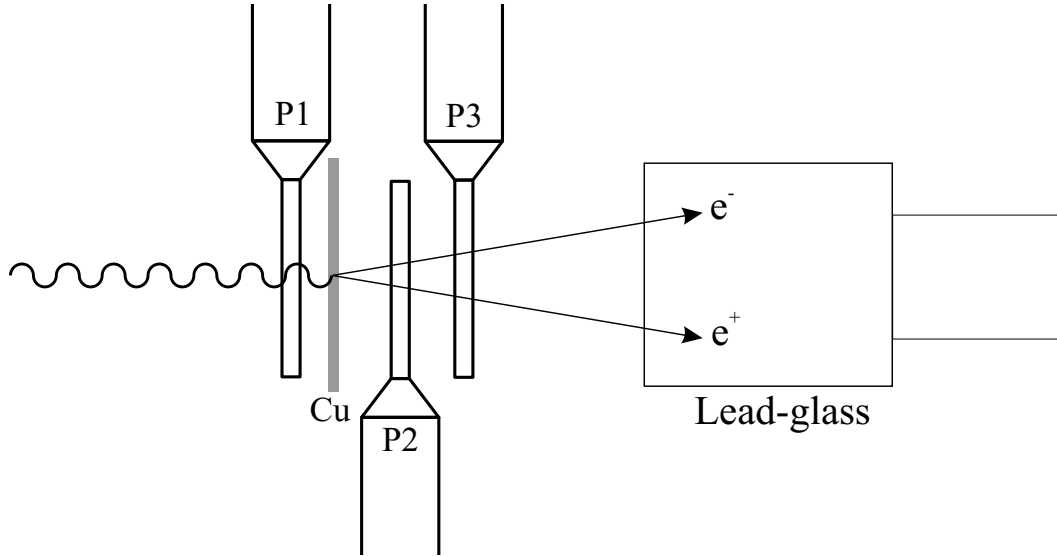


**Figure 3.3:** The pair and the lead glass detectors.

Only about 50% of the bremsstrahlung photons are emitted within the characteristic angle  $\Theta_c = m_e c^2/E_0$ . To obtain a well defined beam on the target cell, the photons need to be collimated at the tagger exit. Mainly due to the collimation the number of tagged photons hitting the target,  $N_\gamma$ , is smaller than the number of electrons measured by the focal plane detector,  $N_e$ , their ratio is defined as the tagging efficiency:

$$\varepsilon_{tagg} = \frac{N_\gamma}{N_e} \quad (3.3)$$

The tagging efficiency depends on the radius of the collimator, the initial electron energy  $E_0$  and the exact position and inclination of the beam, therefore, it is not constant in time and has to be monitored continuously in order to obtain the photon fluxes needed to calculate cross sections values. The value of  $\varepsilon_{tagg}$  is diminished by Møller scattering in the radiator and any other radiationless electron background that increases the count rate in the scintillators of the tagger but does not contribute to the photon beam like for example radiation backscattered from the electron beam dump.

The number of photons  $N_\gamma$  can be measured using a lead glass detector with an efficiency of 100% for photon detection, unfortunately it is limited to a maximum photon flux of  $10^5$  per second, which is 2 orders of magnitude lower than the intensity required for the GDH sum rule experiment. To overcome this problem a pair detector is used. It can measure higher flux, but with less efficiency. Fig 3.3 shows the schematic view. It is composed of 3 plastic scintillators (P1, P2 and P3) and a 1 mm copper radiator where electron-positron pairs are created. A coincident signal between P2 and P3 in anti-coincidence with P1 is defined as a good event. The pair detector is calibrated regularly with the lead glass in specific runs with lower intensity, its efficiency is:

$$\varepsilon_{pair} = \frac{N_{pair}}{N_{lead}} = d_{eff} \sigma_{1cmCu}^{e^+e^-} \quad (3.4)$$

with  $N_{pair}$  the number of photons measured in the pair detector,  $N_{lead}$  photons in the lead glass detector,  $\sigma_{1cmCu}^{e^+e^-}$  the well known cross section of pair photoproduction in 1 cm of copper, and  $d_{eff}$  the effective thickness of the convertor.

Taking all this into account the photon flux is:

$$N_\gamma = \frac{N_{pair}}{d_{eff} \sigma_{1cmCu}^{e^+e^-}} \quad (3.5)$$

Because of polarization reasons that will become clear in the next section two different electron beam energies were used during the experiment  $E_0 = 525$  MeV and  $E_0 = 855$  MeV with tagging efficiencies of about  $\varepsilon_{tagg}^{525} \cong 0.075$  and  $\varepsilon_{tagg}^{855} \cong 0.15$  respectively.

### 3.2.4 Møller Polarimetry

The degree of polarization of the photon beam is another important ingredient for the analysis of the data in the GDH experiment. Since it is not 100%, not all detected events arise from polarized photons hence a precise knowledge of the real polarization degree is required.

During the bremsstrahlung process the longitudinal polarization of an electron is partly converted into circular polarization of the emitted photon. This transfer of polarization was calculated by Olsen and Maximon [Ols59] and reads:



$$\frac{P_\gamma}{P_e} = \frac{4E_\gamma E_0 - E_\gamma^2}{4E_0^2 - 4E_\gamma E_0 + 3E_\gamma^2} \quad (3.6)$$

where  $P_\gamma$  and  $P_e$  are the absolute photon and electron degree of polarization, while  $E_0$  and  $E_\gamma$  are the initial electron and photon energy respectively. At  $E_\gamma = E_0$ , when the entire energy of the electron is transferred to the photon, one has  $P_\gamma = P_e$ , which means that the electron degree of polarization is completely transferred to the photon. Fig. 3.4 illustrates the energy behavior of the polarization transfer. In order to obtain sufficient data with a relatively high degree of polarization in the delta region a primary electron beam of  $E_0 = 525$  MeV was chosen, additionally to the standard  $E_0 = 855$  MeV.

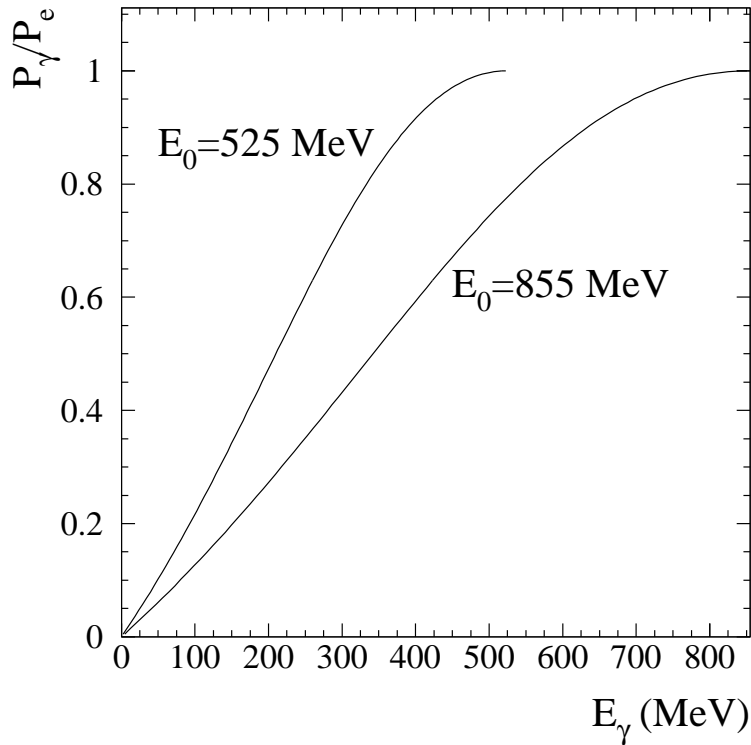


**Figure 3.4:** Degree of polarization transfer from the electron to the photon via the Bremsstrahlung process. The ratio  $P_\gamma/P_e$  between photon and electron polarizations as function of photon energy  $E_\gamma$  for two values of the primary electron energy  $E_0$ .

The electron degree of polarization  $P_e$  is measured by means of a Møller polarimeter. The cross section for Møller scattering of longitudinally polarized electrons off a magnetized ferromagnetic foil is polarization dependent. The polarized Møller scattering cross section can be factorized as follows:

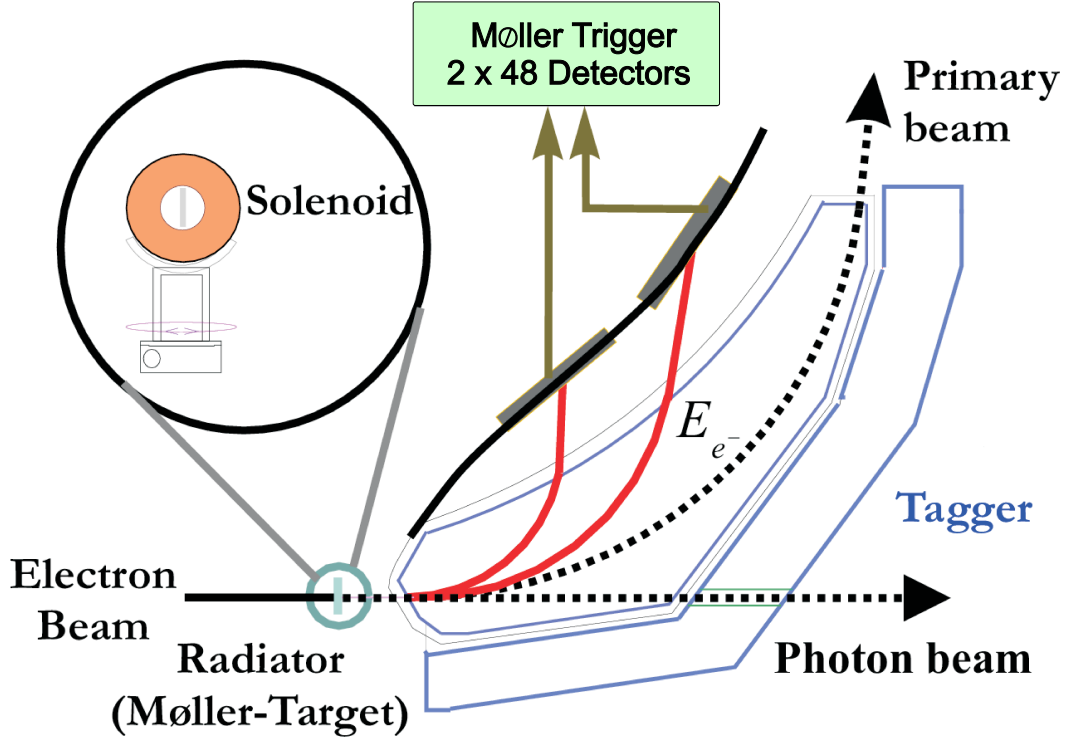


Figure 3.5: The Møller polarimeter.

$$\frac{d\sigma}{dE_e} = \left( \frac{d\sigma}{dE_e} \right)_{unpol} \left( 1 + \sum_{j,k} a_{jk} P_t^j P_e^k \right) \quad (3.7)$$

where  $\left( \frac{d\sigma}{dE_e} \right)_{unpol}$  is the unpolarized Møller cross section,  $P_t^j$  and  $P_e^k$  are the cartesian components of the target foil and electron beam polarization respectively, and  $a_{jk}$  the analyzing power. The elements of  $a_{jk}$  can be calculated from QCD [Ols59]. The non-diagonal tensor elements either vanish because of parity conservation or are negligible because of their weighting factor  $(E_0 + m_e)/2m_e$ . Hence, the asymmetry becomes:

$$A^{Møller} \approx a_{zz} P_t P_e \cos\alpha \quad (3.8)$$

with  $P_t$  and  $P_e$  the norm of the polarization of target and electron,  $\alpha$  the angle between the vectors, and  $a_{zz} = -7/9$ .

Thus, the Møller asymmetry can be measured experimentally by determining the number of events where beam and target have parallel  $N^{\uparrow\uparrow}$  or antiparallel  $N^{\uparrow\downarrow}$  orientation:

$$A^{M\ddot{o}ller} = \frac{N^{\uparrow\uparrow} - N^{\uparrow\downarrow}}{N^{\uparrow\uparrow} + N^{\uparrow\downarrow}} \quad (3.9)$$

Fig. 3.5 shows the experimental setup of the Møller polarimeter. The electron beam hits the polarized Vacoflux (49% Fe, 49% Co and 2% Va) foil, and 2 Møller electrons emerge. Two sets of tagger detectors were chosen to detect these electron pairs in coincidence. A good Møller event is a coincidence of two focal plane detectors with the sum of the corresponding electron energies equal to the primary beam energy  $E_0$ . The two main sources of background are secondary bremsstrahlung electrons and electrons from pair electroproduction. The former, which are not correlated in time, are suppressed by time correlation. The electrons from pair electroproduction are suppressed by demanding coincidences between single tagger channels. By coincidences in these sets of tagger channels the asymmetry  $A^{M\ddot{o}ller}$  can be measured. During the GDH sum rule experiment the degree of polarization of the target foil was  $P_t = (8.1 \pm 0.2)\%$  and the angle between the two vectors was chosen as  $\alpha = 25^\circ$ .

Taking into account 3.6 and 3.8 we can deduce that the photon beam polarization is given by:

$$P_\gamma = \frac{A^{M\ddot{o}ller}}{a_{zz}P_t \cos\alpha} \frac{4E_\gamma E_0 - E_\gamma^2}{4E_0^2 - 4E_\gamma E_0 + 3E_\gamma^2} \quad (3.10)$$

so, by measuring the asymmetry 3.9 with sufficient statistics the photon polarization can be determined with reasonable precision. In order to achieve a precision of 2% about 4 hours were sufficient. The average electron degree of polarization was  $P_e \approx 75\%$ .

### 3.3 Detector Setup

The aim of the experiment was to measure the total polarized photoabsorption cross sections of the nucleon from which the value of the GDH sum rule can be derived and the extraction of the helicity dependent cross section of the different partial reaction channels. The precise measurement of the total and partial photoabsorption cross sections of the nucleon imposes some important requirements for the detector system. A detector setup able to cover the whole angular distribution is required.

The detector setup, Fig. 3.6, used in Mainz satisfies the requirements for this kind of experiment. The main detector is DAPHNE (*DéTECTEUR à grande ACCEPTANCE pour la PHYSIQUE photoNUCLÉAIRE EXPERIMENTALE*) [Aud91]. It contains an internal vertex detector that enables to trace charged particles. In order to cover forward angles the MIDAS (*MIcrostrip DETECTOR ARRAY SYSTEM*) detector was inserted inside the DAPHNE frame [Alt00]. Electron background has a very important contribution, therefore a Čerenkov detector [Lan04] is used in anti-coincidence with the tagger to trigger only the hadronic

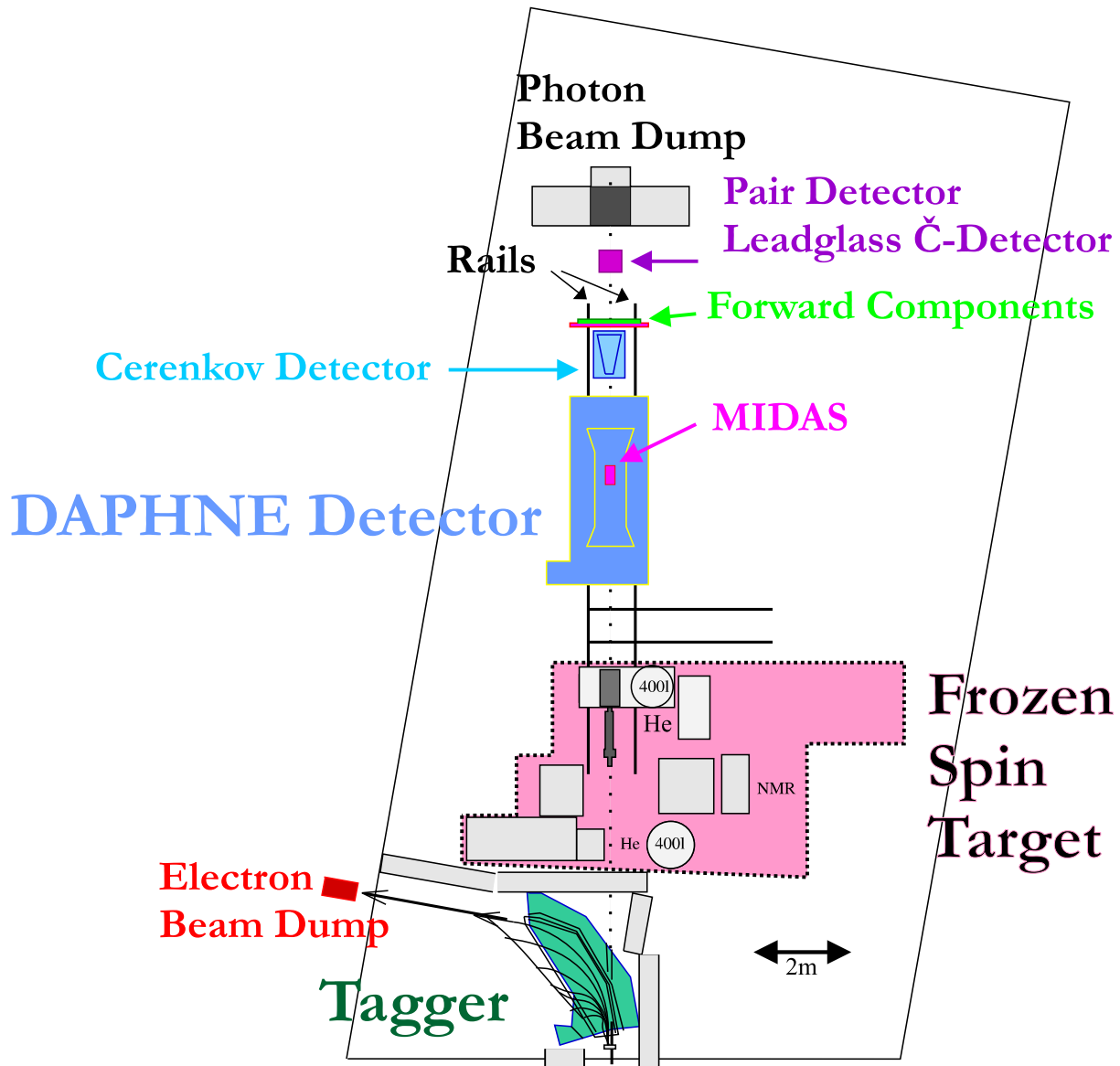


**Figure 3.6:** A2 experimental hall during the GDH experiment.

events. Two additional forward detectors STAR (*Scintillator from Tübingen for Angular Reconstruction*) and FFW (*Far Forward Wall*) [Sau96] were used. Fig. 3.6 shows the schematic of the detector setup in the A2 experimental hall. In the following sections each component of the detector array is discussed.

### 3.3.1 DAPHNE Detector

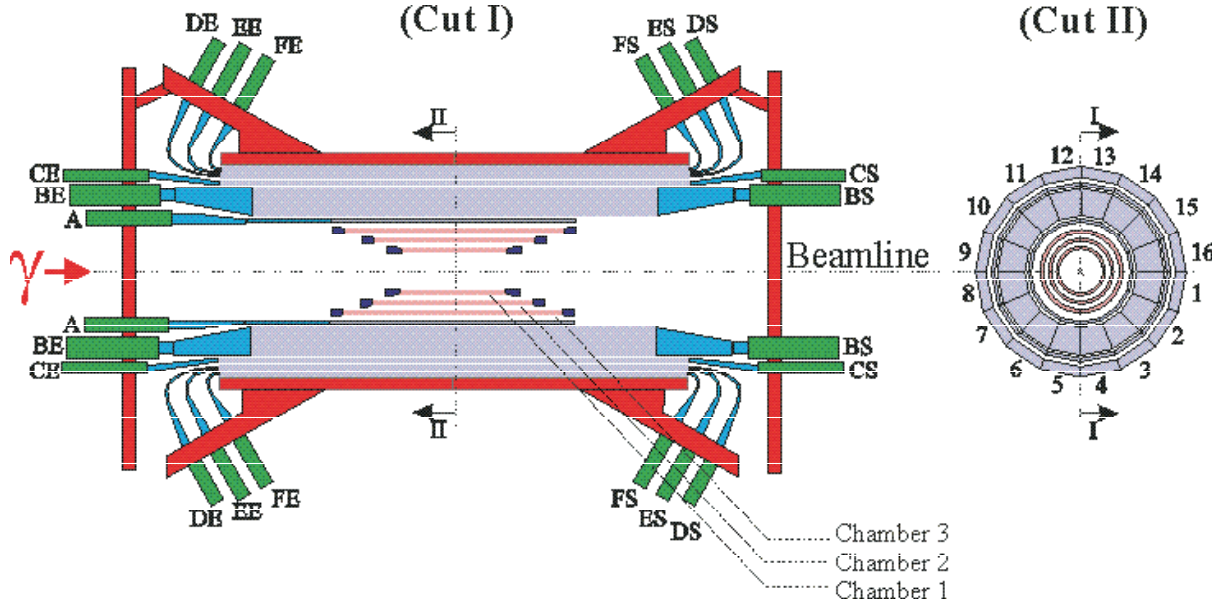


Figure 3.7: DAPHNE detector view.

The DAPHNE detector was built at the beginning of the 90's by the Saclay and Pavia groups. It was designed to measure total photoabsorption and single and double pion photoproduction cross sections of light nuclei in the intermediate energy range, especially at the energies available at MAMI:  $m_\pi < E_\gamma < 800\text{MeV}$ . Many results obtained with DAPHNE have been published over the past ten years.

The detector's main strong points are its wide angular acceptance (94% of  $4\pi$ ), its large acceptance in momentum and its capability to identify protons and charged pions with high efficiency. Neutrons and neutral pions are also identified with a moderate efficiency. In the case of protons and non-relativistic charged pions it provides also the kinetic energy which allows a reliable kinematical reconstruction of the reaction.

It is composed of 6 layers of plastic scintillators, each of them with 16 sections forming a 16-side regular polygon, Fig. 3.7. All scintillators, except for the first (A-layer), are read

by 2 photomultipliers. The three inner layers (A, B and C) are used to identify particles by the  $\Delta E/E$  method (see section 4.6). The first layer A acts as  $\Delta E$ -detector, while layer B provides the full energy information. The outer three layers (D, E and F) alternate with steel/lead and aluminum converters/absorbers forming a sandwich detector which adds detection efficiency for photons originating from the  $\pi^0$  decay. The inner vertex detector allows a precise vertex reconstruction.

### Vertex Detector

The inner part of DAPHNE is a vertex detector composed of 3 Multi Wire Proportional Chambers (MWPC) with cathode strip read out. Each of them has a layer of internal cathode strips, anode wires and external cathode strips. The walls are made of 1 mm thick Rohacell covered by 25  $\mu\text{m}$  kapton foil. The aluminum strips are helicoidally wound on the Rohacell cylinder with an angle of  $45^\circ$  with respect to the anode wires. The strips are 0.1  $\mu\text{m}$  thick by 4 mm wide aluminum layers with a 0.5 mm gap between adjacent strips. They overlap twice, so the wire signal is needed to identify the correct intersection point. The anode is composed of a 20  $\mu\text{m}$  diameter tungsten wires arranged parallel to the cylinder axis and separated by 2 mm. The anode-cathode distance is 4 mm. The MWPCs are filled with a gas mixture of 74.5% argon, 25% ethane and 0.5% freon. This mixture is a compromise between charge multiplication and localization requirements imposed by the ionizing track. The geometrical characteristics of each MWPC are given in table 3.2.

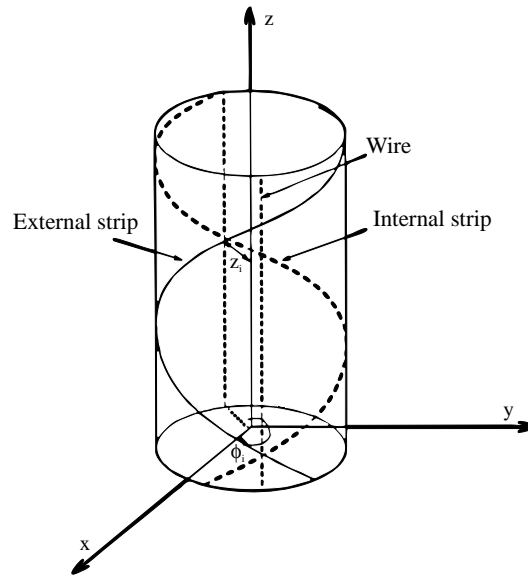


**Figure 3.8:** MWPC: Impact reconstruction of the trajectory of a charged particle.

MWPC	1	2	3
Length (mm)	360	560	760
Internal radius (mm)	60	92	124
External radius (mm)	68	100	132
Number of wires	192	288	384
Number of internal strips	60	92	124
Number of external strips	68	100	132

**Table 3.2:** Parameters of the MWPC's.

A charged particle traveling through the chambers ionizes the gas. The electrons move to the anode wire creating an avalanche of electron-ion pairs on their way by secondary ionization, while the positive ions are accelerated to the internal and external strips. From the center of gravity of the charge distribution on the strips of each chamber the azimuthal angle  $\phi$  and the longitudinal coordinate  $z$  of the impact point are evaluated. Fig. 3.8 illustrates how  $\phi$  and  $z$  are defined. Since the chambers are operating in proportional mode the charges created by secondary ionization are proportional to the charges created by the original traversing particle.

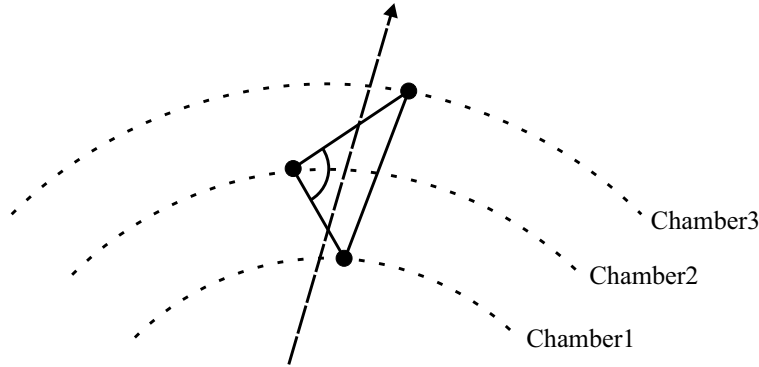


**Figure 3.9:** MWPC: Track reconstruction principle.

Once  $\phi$  and  $z$  are obtained for each chamber the trajectory can be obtained by fitting a straight line to these coordinates. In principle only 2 points are enough to reconstruct the trajectory, but due to some defect wire and strips 3 chambers are more reliable. Fig. 3.9 illustrates the track reconstruction. Since the three impact points will never be in a perfect straight line the condition that a vertical angle  $\beta > 172^\circ$  is required. This means that the middle point must not deviate more than 2.3 mm from the straight line defined by the first and third points. Up to five trajectories from one event can be simultaneously reconstructed.

The vertex reconstruction for two or more charged tracks is done by taking the intersection point of the trajectories. In the case of only one trajectory the vertex is defined as the closest point to the z-axis. In this case the error in z is about 1.5 cm. The precision of the MWPC is angle dependent and can be given as  $0.6^\circ < \Delta\vartheta < 1.1^\circ$  in polar angle,  $\Delta\varphi = 2^\circ$  in azimuthal angle and  $0.3 \text{ mm} < \Delta z < 1.5 \text{ mm}$  in longitudinal resolution.

In order to correct for the loss of particle tracks the global MWPCs track reconstructing efficiency should be determined. This efficiency depends not only on the number of tracks detected, but also on the target type and the identified particle. Table 3.3 shows the global MWPC detection and reconstruction efficiencies for different targets. There was a problem in the wire-electronic chain in one of the run periods (May 1998), therefore two different sets of values for the butanol target are needed. The problem was solved later.

Target	Hydrogen	Deuterium	Butanol(May)	Butanol	DButanol
Proton	100%	100%	100%	100%	100%
Single $\pi$	$97.98 \pm 0.02\%$	$97.87 \pm 0.01\%$	$94.0 \pm 0.05\%$	$96.2 \pm 0.06\%$	$96.2 \pm 0.06\%$
1 $\pi$ from $p\pi^+\pi^-$	$91.9 \pm 0.3\%$	$91.8 \pm 0.2\%$	$78.5 \pm 1.5\%$	$82.5 \pm 1.5\%$	$82.5 \pm 1.5\%$
2 $\pi$ from $p\pi^+\pi^-$	$91.6 \pm 0.3\%$	$91.1 \pm 0.2\%$	$76.0 \pm 2.0\%$	$80.0 \pm 1.5\%$	$80.0 \pm 1.5\%$

**Table 3.3:** Global MWPC detection and track reconstruction efficiencies.

### 3.3.2 MIDAS Detector

The *Microstrip Detector Array System* (MIDAS) was designed to enlarge the forward angles acceptance [Alt00]. Since DAPHNE's mechanical frame prevents particle transmission in the polar angular region  $5^\circ < \vartheta < 21^\circ$ , MIDAS has to be mounted as close to the target as possible. It is placed inside the DAPHNE frame very close to the target (see Fig. 3.10), it covers the region  $7.5^\circ < \vartheta < 16.5^\circ$ . It is not possible to go to lower angles due to the beam halo.

A schematic view of MIDAS is shown in Fig. 3.10. There are 2 parts: the vertex detector for trajectory reconstruction and the calorimeter. A central hole allows the primary photon beam to pass. The three main features of the MIDAS detector are the ability for detecting protons and charged pions with a small electromagnetic background contamination, track reconstruction for charged particles and particle identification for protons and pions.

The vertex detector consists of two annular doublesided semiconductor silicon detectors ( $V_1$  and  $V_2$ ). The n-sides are radially segmented in 16 sectors while the p-sides are divided into 48 concentric rings. The trajectory of a charged particle is reconstructed from the impact points in  $V_1$  and  $V_2$ , which are obtained from the intersection of the hit ring and sector. The polar and azimuthal resolution are  $1.4^\circ$  and  $12^\circ$  respectively.



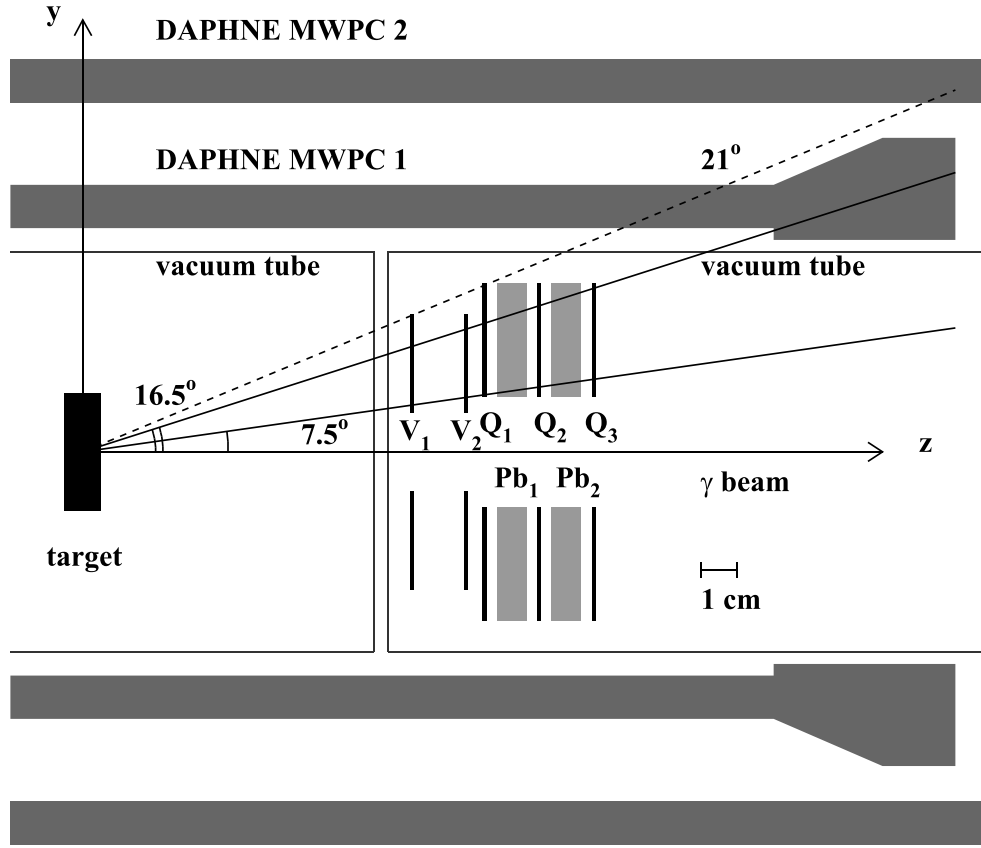


**Figure 3.10:** The MIDAS detector mounted inside the DAPHNE frame very close to the target cell.

The calorimeter contains an annular double silicon/lead sandwich ( $Q_1, Pb, Q_2, Pb, Q_3$ ) with single sided silicon detectors where only the p-side is segmented radially into 4 quadrants. This part is used for particle identification and energy measurements using the range-fit method (see section 4.6) adapted to the MIDAS geometry. The thickness of the lead sandwich corresponds to about 3 radiation lengths and it absorbs 99% of the electromagnetic background, mainly originating from the pair production.

Coincidences between  $Q_1$  and  $Q_2$  provide a good trigger for low energetic protons, whereas a  $Q_1 - Q_2 - Q_3$  coincidence serves as trigger for pions and high energy protons. The kinetic energy threshold is 60MeV for protons and 50MeV for pions. Protons are identified with a pion contamination less than 3%.

### 3.3.3 Čerenkov Detector

The pair production cross section is 3 orders of magnitude and Compton effect about one order of magnitude bigger than the total nuclear photoabsorption cross section. Because of this reason a threshold Čerenkov detector is needed to reduce this source of lepton background. It must have an efficiency very close to 100%. The Gent group built the detector used for the GDH sum rule experiment in Mainz and in Bonn. Fig 3.11 shows a schematic view of it. Two materials are used as radiator: 5 cm of Aerogel, and nitrogen gas. The Čerenkov light is reflected in a ellipsoidal shape mirror with one focus in the target and the other at the photomultiplier position. The active detection surface was enlarged using a nickel-plated straight cone as funnel. The efficiency reached in the detection of electrons is  $99,990 \pm 0.002$  %. It is used as veto in anticoincidence with the other detectors. In chapter 3 of [Lan04] a detailed explanation of the detector and the different tests done with it can be found.

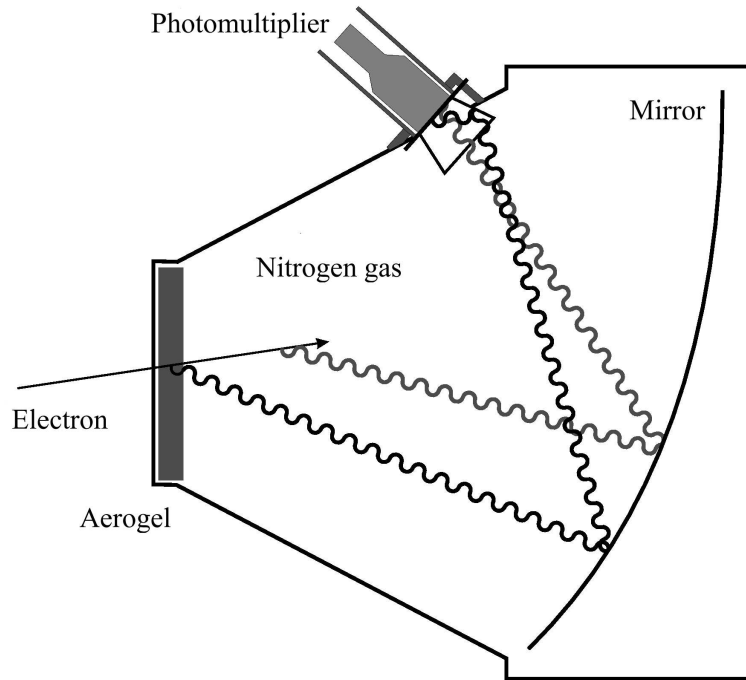


**Figure 3.11:** Side view of the Čerenkov detector.

### 3.3.4 Forward Components

The STAR (*Scintillator from Tuebingen for Angular Reconstruction*) [Fuc95] and the FFW (*Far Forward Wall*) [Emm95] detectors were built to cover polar angles between

2 and 7 degrees. The STAR detector consists of a large square scintillator sheet with a photomultiplier tube at each corner. It serves as trigger plate for charged particles. It is followed by an array of nine segmented concentric scintillator rings from which information on the polar angle of the charged particle can be obtained. A similar trigger plate as for the STAR is implemented in the FFW detector. It is followed by a scintillator-lead sandwich acting as a shower detector for photons originating from  $\pi^0$  decay.

The information given by these components is not included in the analysis procedure. Chapter 4 of [Lan04] contains a detailed discussion of the problems.

### 3.3.5 Data Acquisition

An important factor in the experiment is the speed and quality with which the data can be acquired and processed. The incoming data stream has to contain as many *good* events as possible. To this end the data acquisition programme ACQU [Ann96] was designed specifically for the GDH experiment. The raw signals from the detector electronics are acquired by a VME computer and transferred to a fast Linux PC where they can be monitored online. The data are finally saved on Exabyte data tape for later off-line analysis using the DAPHNE-programme.

With the present electronic setup and read out system a trigger rate of 350Hz with a live time of 85% was obtained during the data taking.

Each detector had its own set of condition on which it defined the occurrence of a good event. A general trigger was defined as:

- A valid signal from the tagging spectrometer.
- DAPHNE, MIDAS or STAR/FFW provide a detector trigger.
- No veto signal from any of the veto detectors.

In the case where the pair detector or the lead glass provide a signal, an independent trigger for these events was processed.

DAPHNE has two main types of triggers: one for neutral and another for charged particles. Any charged DAPHNE trigger requires a signal in the thin layer A. Additional threshold conditions on the sum of layer A and B signals, and on layer C signals are used to suppress a large part of the electron background. For a neutral trigger no signal at all in the wire chamber nor in the layer A should be registered.

As mentioned in section 3.3.2 a MIDAS trigger is either  $Q_1 - Q_2$  for low energetic protons, and  $Q_1 - Q_2 - Q_3$  for pions and high energy protons. The Čerenkov detector signal is placed in anti-coincidence with all detector triggers to suppress electromagnetic background in the forward direction. Each detector trigger is placed in coincidence with the tagger such that the corresponding photon energy is known for each detected event. For further information about the data acquisition system refer to [Lang04].

### 3.4 Unpolarized Target

A target system developed at the beginning of the nineties in Saclay, France, was used to liquify unpolarized deuterium ([Sac91] and [Mah99]). It was designed to fit in the geometry of the DAPHNE detector. It contains a two-stage Gifford-McMahon refrigerator that uses helium gas from a compressor to provide a temperature of 80K in the first stage and 17K in the second. Additionally, a Joule Thomson valve is coupled to the high pressure of the Gifford-McMahon refrigerator and temperatures of 3.2K can be reached by pumping the  $^4\text{He}$  bath after the valve.

The gas is liquified at a heat exchanger in the condenser pot, and flows to the target cell via a tube of about 10 mm in diameter. The liquid can easily be removed from the target cell and put back into the condenser pot, which allows fast empty-target measurements. Many heaters, temperature and pressure sensors allow for the control of the target during the experiment. This results in a target stability of 2 mbar in pressure and 0.1K in temperature, thus ensuring a target density stability of 0.5%. The cell was 15 cm long and had a radius of 2.15 cm, its walls had a thickness of 170  $\mu\text{m}$ .

This target was successfully used in the study of photoabsorption and photoproduction cross sections on hydrogen, deuterium,  $^3\text{He}$  and  $^4\text{He}$  [Cor96]. In 2003 it was employed for the GDH experiment in Mainz with a modified target cell of 10 cm length. Nowadays it is used in the Crystal Ball detector setup as hydrogen or deuterium target. Unfortunately the Joule Thomson valve does not work properly any more and helium can not be liquified.

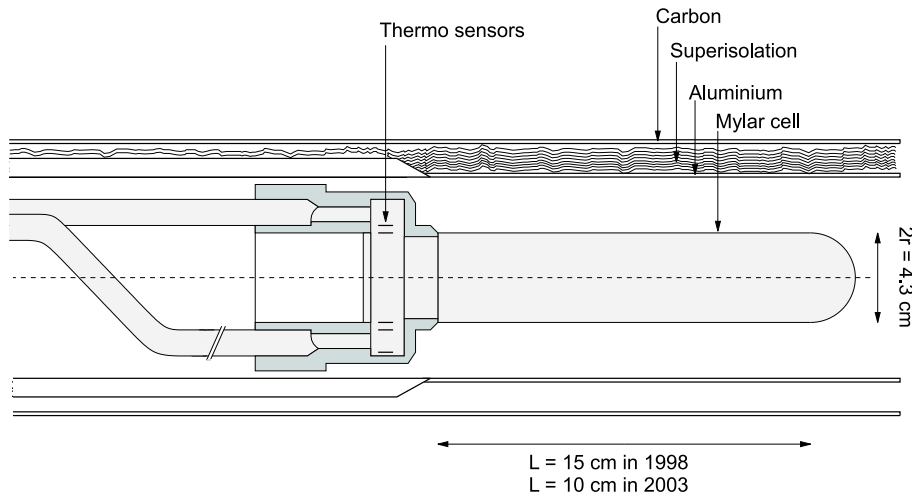


**Figure 3.12:** Unpolarized target cell.

## 3.5 Theoretical Principles of the Frozen Spin Target Technique

This section explains the theoretical principles of the polarized target. Particles with spin are polarized in the presence of an external magnetic field  $B$ . This field  $B$  splits the energy levels of the particles. The degree of polarization can be defined as the asymmetry between the populations of these levels. It is proportional to the magnetic field, and antiproportional to the temperature  $T$ .

High magnetic fields can be achieved with commercial superconducting magnets. The low temperatures are reached by means of a  $^3\text{He}-^4\text{He}$  dilution cryostat. The dynamical nuclear polarization (DNP) method increases the degree of polarization. In this method the degree of polarization is transferred from the electrons to the nucleons by microwave induced transitions. Its degree of polarization is measured by means of a nuclear magnetic resonance (NMR) system.

The frozen spin target can be divided into some subsystems: cryostat, magnet, microwaves, NMR, and control system. The next sections will go into details of all these parts for the 98 Bonn and the new Mainz targets. In the following subsections some theoretical issues about the polarization process, the dilution cryostat principle and the NMR technique are briefly discussed. The magnetic field is obtained with a superconducting coil, therefore a short discussion about superconductivity is given also. The microwave sources of the Bonn and Mainz target are quite different, hence they will be explained in detail in the respective sections.

### 3.5.1 Thermal Equilibrium Polarization

First the concept of degree of polarization in thermal equilibrium will be described in a simple way, later the DNP method will be explained in the framework of the solid effect model. It is not the intention of this work to present the theory in a rigorous way, but just to introduce the important concepts. For a more complete view see [Goe02] and the references therein.

Due to the Zeeman interaction between particles with spin  $S$  and an external magnetic field  $B$ , its energy levels split in  $2S+1$  sublevels. The degree of polarization is defined as the difference in population between the levels  $N_i$ . If the particles are in thermal equilibrium at temperature  $T$ , the population follows the Boltzmann statistics:

$$N_1 = N_0 \exp\left(\frac{\Delta E}{kT}\right) \quad (3.11)$$

where  $k$  is the Boltzmann constant, and the energy level splitting is given by the Zeeman interaction:

$$\Delta E = -g\mu SB \quad (3.12)$$

where  $g$  is the g-factor and  $\mu$  the magnetic dipole moment. In thermal equilibrium the general form of the degree of polarization is given by the Brillouin function [Kop86]:

$$P_S = \frac{2S+1}{2S} \coth \left( \frac{2S+1}{2S} \frac{g\mu SB}{kT} - \frac{1}{2S} \right) \coth \left( \frac{g\mu SB}{kT} \right) \quad (3.13)$$

For particles with spin 1/2 like electrons or protons the equation reduces to:

$$P_{\frac{1}{2}} = \frac{N_+ - N_-}{N_+ + N_-} = \tanh \left( \frac{g\mu B}{2kT} \right) \quad (3.14)$$

For spin 1 particles two parameters are needed to describe the system: *vector*  $P_1^d$  and *tensor polarization*  $P_2^d$  given by:

$$P_1^d = \frac{N_+ - N_-}{N_+ + N_0 + N_-} = \frac{4 \tanh \left( \frac{g\mu B}{2kT} \right)}{3 + \tanh^2 \left( \frac{g\mu B}{2kT} \right)} \quad (3.15)$$

If the small quadrupole interaction is neglected the tensor polarization is given by:

$$P_2^d = \frac{(N_+ - N_0) - (N_0 - N_-)}{N_+ + N_0 + N_-} = \frac{4 \tanh^2 \left( \frac{g\mu B}{2kT} \right)}{3 + \tanh^2 \left( \frac{g\mu B}{2kT} \right)} \quad (3.16)$$

Under thermal equilibrium  $P_1^d$  and  $P_2^d$  are related by:

$$P_2^d = 2 - \sqrt{4 - 3(P_1^d)^2} \quad (3.17)$$

In table 3.4 the values of  $g$  and  $\mu$  for electron, proton and deuteron are given:

Particle	g-factor	$\mu$ Magneton ( $10^{27} J/T$ )
Electron	$g_e = 2.0023193043737(82)$	$\mu_e = 9274.0154(31)$
Proton	$g_p = 5.585694675(57)$	$\mu_p = \mu_N = 5.0507866(17)$
Deuteron	$g_d = 0.8574382329(92)$	$\mu_d = \mu_N = 5.0507866(17)$

**Table 3.4:** Values of the g-factor and the magneton  $\mu$  of the electron, proton and deuteron.

The ratios  $\frac{g_e \mu_e}{g_p \mu_p} \cong 660$  and  $\frac{g_e \mu_e}{g_d \mu_d} \cong 4300$  show that electrons get easier polarized than protons or deuterons under the same conditions. In a magnetic field of 2.5 T at temperatures of 1 K the degree of polarization of electrons is more than 92%, whereas for protons it is only 0.25% and for the deuterium even less than 0.05%. A magnetic field

of approximately 10 T and temperatures of 20 mK are necessary to polarize protons up to a degree of 47%, the degree of polarization of the deuterium is then still only 10%. This way of polarizing protons or deuterons is called "brute force method". To obtain these conditions is very difficult and expensive, in addition detectors and outgoing particles are affected by the high magnetic field. Moreover, the build-up time for the final nuclear polarization in thermal equilibrium is some weeks because of the weak spin-lattice interaction. To overcome all these problems the nuclear polarization is enhanced by the principle of dynamical nuclear polarization.

### 3.5.2 Dynamical Nuclear Polarization

It was first suggested by A.W. Overhauser in 1953 [Ove53] and then experimentally shown by T.R. Carver and C.P. Slichter in the same year [Car53]. The coupled system electron-nucleon has to be considered. A double spin flip transition of electron and proton is produced by the application of an external microwave field with the proper frequency. The electron flips its orientation back in some milliseconds, while the nucleon keeps it for some hours. The electron couples again with another nucleon and the process continues. By this the degree of polarization of the target material increases.

The system electron-nucleon has 4 possible energy levels according to the spin orientation of both particles:

$$\begin{aligned} |a\rangle &= |e \downarrow n \uparrow\rangle \\ |b\rangle &= |e \downarrow n \downarrow\rangle \\ |c\rangle &= |e \uparrow n \uparrow\rangle \\ |d\rangle &= |e \uparrow n \downarrow\rangle \end{aligned}$$

Considering only Zeeman interaction, the selection rules of dipole radiation permits just transitions in which only one particle's spin flips at the same time. Double spin transitions are forbidden. The total Hamiltonian of the system can be written as the Zeeman interaction  $H_Z$ , plus other correction effects:

$$H = H_Z + H_{e-n} + H_{e-e} + H_{n-n} \quad (3.18)$$

where  $H_{n-n}$  is the coupling of two nucleons, which is negligible due to the smaller magnetic moment of proton and deuteron compared to the electron. The electron-electron interaction  $H_{e-e}$  is also neglected, since in the polarized target material the ratio between free electrons and nucleons is less than 1/1000. On the other hand the electron-nucleon coupling can be considered as a small perturbation since its ratio  $q \equiv \frac{H_{e-n}}{H_Z}$  is about 1%. Taking this perturbation into account double spin transitions have a nonzero probability

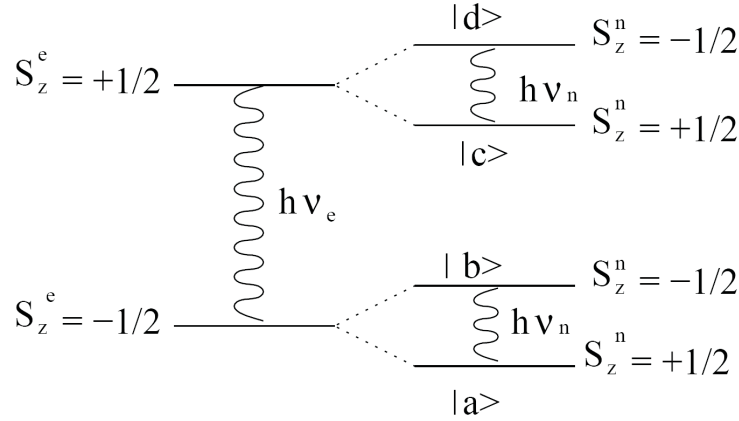


**Figure 3.13:** Energy levels of the coupled electron-nucleon system.

$W^+$  or  $W^-$ . Fig. 3.14 shows the possible transitions. The states can now be written as a linear combination of the states of the  $H_Z$  hamiltonian, defined as:

$$\begin{aligned}
 |a'\rangle &= |e \downarrow n \uparrow\rangle + q^* |e \downarrow n \downarrow\rangle \\
 |b'\rangle &= |e \downarrow n \downarrow\rangle + q |e \downarrow n \uparrow\rangle \\
 |c'\rangle &= |e \uparrow n \uparrow\rangle + q^* |e \uparrow n \downarrow\rangle \\
 |d'\rangle &= |e \uparrow n \downarrow\rangle + q |e \uparrow n \uparrow\rangle
 \end{aligned}$$

Microwave with the frequency  $\nu_+ = \nu_e + \nu_n$  (where  $\nu_e$  is the Larmor frequency of the electron, and  $\nu_n$  the one of the nucleon), are applied and a  $W^+$  transition from  $|a'\rangle$  to  $|d'\rangle$  is induced, see Fig. 3.14. The state  $|d'\rangle$  will decay via transition  $W^0$  rather than  $W^+$  to  $|b'\rangle$ . The electron will couple to another nucleon and the process starts again. By this the protons are pumped from  $|a'\rangle$  to  $|b'\rangle$  state which increments the number of particles in one level enhancing the degree of polarization. The same is valid for  $W^-$  transitions by applying microwaves of frequency  $\nu_- = \nu_e - \nu_n$ , and increasing the population of the  $|a'\rangle$  state. Fig. 3.15 shows the complete process.

In order to be an effective method two conditions have to be fulfilled. First, the total rate of spontaneous electron spin flips should considerably exceed the rate of spontaneous nuclear spin flips. And second, the induced transitions of the electron spins are taking place at a rate much faster than the nuclear relaxation rate. Since the relaxation time of the electron flip back is in the order of milliseconds, and the one of the nucleon is hours, the first conditions is easily fulfilled. For the second condition a microwave source with high intensity is required.



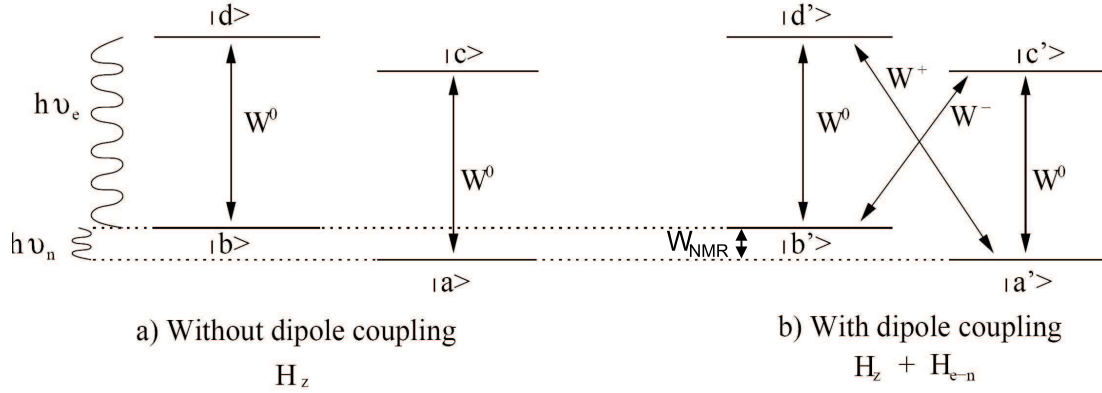


**Figure 3.14:** Possible transitions between different energy levels.  $W^0$ ,  $W^+$  and  $W^-$  represent the transition probability between the levels. Taking into account that  $W^0 \gg W^\pm$ .  $W_{NMR}$  is the transition measured with the NMR system in order to obtain the degree of the polarization.

Theoretically the maximum nuclear degree of polarization achievable is the electron degree of polarization:

$$P_N^{max} = P_e \quad (3.19)$$

However, there are some effects that make this impossible. Because of impurities or crystal imperfections other relaxation channels than those via the electron spins may exist. Only nucleons close to the electrons of the paramagnetic dopant are polarized. In order to understand the complete polarization process the dipole-dipole interaction between nucleons has to be taken into account. The nucleon polarized by the electron can transmit its degree of polarization to a neighbor nucleon. This is called spin diffusion process. Step 4 of Fig. 3.15 indicates it.

Fig. 3.15 shows a schematic view of the dynamical nuclear polarization process. Two different representations are shown. On one hand the energy levels picture, and on the other hand a semi-intuitive model where the spin orientation of electrons (green), close protons (red) and exterior protons (orange) are represented by arrows. 1) Consider the interaction of the electron of a doped radical with one of the close protons. There are also protons far away from the electron that will be polarized in a second process. 2) The microwave are applied which induces a simultaneous spin flip of the proton and electron. 3) The electron flips back (spin lattice relaxation), but the proton keeps its orientation due to the differences in relaxation times. The electron can couple with another proton and the process can start again. 4) The protons close to the electrons interact with the exterior protons and transfer their polarization via the spin diffusion process.

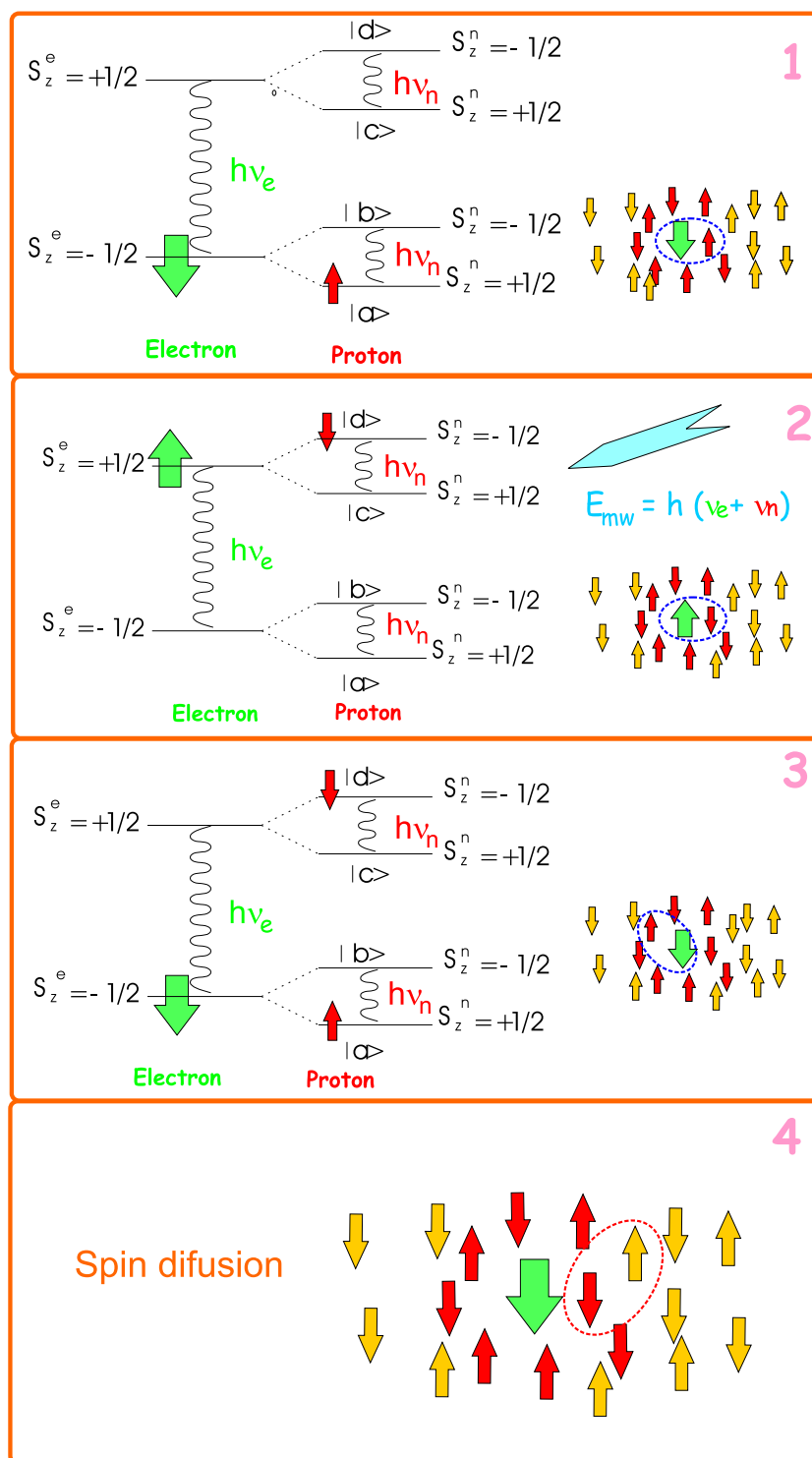


Figure 3.15: Dynamical nuclear polarization process.

This solid effect model is only valid if the electron paramagnetic resonance (EPR) line width is very narrow compared to the nuclear Larmor frequency. This can be true for crystals like LMN (Lanthanmagnesiumnitrat), the first successful target material [Sch65], but it is not valid for amorphous materials like butanol. In this case the electron spin coupling can no longer be ignored, which leads to an almost continuous energy band.

A more complete clarification is given by the spin temperature theory. The basic idea is to consider an isolated system of interacting spins defined by a temperature of equilibrium i.e. a Boltzman distribution of the population. The interaction between the spin systems and the lattice is interpretable in terms of heat contact between bodies of different heat capacities. The explanation of this effect exceeds the frame of this thesis, for more information refer to [Goe04a] and references therein.

### 3.5.3 Nuclear Magnetic Resonance Technique

The nuclear magnetic resonance technique can be used to measure the degree of polarization of a target material. The resonance frequency for the NMR circuit is adjusted to the Larmor frequency of the particle of interest. For protons, this is typically 106 MHz at 2.5T. The main idea is to measure the probability of the transition  $W_{NMR}$  (Figure 3.14) and thus the degree of polarization.

When the target material is placed in an external magnetic field  $B$ , and it is irradiated with radio frequency (rf) energy at the Larmor frequency  $w_L$  the spins can absorb or emit this energy. The response of a spin system to rf irradiation is described by its magnetic susceptibility:

$$\chi(w) = \chi'(w) - i\chi''(w) \quad (3.20)$$

where  $\chi'(w)$  and  $\chi''(w)$  are the absorbtion and the dispersion functions respectively. The spin polarization of the target material is given by the integral of the absorption function over the frequency  $w$  [Gol75]:

$$P = \left( \frac{2\hbar S}{g^2 \mu_N^2 \pi N} \right) \int_0^\infty \frac{w_L \chi''(w)}{w} dw \quad (3.21)$$

in this equation  $S$  is the spin,  $g$  is the g-factor,  $\mu_N$  is the nuclear magneton,  $N$  the number of spins and  $w_L$  the Larmor frequency.

The absorption function is measured by putting a coil of inductance  $L$  and resistance  $r_c$  around the target material. Through the inductive coupling between the spins and the coil, the impedance of the coil  $Z_c$  will become [Abr78]:

$$Z_c = r_c + iwL_c(1 + 4\pi\eta\chi(w)) \quad (3.22)$$

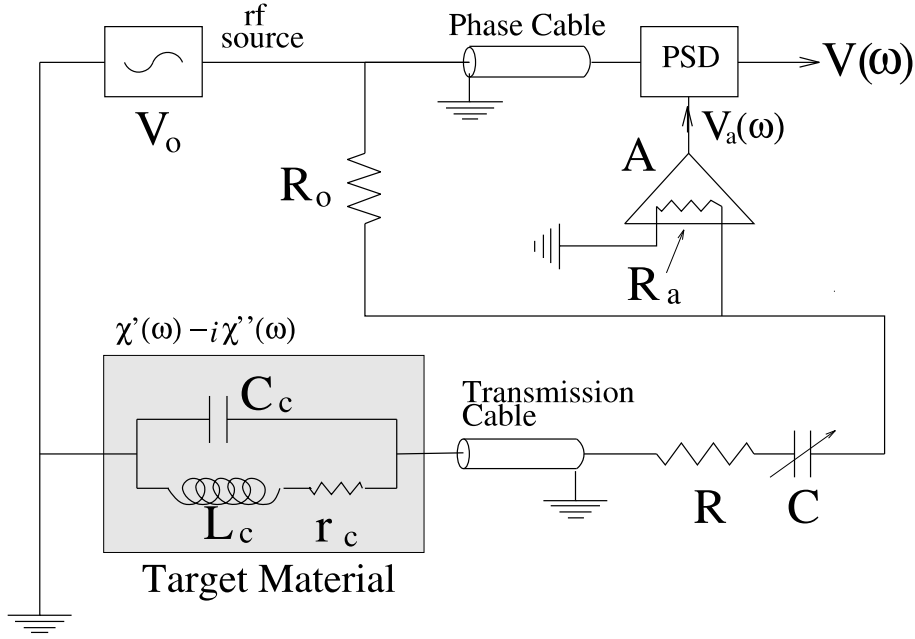


Figure 3.16: NMR circuit.

where  $\eta$  is the filling factor of the coil. The change of impedance is detected by a continuous wave, constant current Q-meter connected to a series LRC circuit as shown in Fig. 3.16. The LRC circuit consists of the NMR coil connected via a coaxial transmission line to the damping resistor,  $R$ , and the tuning capacitor,  $C$ . A frequency synthesizer connected to the Q-meter sweeps the rf frequency  $w$  over the values where  $\chi''(w)$  is non zero. A complex voltage  $V(w, \chi)$  which is a function of  $Z_c$  is generated if the current is constant. The voltage is a superposition of both the signal proportional to  $\chi$  and the so-called Q-curve, which is the response of the Q-meter to  $w$  in the absence of  $\chi$ . The last stage of the Q-meter selects the real part of the voltage by using the input rf signal as reference. The Q-curve is measured separately by changing the external magnetic field  $B$  such that  $w_L$  is well outside the range of the frequency scan of the Q-meter. In this case  $\chi''$  vanishes and  $\chi'$  is negligible. The two signals are subtracted and the result is the NMR signal:

$$S(w) = \text{Re}[V(w, \chi) - V(w, 0)] \propto \chi''(w) \propto P \quad (3.23)$$

The degree of polarization can be approximated by:

$$P = K \int \frac{w_L S(w)}{w} dw \quad (3.24)$$

where  $K$  is a constant that contains all the unknown frequency independent gains in

the Q-meter and it is determined by making a thermal equilibrium (TE) calibration at temperatures around 1 K. If the spin system is in thermal equilibrium with the lattice the degree of polarization is given by the Brillouin function (Eq. 3.13).

Once this constant  $K$  is obtained it can be used to measure the degree of polarization just by integrating the NMR signal  $S(w)$  over the frequency scan region.

### Thermal Equilibrium Measurement

The degree of polarization is measured in two steps. First, an NMR signal is taken at low temperatures with a magnetic field a bit different from that corresponding to resonance (typically 2.4 T). The polarization signal is the difference of the signal measured with a magnetic field corresponding to resonance (typically 2.5 T), and the signal measured in step one. If the NMR circuit provides a linear behavior of the amplification, then the difference signal depends only on the degree of polarization of the target material. The linearity is one of the most important features and a big challenge when building the NMR circuit. The quantity of interest is the area below the signal. Since this area is proportional to the degree of polarization (Eq. 3.24) the next relation is used:

$$\frac{Polarization_{Dynamical}}{Area\ Unit_{Dynamical}} = \frac{Polarization_{Thermal\ Equilibrium}}{Area\ Unit_{Thermal\ Equilibrium}} \quad (3.25)$$

The  $Area\ Unit_{Thermal\ Equilibrium}$  is measured in thermal equilibrium with the NMR signal at known magnetic field and temperature. Under these conditions the  $Polarization_{Thermal\ Equilibrium}$  is also known from Equation 3.14 and 3.15. Once these values are obtained the degree of polarization in the dynamical process  $Polarization_{Dynamical}$  is known by measuring the area under the NMR signal  $Area\ Unit_{Dynamical}$ .

### Shape of the Deuteron

In the case of the deuterated butanol another method can be used to measure the degree of polarization. From the shape of the NMR line the degree of polarization could be obtained. In [Dul96] the full explanation of this theoretical model as well as some results and comparisons with experimental data are given. Here only the main ideas of this model will be presented.

Due to the asymmetry in the spatial distribution of the deuterated butanol molecule ( $C_4D_9OD$ ) some local gradient fields are created by the C-D and O-D bonds. These electric gradient fields  $\nabla \vec{E}$  couple to the quadrupole tensor of the deuteron  $\vec{Q}$  causing an asymmetric splitting of the energy levels into two overlapping absorption lines. For a fixed value of the angle  $\theta$  between  $\vec{Q}$  and  $\nabla \vec{E}$  there are two resonant frequencies corresponding to the positive transition  $E_0 \leftrightarrow E_1$  with energy  $\Delta E_+ = E_0 - E_1$  and intensity  $I_+$ , and the

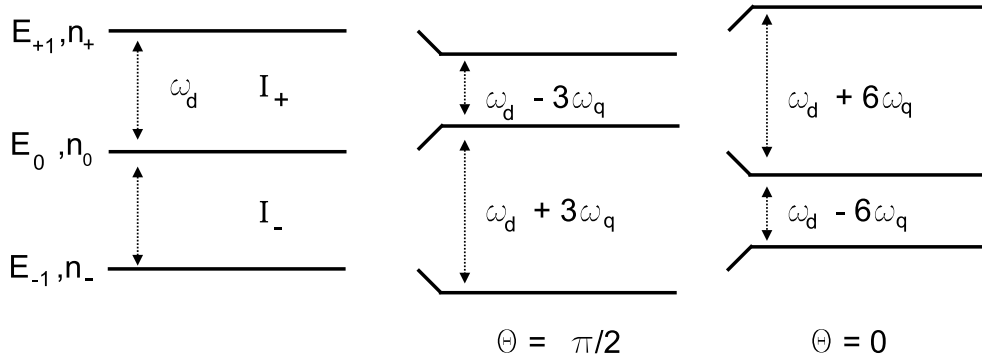


**Figure 3.17:** Energy level diagram of the deuteron spin system. The quadrupole interaction shifts the levels depending on the angle  $\theta$  between the quadrupole tensor  $\vec{Q}$ , and the electrical field gradient  $\nabla \vec{E}$ .

negative transition  $E_{-1} \leftrightarrow E_0$  with energy  $\Delta E_- = E_{-1} - E_0$  and intensity  $I_-$ . These two resonance frequencies are given by:

$$\Delta E \equiv \hbar w_{\pm} = \hbar w_d \mp 3\hbar w_q \{ [3 - \eta \cos(2\phi)] \cos^2(\theta) - [1 - \eta \cos(2\phi)] \} \quad (3.26)$$

which are no longer equal as in the case of pure Zeeman splitting (Fig. 3.17). In equation 3.26 the Larmor frequency of the deuterium is  $w_d$  and  $\hbar w_d$  represents the shift by the quadrupole interaction. The azimuthal angle  $\phi$  and the parameter  $\eta$  are necessary for describing bonds where the electric field gradient is not symmetric about the bond axis.

If we consider the level populations  $N_+$ ,  $N_-$  and  $N_0$  the vector polarization can be calculate as:

$$P_1^d = \frac{N_+ - N_-}{N_+ + N_- + N_0} = \frac{\frac{N_+}{N_-} - 1}{\frac{N_+}{N_-} + \frac{N_0}{N_-} + 1} \quad (3.27)$$

If the asymmetry parameter  $r$  is defined as  $r = e^{\frac{\hbar w_d}{kT}}$  then:

$$\frac{N_+}{N_-} = r^2 \quad \frac{N_0}{N_-} \approx r \left[ 1 + \frac{6}{5} \left( \frac{\hbar w_d}{kT} \right)^2 \right] \quad (3.28)$$

Hence the degree of polarization can be rewritten as:

$$P_{AS} = \frac{r^2 - 1}{r^2 + 1 + r} + \delta \left( \frac{\hbar w_d}{kT} \right)^2 \quad (3.29)$$

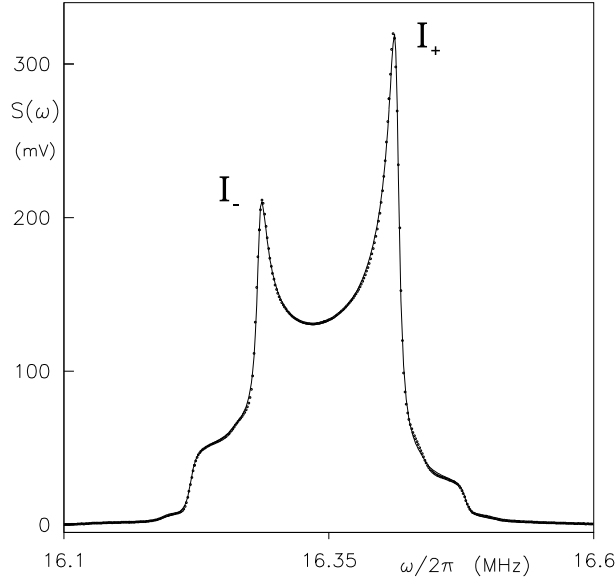


**Figure 3.18:** An enhanced signal of 44 % degree of polarization (circles) with the fitted curve superimposed (line). The two peaks correspond to  $\theta = \frac{\pi}{2}$ , the pedestals to  $\theta = 0$ . The right peak and the left pedestal corresponds to the  $E_0 \leftrightarrow E_1$  transition with intensity  $I_+$ , and the other peak and pedestal to the  $E_{-1} \leftrightarrow E_0$  transition with intensity  $I_-$ .

where  $\delta$  represents a function depending on the factor  $\left(\frac{\hbar w_d}{kT}\right)^2$ . The asymmetry  $r$  is proportional to the intensity factors  $I_{\pm}$ , that are connected to the height of the 2 peaks of the line shape, Fig. 3.18.

$$P_{AS} \propto r \propto I_{\pm} \quad (3.30)$$

This so-called simple r-Ratio method is valid to obtain an approximate measurement of the degree of polarization. A full theoretical expression of the NMR shape line is obtained from a fit of 13 parameters to determine  $S(w)$ . The absorption function  $\chi''(w)$  requires 8 parameters: the gain factor of the Q-meter  $\Theta$ , the asymmetry  $r$ , the Larmor frequency of the deuteron  $w_d$ , the dipolar broadening parameter  $\sigma$ , the quadrupol coupling of carbon  $w_q^C$  and oxygen  $w_q^O$ , and two parameters  $\eta$  and  $\kappa$  to describe the O-D and C-D bonds. In addition, the instrumentation requires 5 fitting parameters: the false asymmetry  $\xi$  and 4 parameters for third order polynomial of the residual background.

All these parameters are obtained from the fit of many NMR signals and the comparison with the TE degree of polarization measurement. Some parameter values can be cross checked with other methods of measurement and they are in good agreement. This technique has been used for more than ten years in different NMR measurements.

### 3.5.4 Frozen Spin Target Principle

As it was previously shown, to polarize a material high magnetic fields and low temperatures are needed. A commercial superconducting magnet can provide the required magnetic field intensity and homogeneity. The low temperatures are attained with a dilution refrigerator that must fit in the geometry of the detector. The next section will explain the physical principles of the dilution cryostat, and in section 3.5.6 some basic ideas of superconductivity will be presented.

An important constraint in the design of a scattering experiment is that the target should allow produced particles to leave with small energy losses, and within as large as possible solid angle.

To overcome this problems the frozen spin method was developed [Nii76]. In 1967, Schmugge and Jeffries [Sch65] already discussed the possibility of maintaining the target polarization without microwaves (and thus in a less homogeneous and, perhaps, less strong field), based on their observation that the nuclear spin-lattice relaxation time in LMN extrapolates to very low values at temperatures below 1 K. This would free the experiment from the constraint of having the target inside a big magnet, allowing large solid angle for observing scattered particles.

The principle of the frozen spin target is as follows. The target material is located inside the refrigerator. The cryostat is inserted into a polarizing magnet able to produce large magnetic fields with high homogeneity. The microwaves are fed into the target material in order to increase the degree of polarization via the DNP process. This is the so called *Polarization Mode*, where the refrigerator is driven at around 300 mK. Once the maximum degree of polarization is achieved the microwaves are turned off. At this moment the temperature is driven down to about 50 mK, where the spins get "frozen" and the relaxation time increases, this is the so-called *Frozen Spin Mode*. Then the field of the polarizing magnet is reduced and a smaller holding magnet keeps the magnetic field at lower values. Then the polarizing magnet is removed and the detector is installed around the target.

Nowadays, thanks to superconducting wires, polarizing magnets with magnetic fields of more than 2.5 Tesla and with homogeneity  $\Delta B/B < 10^{-4}$  are available. In 1995, the introduction of internal superconduction holding coils able to produce about 0.4 Tesla with a small amount of material opened the possibility to operate in combination with  $4\pi$  detectors, where detector components are placed closely around the target refrigerator [Dut95]. These wires have a maximum current limit that gives the maximum magnetic field.



### 3.5.5 Cryostat

In order to fulfill the requirements of low temperature and high cooling power in continuous operation a horizontal dilution cryostat is needed. During the GDH experiment in 1998 the Bonn frozen spin target was used [Bra99]. It contains a dilution cryostat that will be illustrated in section 3.6. The central component of the new Mainz frozen spin target is a horizontal dilution refrigerator developed in a collaboration between the JINR in Dubna and the KPH in Mainz. Section 3.7 is devoted to this new target. In the next lines the physical principles of the dilution cryostat are expounded.

#### Liquid Helium Pre-cooling System

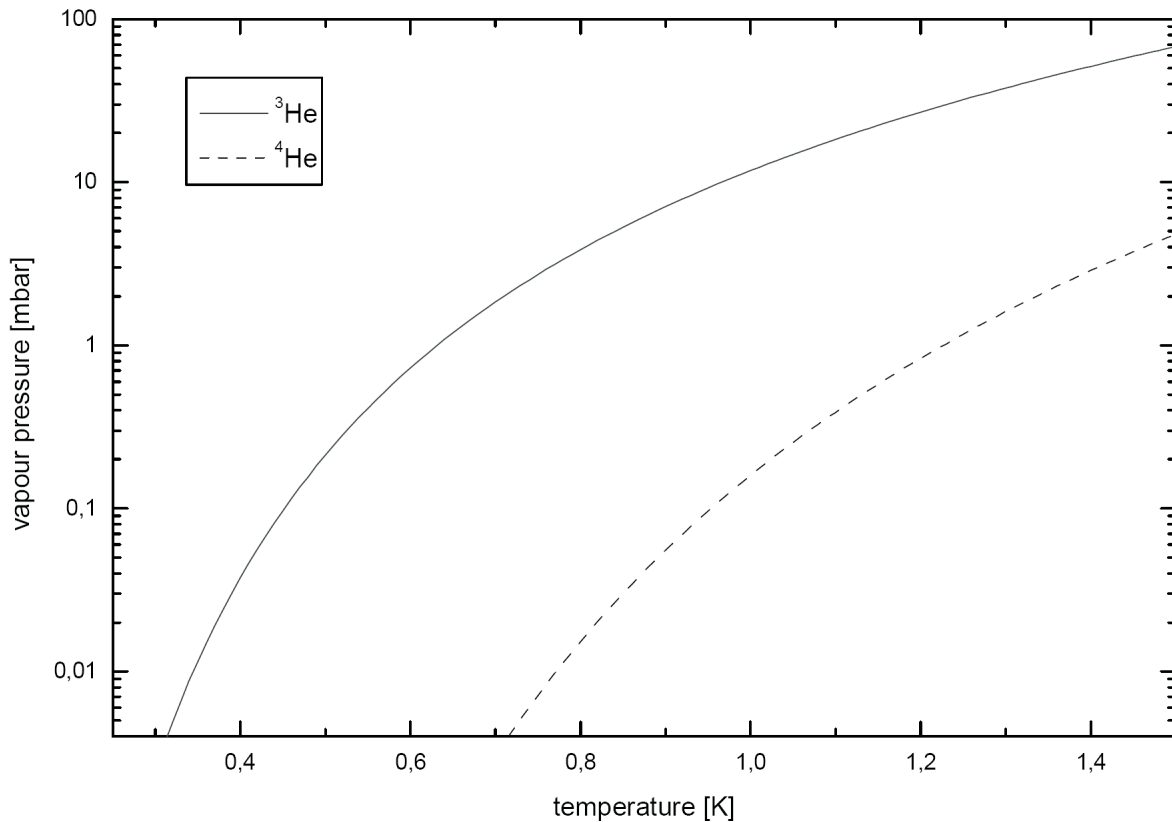


**Figure 3.19:** Vapor pressure of liquid  $^3\text{He}$  and  $^4\text{He}$ .

Normally a dilution cryostat has an evaporation refrigerator as pre-cooling system. Typically liquid  $^4\text{He}$  is used to cool down. Fig. 3.19 displays the vapor pressure curve of

$^4\text{He}$  and  $^3\text{He}$ . By pumping out gas from a bath of  $^4\text{He}$  the gas pressure is reduced and temperatures around 0.8 K are easily reached with commercial pumps. The helium's heat of evaporation is  $L_{He} \approx 2.6$  kJ/l and its enthalpy  $H$  between 4.2 K and 300 K is about 200 kJ/l, hence it is important to use the outgoing gas to cool the outer parts of the cryostat and thermally isolate the coldest inner part, where the dilution refrigerator is placed.

The cooling power in the liquid chamber of an evaporation cryostat is given by:

$$\dot{Q} = \dot{n}[H_{liq} - H_{vap}] = \dot{n}L \quad (3.31)$$

where  $H_{liq}$  and  $H_{vap}$  are the enthalpy of the liquid and the vapor phases respectively, and  $L$  is the latent heat of evaporation. Normally a pump with constant-volume pumping speed  $\dot{V}$  is used and therefore the mass flow  $\dot{n}$  across the liquid-vapor boundary is proportional to the vapor pressure.

$$\dot{n} \propto P_{vap}(T) \quad (3.32)$$

The vapor pressure  $P_{vap}(T)$  can be estimated from the Clausius-Clapeyron equation, which in a rough approximation can be written as:

$$\left(\frac{dP}{dT}\right)_{vap} = \frac{S_{gas} - S_{liq}}{V_{m,gas} - V_{m,liq}} \cong \frac{LP}{RT^2} \quad (3.33)$$

where  $S$  is the entropy and  $V_m$  the molar volume. The vapor pressure is then proportional to:

$$P_{vap} \propto e^{-L/RT} \quad (3.34)$$

When we approximate  $L \cong \text{constant}$ , then the dependence of the cooling power with the temperature is:

$$\dot{Q} = \dot{n}L \propto P_{vap} \propto e^{-1/T} \quad (3.35)$$

The cooling power of an evaporator refrigerator decreases rapidly with decreasing temperature. The practical low temperature limits are typically about 0.8 K for  $^4\text{He}$  and 0.3 K for  $^3\text{He}$  (Fig. 3.19). In order to reach lower temperatures with high cooling power dilution cryostats are used.

### Dilution Cryostat

A dilution cryostat employs the enthalpy of a mixture of liquid  $^3\text{He}$ - $^4\text{He}$  to cool down. In 1951 H. London proposed this idea [Lon51]. In 1965 the first dilution refrigerator, produced by Das, De Bruyn Oubother and Tachonis in Leiden University, could reach 0.22

K [Das65]. One year later the Dubna group started producing more efficient refrigerators [Neg66], and in 1968 Neganov obtained 5.5 mK [Neg68]. Nowadays commercial cryostats able to reach 4 mK are available.

The pre-cooling evaporation refrigerator uses the phase transition from liquid to vapor to cool. The dilution cryostat also exploits a transition, but from a concentrated to a diluted phase of  $^3\text{He}$  mixed in liquid  $^4\text{He}$ . To transfer  $^3\text{He}$  from concentrated to diluted phase requires energy that is taken from the surrounding, which leads to a reduction of the temperature.

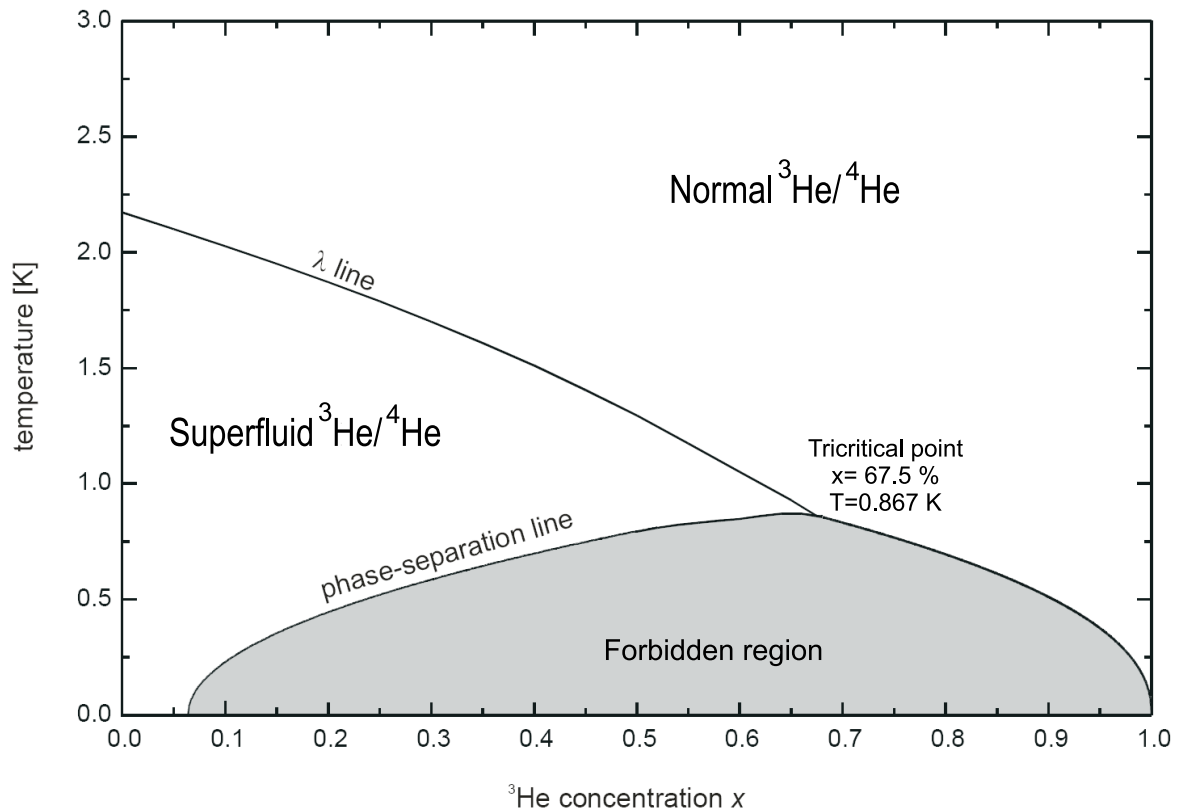


**Figure 3.20:** Phase diagram of liquid  $^3\text{He}$ - $^4\text{He}$  mixtures at saturated vapor pressure. The diagram shows the lambda line for the superfluid transition of  $^4\text{He}$ , the phase separation line of the mixtures below which they separate into a *concentrated*  $^3\text{He}$ -rich and a *diluted*  $^3\text{He}$ -poor phase.

### Liquid Mixtures of $^3\text{He}$ and $^4\text{He}$

In Fig. 3.20 one can see the concentration-temperature phase diagram of liquid  $^3\text{He}$  mixed with  $^4\text{He}$ . The concentration  $x$  of  $^3\text{He}$  influences the properties of the mixture. It is defined as:

$$x = \frac{n_3}{n_3 + n_4} \quad (3.36)$$

with  $n_3$  and  $n_4$  the number of  $^3\text{He}$  and  $^4\text{He}$  atoms, respectively.

At atmospheric pressure pure  $^4\text{He}$  becomes superfluid at 2.177 K, but if some  $^3\text{He}$  is mixed the phase transition temperature changes following the lambda line. Above the tricritical point ( $T = 0.87$  K,  $x = 67.5\%$ ), the liquid can be superfluid or normal fluid depending on the concentration  $x$ . Below this point the mixture separates into 2 different phases, one with high concentration of  $^3\text{He}$  (*concentrated phase*), and the other with low content of  $^3\text{He}$  (*diluted phase*). This second order transition of phase is employed to refrigerate the dilution cryostat.  $^3\text{He}$  is evaporated from the diluted phase forcing atoms from the concentrated phase to move into the other phase. Due to the difference in enthalpy the process can be used to cool down. The heat of mixing is:

$$\dot{Q} = \dot{n}_3 [H_{3,d}(T_{mc}) - H_{3,c}(T_{ex})] \quad (3.37)$$

where  $\dot{n}_3$  is the number of  $^3\text{He}$  atoms per unit of time,  $H_{3,d}$  is the enthalpy of diluted  $^3\text{He}$  inside the mixing chamber, which has a temperature  $T_{mc}$ , and  $H_{3,c}$  is the enthalpy of the concentrated phase in the last heat exchanger before entering the mixing chamber with temperature  $T_{ex}$ . If  $H_{3,d}(T_{mc}) > H_{3,c}(T_{ex})$  then  $^3\text{He}$  diffusing across the phase boundary from the concentrated to the diluted phase absorbs heat analogous to the evaporation of a liquid into a gas.

Taking some experimental data available for the specific heat, and doing some reasonable simplifications the dependence of the cooling power  $\dot{Q}$  of a dilution cryostat with the temperature  $T$  can be expressed as [Pob96]:

$$\dot{Q} \cong \dot{n}_3 (95T_{mc}^2 - 11T_{ex}^2) \quad (3.38)$$

This relation tells us that the decreasing of cooling power is proportional to  $T^2$ , and not to  $e^{-T}$  as in the evaporation cryostat (Eq. 3.35). This is because the concentration of  $^3\text{He}$  in the diluted phase is almost constant below 0.1 K, while the vapor density decreases exponentially. Even at absolute zero temperature the concentration of  $^3\text{He}$  in the diluted phase is nonzero. This becomes clearer when the quantum properties of the liquids are taken into account, see next section.

The lowest temperature attainable in continuous mode in the mixing chamber depends mainly on the temperature of the incoming  $^3\text{He}$ . The maximum temperature allowed for

the liquid leaving the last heat exchanger before entering the mixing chamber is:

$$T_{ex} \leq 3T_{mc} \quad (3.39)$$

Because of this reason the design of the last heat exchangers is of major importance. They have to be very efficient in transferring the heat from the incoming to the outgoing helium. The important parameters for a heat exchanger are three. They should have small volume to reach the equilibrium temperature very fast. A small impedance is needed to obtain very few losses due to viscosity. Small thermal resistance between the streams is also required in order to get good temperature equilibrium between them. The heat flow  $\dot{Q}$  in a material can be written as:

$$\dot{Q} = \kappa A \Delta T \quad (3.40)$$

where  $\kappa$  is the thermal conductivity,  $A$  the cross section area and  $\Delta T$  the gradient of temperature. The thermal conductivity coefficient  $\kappa(T)$  depends on the material, and the heat transport mechanism. It can be understood as a diffusion process of the phonons and electrons through the lattice. Imperfections and impurities can influence the transport of heat. Therefore special care should be taken in choosing the materials and their purity. The best way to improve the heat flow is to increase the cross section area  $A$  as much as possible. On the other hand the thermal boundary resistance between helium and the heat exchanger material at temperatures below 1 K has to be taken into account. It is called the Kapitza resistance and can be defined as:

$$R_k = \frac{\chi}{AT^3} \quad (3.41)$$

where  $\chi$  is an experimental parameter that depends on the body in contact with helium, and  $A$  is the cross section area. The transfer of heat between liquid helium and solids occurs only via phonon transmission. The velocity of the phonons in helium is about  $v_h \approx 200$  m/s, while in metals it is  $v_h \approx 5000$  m/s. This produces acoustic impedance mismatches between the solid material and the liquid helium, which means that the heat flow between them is very small, and in addition it becomes smaller with decreasing temperatures.

There exist different kinds of heat exchangers, in section 3.7.1 the ones employed in the new Mainz frozen spin target are explained in some detail.

### Quantum $^3\text{He}$ - $^4\text{He}$ Mixture

In order to understand the phase diagram of Fig. 3.20 one has to think about the helium isotopes as quantum liquids.  $^4\text{He}$  has spin 0, hence it is a boson. On the other hand  $^3\text{He}$  is composed of 2 protons and 1 neutron, the total spin is 1/2 therefore it is a fermion.

Both isotopes follow different statistics.  $^4\text{He}$  can go into the Bose condensate state, with all particles in the lowest energy level. In the case of the  $^3\text{He}$  only one particle for each energy level is allowed due to the Pauli exclusion principle.

Below 0.5 K almost all  $^4\text{He}$  atoms are in a Bose condensate state, there are no excitations, no phonons or rotons. It acts as an inert superfluid background.  $^3\text{He}$  inside the  $^4\text{He}$  bath can be seen as a Fermi-like gas, but taking into account the interaction with the  $^4\text{He}$  in the effective mass. For concentrations of  $x= 6.6\%$  the effective mass is about 2.45 times bigger than the normal mass.

$^3\text{He}$  has the same Van der Waals force as  $^4\text{He}$  since both have the same electron charge distribution.  $^3\text{He}$  has just less mass, and therefore less density. This fact tells that the concentrated phase will stay over the diluted phase.

Due to its smaller mass the  $^3\text{He}$  atom has larger zero-point motion than the  $^4\text{He}$  atom. Therefore, in the liquid phase  $^4\text{He}$  atoms occupy a smaller volume than the  $^3\text{He}$  ones. The  $^3\text{He}$  atom will be closer to the  $^4\text{He}$  than it would be to the  $^3\text{He}$ . Hence its binding is stronger, and it would prefer to stay in liquid  $^4\text{He}$ .

Because of the large zero-motion the liquid around a  $^3\text{He}$  atom is more diluted than near a  $^4\text{He}$  atom. If more  $^3\text{He}$  atoms move into the mixture they will be attracted to this region of less density. Due to this attractive interaction between  $^3\text{He}$  atoms the binding energy of a  $^3\text{He}$  atom in  $^4\text{He}$  should increase with increasing  $^3\text{He}$  concentration  $x$ . But, since  $^3\text{He}$  are fermions, only one particle per energy level is allowed. The number of  $^3\text{He}$  atoms in the  $^4\text{He}$  bath is limited by the Fermi statistics. At absolute zero the concentration of  $^3\text{He}$  is about 6.6%. If more  $^3\text{He}$  is admixed it goes to the concentrated phase.

### Osmotic Pressure

The  $^3\text{He}$ - $^4\text{He}$  mixture separation occurs in the so called *mixing chamber*. The evaporation of  $^3\text{He}$  from the diluted phase is not done here but in another vessel called *still*. The  $^3\text{He}$  will flow from the mixing chamber to the still by osmotic pressure:

$$\Pi = \frac{1}{V_4} \int_{x_i}^{x_f} \frac{x}{1-x} \left( \frac{\delta\mu_3}{\delta x} \right)_{PT} dx \quad (3.42)$$

where  $V_4$  is the molar volume of  $^4\text{He}$  and  $\mu_3$  the chemical potential of  $^3\text{He}$ .

Making some simplifications, supposing ideal gas, for low  $x$  concentrations and at temperatures  $T > 0.15\text{K}$  the osmotic pressure can be enunciated as:

$$\Pi = \frac{1}{V_4} RTx \quad (3.43)$$

with  $R = 8,31451 \text{ J/Kmol}$  the universal gas constant and  $T$  the temperature.

Consider the osmotic pressure between the mixing chamber and the still:

$$\Delta\Pi = \frac{R}{V_4} [x_{mc}T_{mc} - x_{st}T_{st}] \quad (3.44)$$

Typical values are a concentration of  $x_{mc} = 6.6\%$  and temperatures of  $T_{mc} = 10$  mK in the mixing chamber, and in the still  $T_{st} = 0.7$  K with a concentration of  $x_{st} = 0.1\%$ . By pumping the  ${}^3\text{He}$  from the still this concentration is reduced and some gradient of pressure is created. The maximum theoretical pressure will be reached when  $x_{st} = 0\%$ , in this case the pressure is comparable to the hydrostatic pressure of about 1 meter of helium. In this simple calculus it was not considered that at this temperatures the  ${}^3\text{He}$  in both phases is in a degenerate state. The fountain pressure effect resulting from the superfluidity of  ${}^4\text{He}$  was neglected because it is smaller compared with the osmotic pressure.

### Working Principle of a Dilution Cryostat

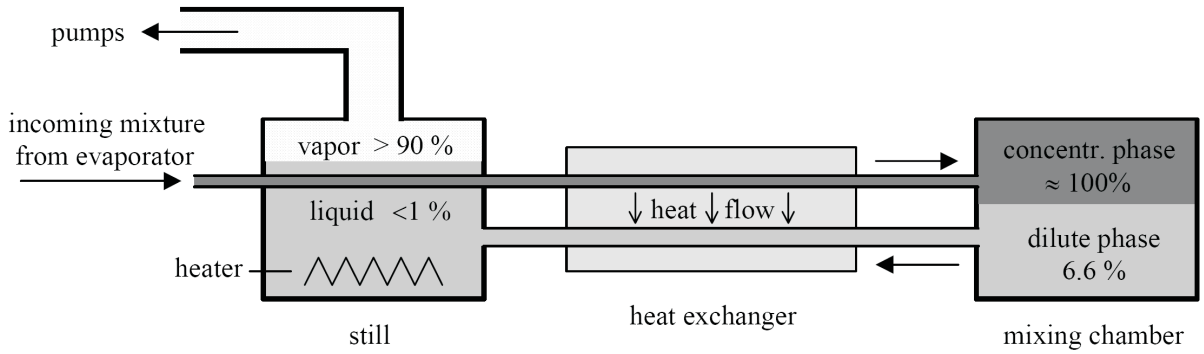


**Figure 3.21:** Flow diagram of a dilution cryostat unit.

The injected  ${}^3\text{He}$ – ${}^4\text{He}$  gas mixture is pre-cooled and liquified at about 2.5 K using a  ${}^4\text{He}$  evaporator cryostat. The liquid is further cooled down by thermal contact with the *still*, which is at about 0.7 K. Before entering the *mixing chamber* the liquid passes through some counter-flow heat exchangers in order to reduce the temperature as much as possible. Outgoing cold liquid from the mixing chamber is employed to pre-cool the incoming helium.

The mixing chamber is the coldest point. There the liquid separates in the upper concentrated phase and the lower diluted phase. A capillary connects the lower part with the still. Because of the osmotic pressure the  ${}^3\text{He}$  will flow from the diluted phase to the still. Here a heater is installed and the helium is evaporated and pumped out.

At temperatures below 1 K the vapor pressure of  $^3\text{He}$  is about 2 orders of magnitude bigger than the  $^4\text{He}$  vapor pressure (Fig. 3.19), which means that the most of the gas evaporated is  $^3\text{He}$ . A pumping system evacuates the gas. This gas is re-injected at room temperature into the cryostat, cooled down, liquified and the process starts again.

### 3.5.6 Superconductivity

In order to polarize the target material a superconducting magnet able to produce about 2.5 Tesla with a homogeneity of  $\Delta B/B \leq 10^{-4}$  is needed. In addition, the internal holding coil is also superconducting. This section will deal with some basic ideas of superconductor materials. This very open field of physics has been changing and improving a lot in the last years.

Superconductivity is a macroscopic quantum effect discovered in 1911 by Heike Kamerlingh Onnes, while he was studying the resistivity of mercury at low temperatures using liquid  $^4\text{He}$ , that he had liquified for the first time just 3 years before. No satisfactory theory could explain this effect until the 50's with the phenomenological Ginzburg-Landau theory [Gin50] and the microscopic BCS theory [Bar57].

The BCS theory is based on the idea that pairs of electrons couple together forming Cooper pairs. An electron moving through a conductor will attract nearby positive charges in the lattice. This deformation of the lattice causes another electron, with opposite "spin", to move into the region of higher positive charge density. The two electrons are then held together with a certain binding energy. When this binding energy is higher than the energy provided by kicks from oscillating atoms in the conductor (which is true at low temperatures), then the electron pair will stick together and resist all kicks, thus not experiencing resistance. These two combined electrons now form a state with spin 1, hence they are bosons and can undergo Bose-Einstein condensation.

The important parameters for a superconducting wire are the critical current  $I_c$  which it can carry before becoming a normal conductor, and the critical external magnetic field  $H_c$ . There are two types of superconductors. The type I repels the external magnetic field until it arrives to a critical value  $H_c$ , and then it becomes a normal conductor. The type II superconductors have two critical magnetic fields. For magnetic fields bigger than some value the field can penetrate the superconductor, but it still conducts electricity without resistance. If the field is even increased the wire becomes a normal conductor. In type I the transition to superconduction is very abrupt, while type II has a slow transition with a mixing state, see Fig. 3.22.

The type I are explained by the BCS theory, but up to now no theory can explain the type II superconductors. This second type is mainly complex metallic compounds and alloys. Recently it was discovered that some metal-oxide ceramics are superconductors at temperatures higher than 130 K. These high temperature superconductors are used in



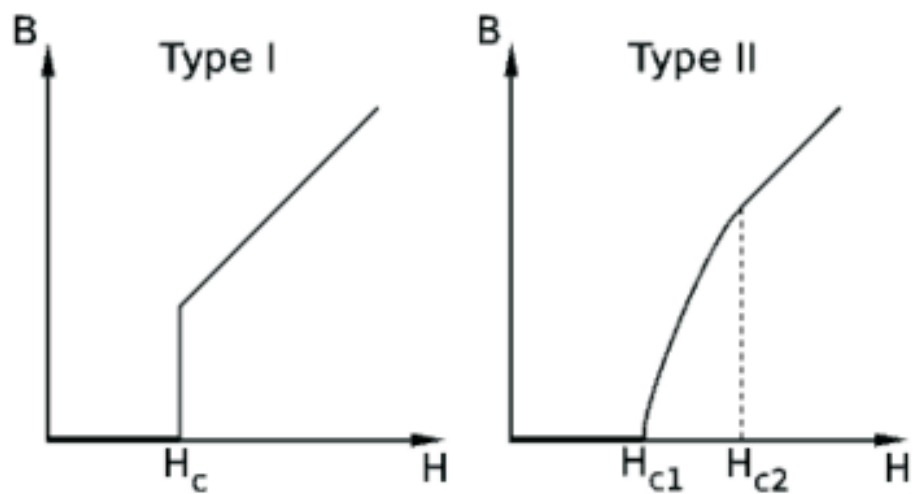


**Figure 3.22:** Variation of internal magnetic field ( $B$ ) with applied external magnetic field ( $H$ ) for Type I and Type II superconductors.

the frozen spin target to load the current to the superconductor internal holding coil. The holding coil is inside the cryostat at very low temperature and it must be connected to the outer power supply. If normal conductor wires were used they would load a lot of heat into the cryostat, and it would be very difficult to obtain the desirable low temperatures. Hence high temperature superconductors are used for this propose.

## 3.6 The Bonn Frozen Spin Target

This section will briefly describe the Bonn frozen spin target setup used in 1998 for the GDH experiment in Mainz [Bra99]. Data taken in this experiment will be presented in chapter 5.

### 3.6.1 Target Material

Since the sixties [Sch65] many different materials have been used as target for nuclear physics experiments. In [Goe02] is a table with the main characteristics of some of them. The important qualities for a good target material are: high degree of polarization, fast build up time, high relaxation time, high dilution factor (ratio of free polarizable nucleons and the total amount of nucleons in the material), good resistance to radiation damage, and no presence of other polarizable nuclei.

In the GDH 1998 experiment in Mainz butanol ( $C_4H_9OH$ ) and deuterated butanol ( $C_4D_9OD$ ) were chosen as proton and deuterium target respectively. Carbon and oxygen are spinless particles and therefore they do not contribute to the asymmetry in the scattering process. The radiation damage was negligible at a photon beam intensity of  $5 \cdot 10^5 \gamma/s$ , for energies of the MAMI-B accelerator. The material was chemically endowed with 0.5 % by weight porphyrine dissolved in 5% water resulting in  $1.89 \cdot 10^{19}$  electron spins per  $cm^3$ . Taking this into account the dilution factor for butanol is  $d_{But} = 0.133$ , and  $d_{DBut} = 0.236$  for deuterated butanol. The target material was frozen into spherical beads of 2 mm size by shock freezing in liquid nitrogen. The beads were placed in a PTFE (polytetrafluorethylen) container of 2 cm in length and diameter. The effective filling factor was  $f=(63.3 \pm 0.7)\%$  [Roh04].

### 3.6.2 Refrigerator

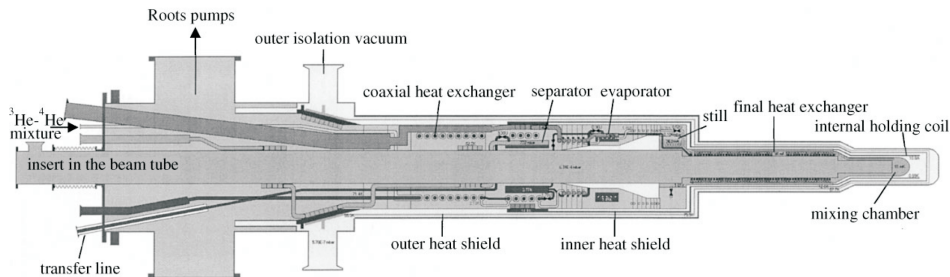


**Figure 3.23:** Schematic view of Bonn's dilution cryostat.

The requirements of the refrigerator are about 30 mW of cooling power around 300 mK during polarization mode for polarizing the 10 cm<sup>3</sup> target material, and it must reach temperatures below 70 mK for the frozen spin mode in order to achieve long relaxation times. It also has to fit geometrically into the DAPHNE detector and to allow maximum angular acceptance. A horizontal <sup>3</sup>He–<sup>4</sup>He dilution refrigerator that fulfills all these conditions was built in Bonn. It has two <sup>4</sup>He pre-cooling stages called *Separator* and *Evaporator*, that reach temperatures of 2.2 and 1.5 K respectively by pumping the vapor over a liquid <sup>4</sup>He bath. The outgoing gas cools the incoming <sup>3</sup>He, and thermally isolates the inner parts of the cryostat. In the mixing chamber temperatures of 40 mK are achieved by pumping the <sup>3</sup>He from the <sup>3</sup>He–<sup>4</sup>He mixture. The target container is mounted at the end of an insert that also contains the NMR coil and microwave guides. This insert allows a fast exchange of the target material.

Using an oil-free compressing Roots pumping system, <sup>3</sup>He circulations of 30 mmol/s are possible, which provides a cooling power of 50 mW at 300 mK. A base temperature of 40 mK was measured at a circulation rate of 1.4 mmol/s. In the frozen spin mode the refrigerator was usually operated at 50-60 mK with a cooling power of a few microwatts. The total liquid <sup>4</sup>He consumption amounted to 7 l/h during cooling down and 5 l/h in the frozen spin mode.

### 3.6.3 Polarizing Magnet

The magnetic field for the polarization build-up was provided by a superconducting solenoid coil built by the Saclay group. It was used in the experiment E704 at Fermilab [Cha90]. It can achieve up to 6.5 Tesla with a homogeneity of  $\Delta B/B < 10^{-4}$ . It runs in nonpersistent mode at a current of 70A producing 2.5 Tesla. The magnet is mounted on a railway system that allows a quick and reproducible positioning to enclose the static target during the polarization process, and a quick removal for data taking periods.

### 3.6.4 Internal Holding Coil

An internal holding coil placed inside the cryostat keeps the degree of polarization in the frozen spin mode when the external magnet is removed. It is wound in four layers of 1050 turns each on a copper carrier. It consists of a 100  $\mu m$  multifilament NbTi-wire insulated by 10  $\mu m$  varnish. The total thickness of the coil including the 300  $\mu m$  copper carrier amounts to only 780  $\mu m$ . Due to its low mass content the majority of outgoing particles are unaffected. It produces a 0.48 tesla magnetic field with a homogeneity better than  $10^{-3}$ , which allows for NMR measurements. The outer fringe field is less than 200 Gauss and it does not influence the detector nor the outgoing particles significantly .

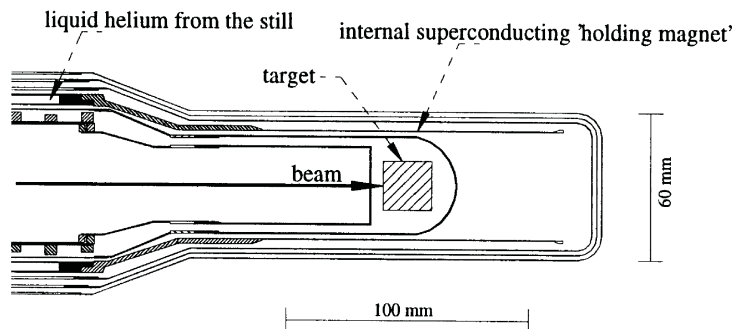


**Figure 3.24:** View of the front part of the refrigerator containing the internal holding coil.

### 3.6.5 Microwave System

For the DNP process microwaves with a stability of  $10^{-4}$  in frequency are needed to induce transitions between the Zeeman levels. For fast build-up time a power of 2-3 mWatt/cm<sup>3</sup> is required, which adds up to about 25 mW for a 10<sup>3</sup> cm<sup>3</sup> target volume. A carcinotron (Thompson CSF) was used as microwave source. It can provide up to 3.5 W of power at 70 GHz which corresponds to the electron Larmor frequency at 2.5 Tesla. The microwaves are conducted to the refrigerator by a rectangular waveguide, which is oversized to minimize power losses. The mixing chamber acts as a cylindrical multimode cavity of 39 mm diameter. During the DNP process the frequency is modulated in a bandwidth of 20 MHz with a frequency of 1 kHz, to increase the degree of polarization by 3% and to accelerate the build-up time.

### 3.6.6 NMR System

A nuclear magnetic resonance (NMR) system is used to determine the degree of polarization of the material [Rei95]. For this purpose a coil is placed around the target cell. For detecting the proton signal a one turn coil with inductance of about 75 nH is used, while in the case of the deuteron an eight turns coil with 440 nH of inductance was built. It is necessary because of the small deuteron signal due to its smaller magnetic moment compared to the proton. The coil acts as a probe in an RF circuit that measures the Q value. It is driven at the nucleus Larmor frequency to induce transitions between the nucleon Zeeman levels. Changes in the degree of polarization will induce changes in the susceptibility  $\chi(w)$  of the material and this will modify the impedance  $Z(w)$  of the coil, that can be seen by the Q-meter, see Eq. 3.22.

### 3.6.7 Control System

The computing control system of the target setup can be detached in 3 parts: NMR, slow control and Programmable Logic Controllers (PLC). The fast NMR measurement requires a high speed data acquisition with excellent precision to ensure a high accuracy in a short time of measurement by the signal-averaging method. The slow control of the cryostat, microwave system and superconducting magnet contains a variety of devices such as frequency counters and generators, power supplies, level meters, pressure gauges, mass spectrometers and resistance bridges for the measurement of temperatures, etc. All these devices must be controlled and monitored at any time. The automatization of the critical processes concerning the vacuum system, the polarization magnet and the  $^4\text{He}$  support are controlled by Programmable Logic Controllers (PLC). The three data acquisition and supervision systems are integrated in an intuitive graphical user interface developed in G, the object-oriented graphical programming language of LabView.

## 3.7 The Mainz Frozen Spin Target

This section will explain the new Mainz frozen spin target (MaiFroST). This new target will be used together with the Crystal Ball detector in order to perform double polarization experiments, that will bring new information about the spin structure of the nucleons.

As it was shown in section 3.5, to polarize a target material high magnetic fields and low temperatures are required. Temperatures in the mK range are achieved with a dilution refrigerator. It should fit in the geometry of the Crystal Ball detector, therefore has to be horizontal and with a well defined maximum radius. A superconducting magnet provides a magnetic field of up to 5 T with high homogeneity. A microwave system enlarges the degree of polarization via the dynamical nuclear polarization (DNP) method. A developed nuclear magnetic resonance (NMR) system will provide an accurate measurement of the degree of polarization. The next sections will present the different parts of the Mainz frozen spin target, and its actual status.

### 3.7.1 Refrigerator

The horizontal dilution cryostat was developed in close collaboration with the polarized target group of the Joint Institute for Nuclear Research, JINR, in Dubna, Russia, which has a lot of experience in building this kind of refrigerators ([Neg66], [Neg68], [Leh95], [Baz98], [Uso04]).

Fig. 3.25 shows a schematic view of the cryostat. The  $^4\text{He}$  pre-cooling system is pictured in blue, and the  $^3\text{He}$  line in green color.

The outgoing helium gas is collected in a reservoir container and afterwards liquified

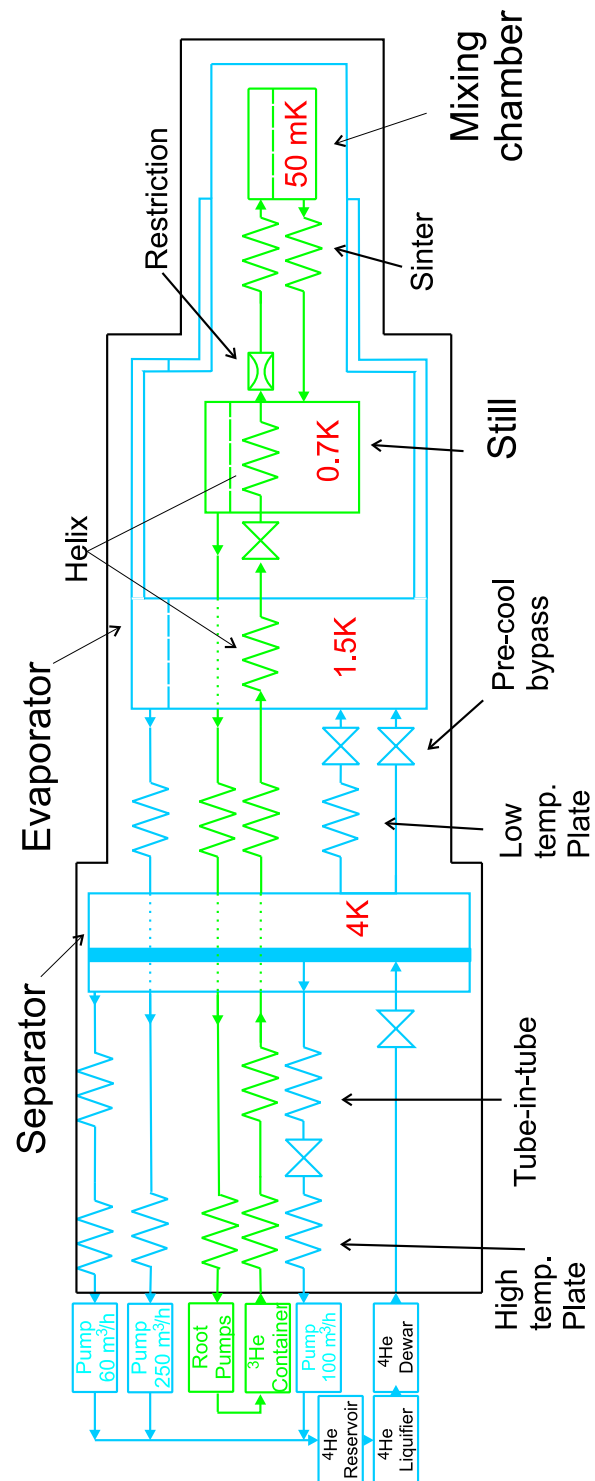


Figure 3.25: Schematic view of the Dubna-Mainz dilution cryostat.

in a standard Linde liquifier.  $^4\text{He}$  is inserted from a Dewar into the *separator*. A needle valve controls this flow. In this vessel the helium is separated in gas and liquid phases. A superconducting wire is used to measure the level of liquid helium. One 60 m<sup>3</sup>/h rotary pump circulates the gas through different heat exchangers attached to the external shield to thermally isolate the inner part of the cryostat. Another 100 m<sup>3</sup>/h rotary pump reduces the vapor pressure from above the liquid, cooling down the separator. This outgoing gas pre-cools the incoming  $^3\text{He}$  gas in two steps with some high temperature and tube-in-tube heat exchangers (HE) (see next section). One needle valve manages the outgoing flow between the two HEs.

Liquid helium from the separator can move to the *evaporator* pot via a HE, where the incoming  $^3\text{He}$  is liquified, or directly through a bypass for the cool down process, since the flow resistance of the HE is too high for warm gas. Two needle valves rule these possibilities. As in the separator, the level of liquid is measured with a superconducting wire. The temperature in the evaporator is reduced down to about 1.5 K by exhausting helium with a 250 m<sup>3</sup>/h rotary pump. This gas is also used to cool down the incoming gas. The evaporator surrounds the *still* vessel and thermally isolates it.

The incoming  $^3\text{He}$  liquid passes through an helix immersed in the cold helium of the evaporator and another one inside the still. Behind the still are ten sintered heat exchangers (Fig. 3.29) that reduce the temperature of the liquid  $^3\text{He}$  as much as possible before it enters the *mixing chamber*. Where the diluted-concentrated phase separation is produced and the lowest temperatures are achieved. Liquid from the diluted phase goes to the still via the sintered heat exchangers pre-cooling the incoming  $^3\text{He}$ .

A heater is placed in the still to evaporate the liquid. This gas is pumped out by powerful roots pumps, and in its way out it cools the whole cryostat. After the roots pumps the warm gas is re-injected and the continuous process starts again.

## Heat Exchangers

As it was explained in section 3.5.5 the design of the heat exchangers (HE) is of major importance. The lowest temperature attainable and the stability of the cryostat depend strongly in the capacity of heat transfer from the outgoing cold fluid to the incoming warm helium.

Depending on the temperature gradient and the absolute temperature different designs of HE are used. Fig. 3.26 shows a schematic view of the high temperature heat exchangers, that pre-cool the gas from room temperature to about 4 K. The tube with the incoming  $^3\text{He}_C$  is welded to the capillary that carries the outgoing  $^4\text{He}_{sep}$  gas from the separator. Both tubes are fixed to a machined copper block which has a special shape that maximizes the surface area in contact with the  $^3\text{He}_D$  gas pumped out from the *still*. Additionally  $^4\text{He}_{ev}$  gas coming from the *evaporator* moves out in an inner tube that runs parallel to the axis of symmetry and it is also anchored to the copper blocks. It isolates

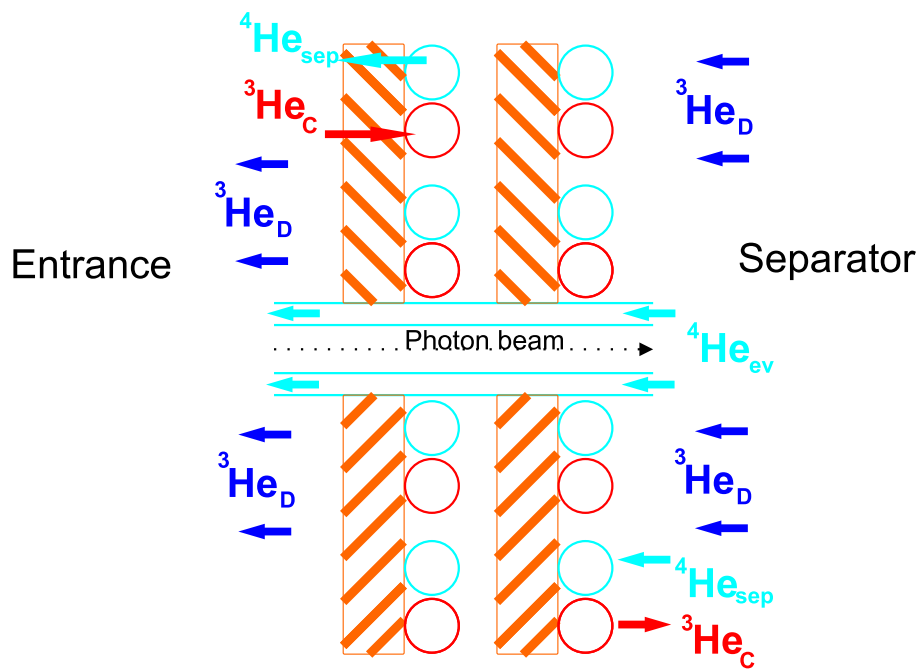


**Figure 3.26:** Schematic view of the high temperature heat exchangers.

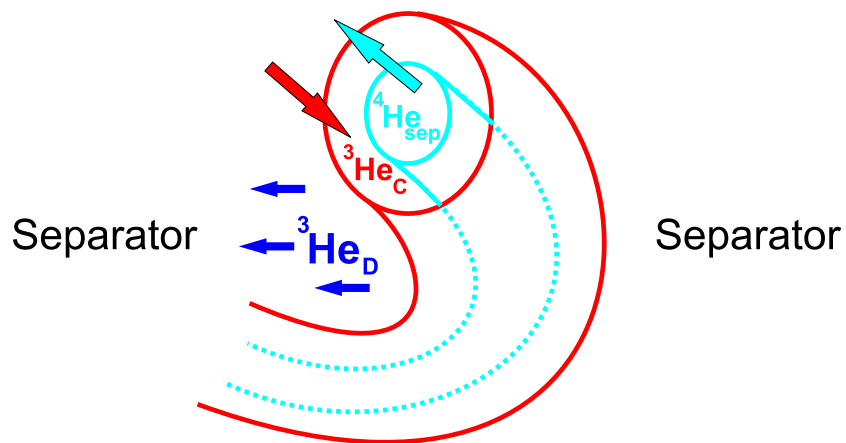


**Figure 3.27:** Schematic view of the tube-in-tube heat exchangers located around the separator.



the incoming gas from the center part of the cryostat where the insert will be placed. Careful calculations were performed to design the heat exchangers and to estimate the number of them needed. In Fig. 3.26 only 2 blocks are illustrated, but a total of 7 are employed to cool down the gas from 300 K to about 4 K.

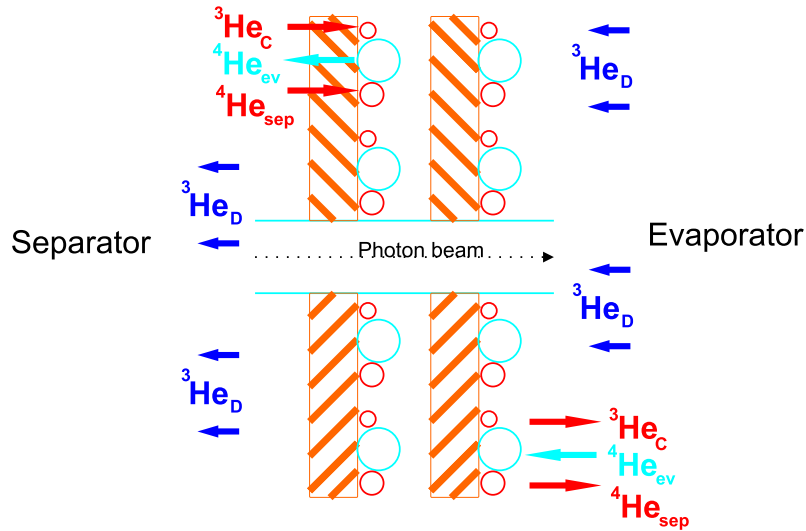


**Figure 3.28:** Schematic view of the low temperature heat exchangers to reduce the temperature from 4 to 1.5 K.

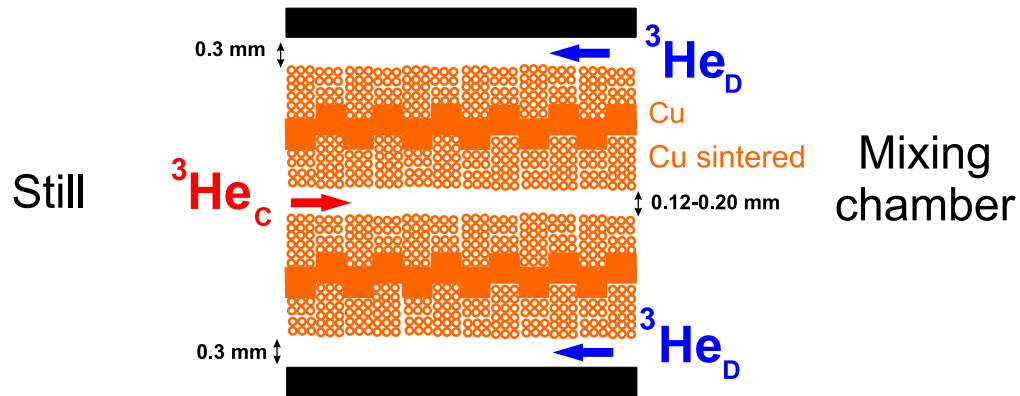


**Figure 3.29:** Low temperature heat exchanger made with sintered copper powder. The metal sponge increases the contact surface.

The second step is a tube-in-tube heat exchanger consisting of two concentric capillaries, Fig. 3.27. Heat is transferred across the body of the wall, and conduction along the capillary and along the liquid streams are negligible. The warm  ${}^3\text{He}_C$  moves in the space

between the tubes and  ${}^4\text{He}_{sep}$  coming from the separator goes out through the inner tube. This HE is placed between the *separator* pot and the inner tube where  ${}^4\text{He}_{ev}$  gas coming from the *evaporator* moves out.

A schematic view of two HEs that reduces the temperature from 4 to about 2 K is shown in Fig. 3.28. Tree tubes are spiralled and attached to a copper block cooled by the  ${}^3\text{He}_D$  gas coming from the *still*. The biggest tube contains outgoing cold  ${}^4\text{He}_{ev}$  gas from the *evaporator*. The warm  ${}^4\text{He}_{sep}$  from the *separator* moves through one of the capillaries, if needed it can also go directly to the *evaporator* via a bypass.

The incoming  ${}^3\text{He}_C$  moves into the third tube where it starts to liquify at around 2.5 K. Four of these HE are located between the *separator* and the *evaporator* vessels. The liquified  ${}^3\text{He}_C$  pass first through an helix inserted in the liquid  ${}^4\text{He}_{ev}$  of the evaporator and then to a second helix placed inside the still in order to reduce its temperature to about 0.7 K. At very low temperature the Kapitza resistance,  $R_k$ , (Eq. 3.41) between helium and the metals becomes the limiting factor. To overcome this problem heat exchangers with large surface contact areas are required. Sintered metal powder is added to the inner part of the tubes. The important parameters of a sintered heat exchanger are surface area, thermal conductivity and bonding to its container. Fig. 3.29 shows the schematic view of a sinter heat exchanger used between the *still* and the *mixing chamber*. The inner capillarity contains the warm  ${}^3\text{He}_C$ , while the outgoing  ${}^3\text{He}_D$  from the diluted phase of the mixing chamber moves in the external part. This design maximizes the heat contact. Ten of these HE are placed between the *still* and the *mixing chamber*.

### Internal Holding Coil

As in the Bonn cryostat design the new Mainz Frozen Spin target will have an internal superconducting holding coil. It was produced in the Mainz workshops. It is made of  $0.227\ \mu\text{m}$  NbTi wire type F54 1.35(0.20)TV from the company ERS, and composed of four layers each of them with 600 turns around a 0.3 mm copper holder of 47.7 mm diameter. Magnetic fields up to 0.7 Tesla will be possible before the critical current  $I_c$  of the wire is reached. The coil will be refrigerated by liquid helium from the evaporator vessel.

A power supply able to produce up to 70 A will control the holding coil. To load the required current from the power supply at room temperature to the coil at about 1.5 K a high temperature superconducting wire from the company Trithor is used. The material employed is TT-gold composed of BSCCO ceramic in a matrix of AgAu with an outer sheath of reinforced AgAu alloy. It has a critical current of  $I_c = 50$  A at 77 K. It is 4.0 mm wide and 0.25 mm thick.

### 3.7.2 Polarizing Magnet

In order to polarize the target material a superconducting magnet able to produce up to 5 Tesla with a central homogeneity of  $\Delta B/B \leq 10^{-4}$  is used. The high compact field solenoid consists of a single block of multifilamentary NbTi wound onto an stainless steel former. The conductor is casted in epoxy resin to eliminate wire movement. The inductance of the coil is 17.5 H. It is immersed in a bath of liquid  $^4\text{He}$ . Radiation heat load is minimized by the use of high purity aluminium nitrogen-cooled radiation shield, and multi-layer superinsulation enclosed in vacuum.

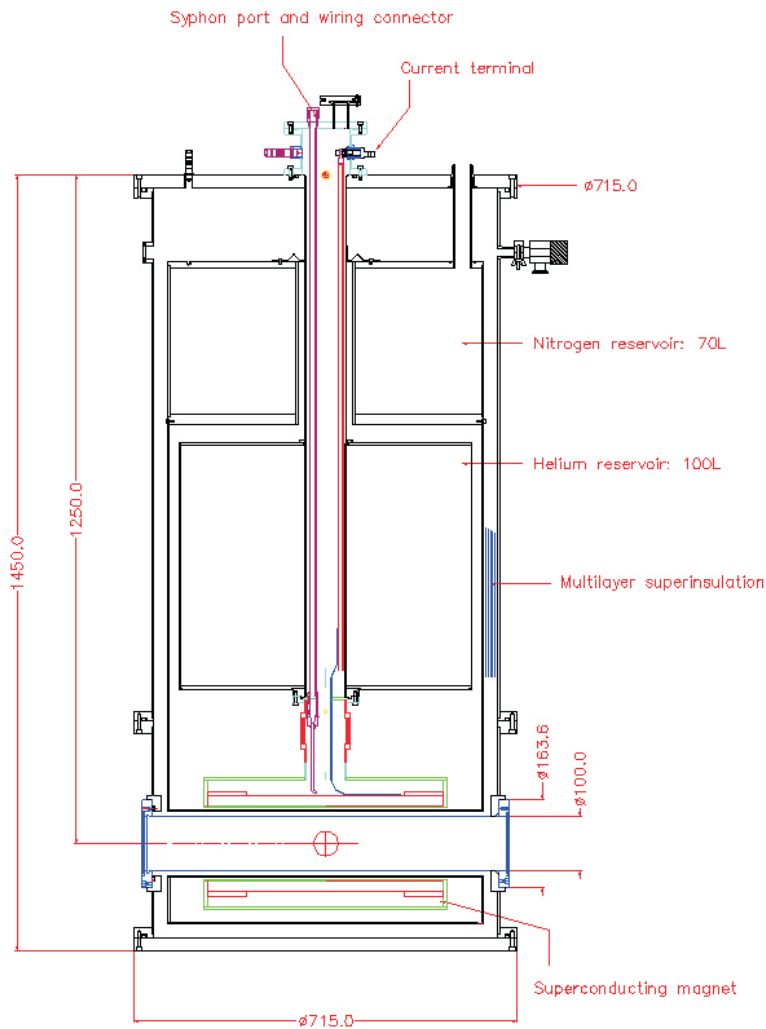


**Figure 3.30:** Polarizing magnet.

The magnet contains a 70 liter nitrogen storage dewar, and a 100 liter liquid helium reservoir monitored with an helium level meter HLG200/210 with a probe type 250 from Cryogenic Limited. The construction is as shown in the general assembly drawing Fig. 3.30. Three RhFe thermometers, with a well defined response between 300 and 4.2 K, attached to the superconducting coil, the helium reservoir and the insulation respectively provide an immediate indication of temperatures from four terminal resistance measurements.

The magnet control system was developed mainly by the company Cryogenic Limited. The power supply able to produce the 97.06 Amps needed to achieve 5 T incorporates a sophisticated microprocessor unit, with all operations monitored through the internal firmware. It is connected to a PC via an IEEE-488 interface, and it is fully controlled by a LabView program. The ramping speed and maximum current can be set, and the induced magnetic field is continuously displayed. The temperature sensors and the helium level gauge are verified at any time by the program.

A superconducting persistent mode switch is connected in parallel to the magnet coil and wired to the main input/output current terminals. Resistive heaters wound into the switch enable it to be either resistive or superconducting.

The outer magnetic field was simulated and successfully compared with measurements. Figure 3.31 shows the simulated field. As one can see just 20 cm away from the center of the coil less than 10 Gauss are measured, therefore, no electromagnetic devices will be affected by it.

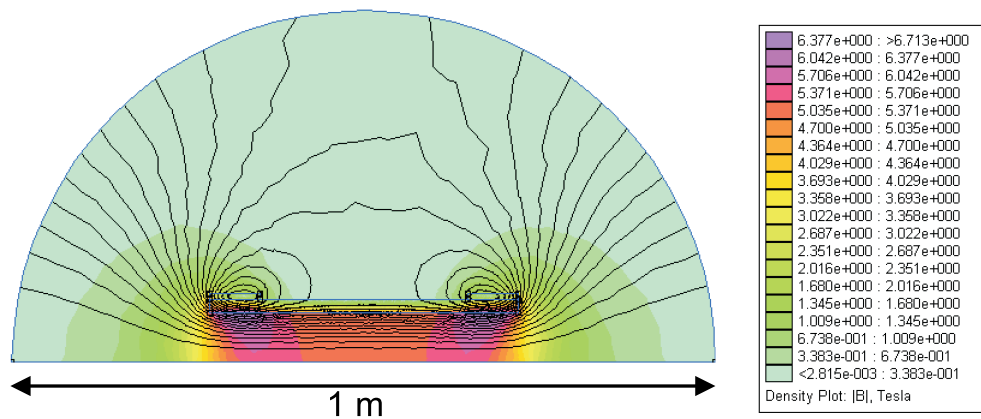


**Figure 3.31:** Simulated external magnetic field.

About 100 liters of liquid nitrogen are initially needed to cool the shielding. It takes around 10 hours to cool it down from room temperature to 100K. After 3 days the rest of the magnet is below 200 K. The  $^4\text{He}$  reservoir and the solenoid container are then pre-cooled by a small amount of liquid nitrogen within 1 hour. With the system pre-cooled

and all nitrogen expelled, liquid helium can be transferred into the dewar via the siphon port. In about 3 hours the magnet coil reaches temperatures of 4.2 K and the reservoir container starts to fill. It is also possible to pre-cool the magnet using only the liquid nitrogen shielding container. This method avoids the complicated process of extracting the nitrogen from the helium pot. If the nitrogen container is filled for at least 7 days temperatures below 150K are achieved in the magnet can and in the helium reservoir. The helium consumption of the magnet is less than 1 m<sup>3</sup>/h gas in stable operation, and about 1.5 m<sup>3</sup>/h when it is operated at magnetic fields of 2.5T.

The magnet was manufactured by Cryogenic Limited (job number 1879) and delivered in 2002. In the last years it was successfully used by the X1 group of the KPH Institut in Mainz. For more technical details refer to [Roc02].

### 3.7.3 Microwaves System

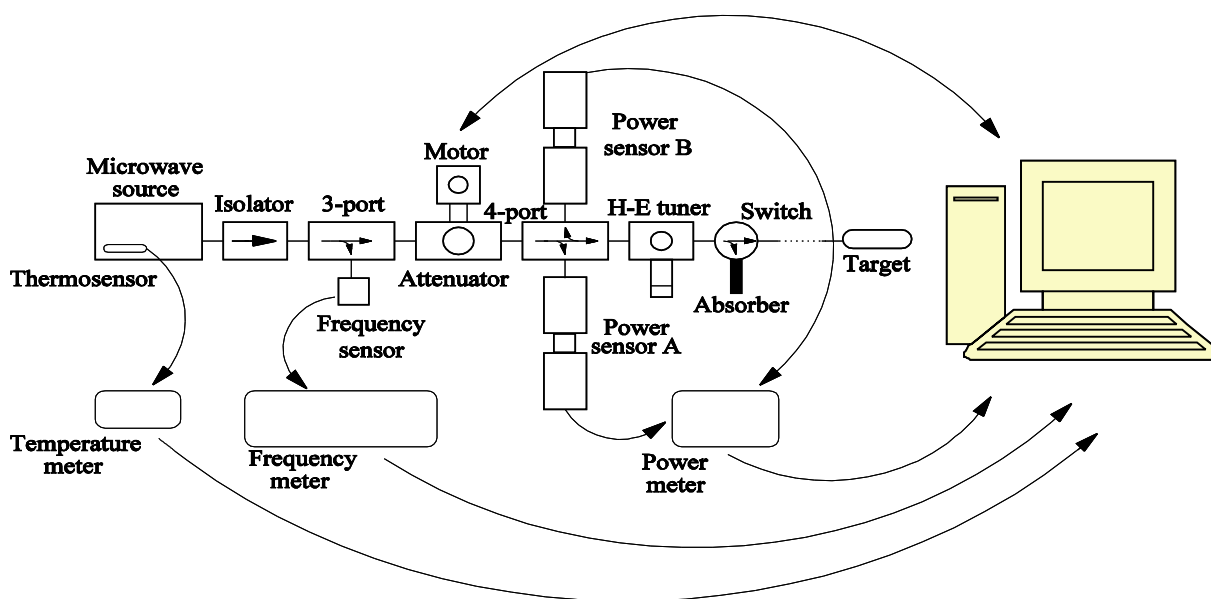


Figure 3.32: Microwave system.

The microwave system was developed in the frame work of a diploma thesis [Mar03]. It was designed, tested and successfully used for the Mainz GDH experiment on the neutron in 2003. Since then some minor changes have been made. The system was tested again for the new FST, and the software was slightly modified to be included in the complete target control system.

Figure 3.32 shows the schematics of the system. A Varactor IMPACTT (IMPact ionization Avalanche Transit-Time) diode is used as microwave source. It is able to deliver about 150 mWatt with a central frequency of 70 GHz tunable around  $\pm 200$  MHz by an external power supply. This corresponds to the Larmor frequency of the electron in a magnetic field of 2.5 Tesla. The corresponding Larmor frequency of the proton and the deuteron for this magnetic field is 106 MHz and 16 MHz respectively. As a rough number the required power at temperature of 1 K is 2 mW/g of target material at 2.5 T, and 20 mW/g at 5T [Goe02]. An additional source was bought and successfully tested. Figures 3.33 and 3.34 display the frequency and power dependence on the applied external voltage for both IMPATT diodes.

A frequency counter 598A from Phase Matrix, Inc. gives a reliable frequency value. It can measure continuous signals from 100 Hz to 170 GHz, and perform pulsed measurements from 250 MHz to 170 GHz. It is steered via a GPIB connection by a computer. Its data are processed in a LabView program that controls the total setup. This frequency counter uses the YIG Preselected Heterodyne Down Conversion technique. A spectrum analyzer type preselector prevents harmonics and other spurious signals from interfering with the measurement of the desired signal. Additionally, it totally eliminates noise. The YIG (Yttrium Iron Garnet) filter provides effective power limiting to protect against burnout and does not reduce sensitivity.

The system also contains two sensors V8486A and an E4419B EPM Series Power Meter from Agilent Technologies. They measure incoming and reflected microwave power. They are connected to the computer via a GPIB cable and the signals are processed by the LabView program. With this setup it is possible to control and monitor the power, and save all data for later analysis. The time needed to polarize the target material is depending on the power, the optimum power can be tuned using an attenuator. This attenuator controls the power fed into the target material, while the frequency is adjusted by the applied voltage. The attenuator used in the present setup is flag shaped and can attenuate up to 30 dB. It is controlled by an external micrometer. Finally an H-E tuner matches the impedances of the microwave generator and the transmission waveguide to the cryostat cavity.

A frequency generator modulates the control voltage applied to the source, and therefore the microwave signal. This can improve the maximum degree of polarization and the polarization rate [Ade96].

Oversized wave guides transport the microwave power from the source to the cryostat. In there circular wave guides of 4.5 mm in diameter transport the signal to the mixing chamber where the target material is placed. The mixing chamber acts as a resonant cavity.

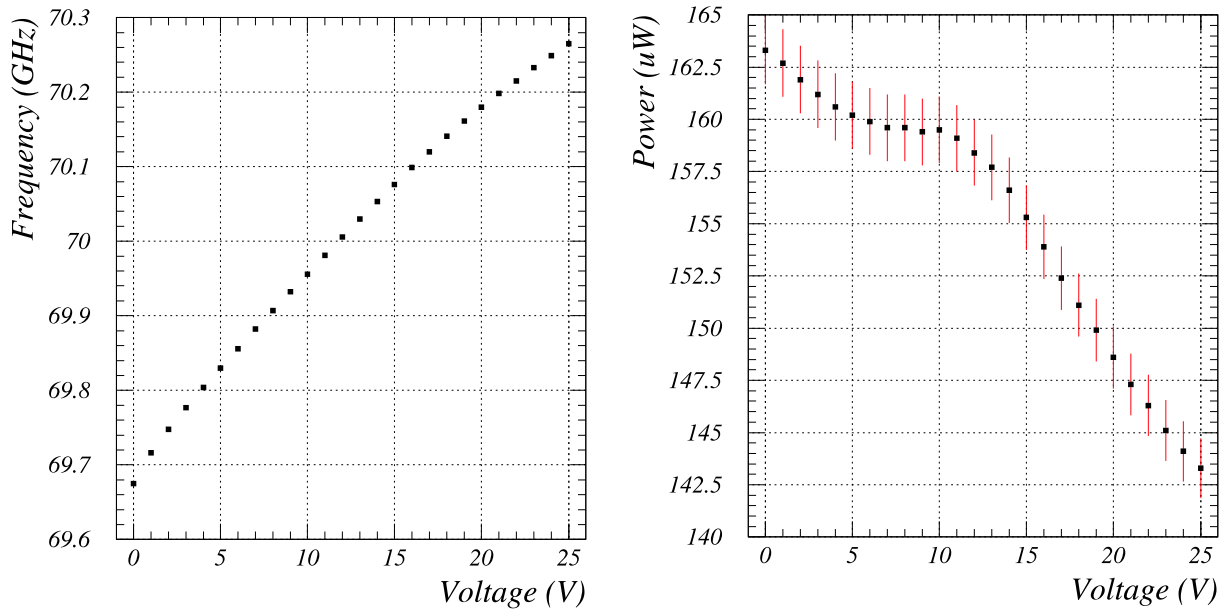


**Figure 3.33:** Frequency and power of the old microwave source versus the applied control voltage.

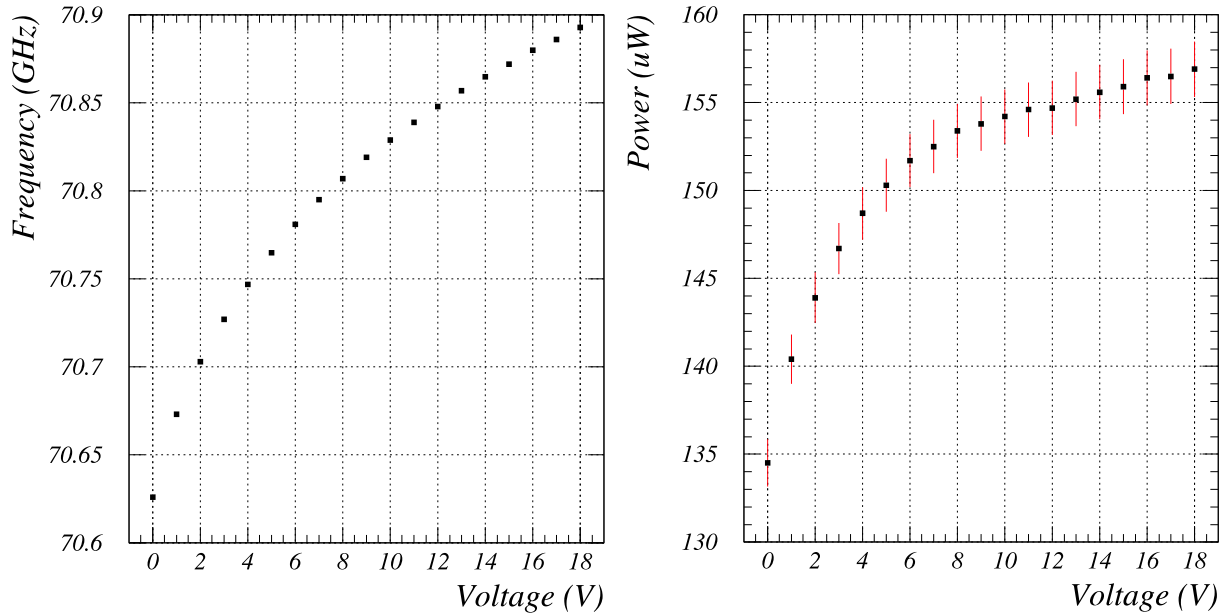


**Figure 3.34:** Frequency and power of the new microwave source versus the applied control voltage.

### 3.7.4 NMR System

The Nuclear Magnetic Resonance System used to determine the degree of polarization of the target material is currently under development in close collaboration with groups from Zagreb and Bochum.

A signal generator from Rohde & Schwarz able to produce signals from 5 kHz up to 1.5 GHz is used. Different radio frequency components from the company Mini-circuits are used to create the circuit that amplifies the signal and processes it. The processed signal goes via a PCI-68M I/O M-series board from National Instruments to the PC, where a self developed LabView program reads and analyzes it.

### 3.7.5 Control System

The subsystems of the frozen spin target have different requirements from the fast NMR read out to the slow control of the cryostat. Another important task is given by security considerations. In case of a failure the cryogenic liquid, used in the system, may evaporate very fast causing spontaneous overpressure. The main idea is to have a modular control for each subsystem integrated in the same software in order to allow easy data transfer from one to the other. Each of the NMR, magnet, and microwave systems have a dedicated Windows PC with LabView software from National Instruments installed on it. In the previous sections an explanation of each part was given, in here the attention will focus on the complex cryostat control system. It also has different subsystems that will be shown in detail in this section.

#### Cryostat

In order to control and monitor the dilution cryostat sensors, pumps and valves are used. The schematic idea is shown in Fig. 3.35. The temperature inside the cryostat is monitored with sensors read by an AVS resistor bridge and a digital voltmeter. The gas flow in the different stages of the refrigerator is managed with 5 needle valves each of them operated by a step motor. Three Simatic CPUs handle the rest of the valves, pressure gauges, flow meters, and pumps. One CPU operates the Roots Pumps unit, another runs the  $^4\text{He}$  pre-cooling stage and the last one takes care of the  $^3\text{He}$  line. The CPU of the Roots pumps acts as master and it is connected to the two slaves via Profibus, and to the computer by an MPI cable. Each CPU has some modules for Digital Input/Output and Analog Input/Output signals, as well as an RS232 connector port. These modules are connected to the CPU that runs the Simatic Step7 control software. An intuitive LabView interface was created, where all the parameters are shown. Step7 and LabView are connected using AGlink software. In the next subsections a detailed explanation of the different subsystem is given.



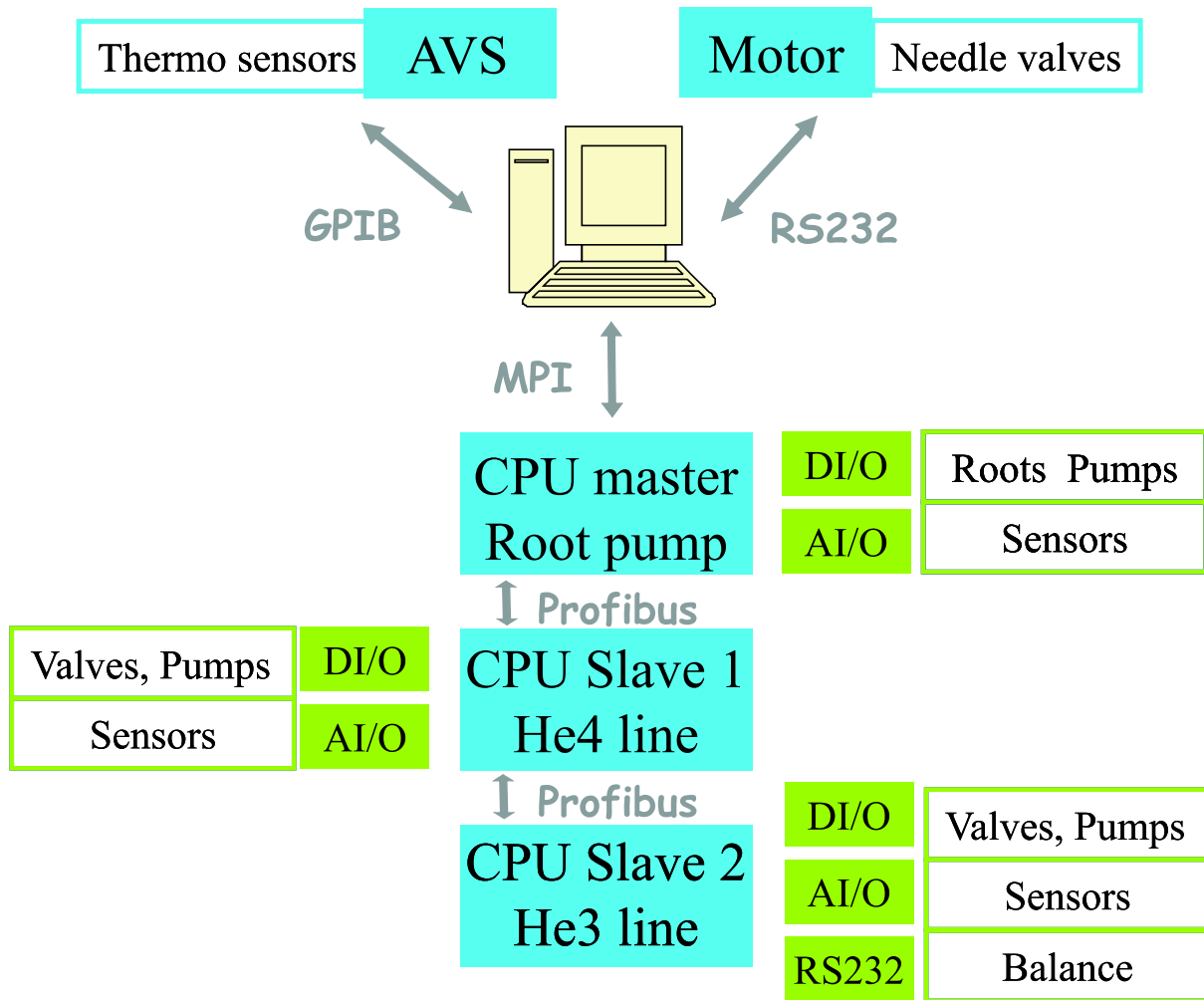


**Figure 3.35:** Schematic view of the cryostat control system.

### Temperature Measurements

The temperature monitoring of the cryostat is done by many secondary thermometers. One calibrated RuO and different PT100, Allen Bradley, Speer and TVO resistors are used. AVS resistor bridges measure the resistance precisely and without disturbing noise. A Keithley digital voltmeter monitors the less important sensors. Both AVS and voltmeter are connected to the computer via GPIB, and the LabView program reads the values. The AVS resistor bridge is optically coupled with the computer to avoid the influence of the GPIB bus clock frequency.

### Needle Valves

The cryostat has 5 needle valves in different positions for gas flow control. Each of these valves is driven by a step motor, from the company Portescap, controlled by a programmable IPS110 mother board from Technosoft. It was developed a LabView interface that can be used to set the position of the needle valve in order to optimize the cryostat functioning.

### $^4\text{He}$ Pre-cooling Stage

The pre-cooling stage has two parts: the *separator* and the *evaporator*, it was developed in the framework of a Diploma Thesis [Mou04]. Fig 3.36 shows the pumping system. In this figure the electropneumatic valves and the manual valves are represented by an  $E$  and a  $V$ , respectively. The pressure sensors are denoted by an  $M$  and the flowmeter by  $FLM$ . As one can appreciate there are three symmetric parts, two on the right for the separator and one on the left for the evaporator. The last one will be explained in detail.

The main line follows the valves E46, E43 and E40. The 250 m<sup>3</sup>/h pump removes  $^4\text{He}$  from the cryostat, it passes through the flow meter FLM4 and it goes to a container where it is stored and later on liquified. A bypass of the valve E46 controls the flow of helium. This bypass contains the electropneumatic valve E47 and the valve V47 that can be regulated manually. The difference in pressure between M41 and M42 sensors gives an estimation of the flow and it is used to optimize the cryostat. Sensor M40 shows the pressure after the pump. Valves E42 and E44 are for security reasons connected to air, while valve E45 allows injection of  $^4\text{He}$ . The whole system has an automatic and manual bypass with valves E48 and V48 respectively for security reasons.

The evaporator has a powerful Rotary pump of 250 m<sup>3</sup>/h, thus temperatures of about 1.5 K are achieved. The set up is also composed of 3 pressure sensors, 1 flow meter, 9 electro-pneumatic valves and 2 hand valves.

The separator has 2 rotary pumps of 100 and 60 m<sup>3</sup>/h to pump the  $^4\text{He}$  gas and it reaches temperatures of about 4 K. It has 6 pressure sensors from the WIKA company and 2 Hasting mass flow meters to monitor the circulation of the gas. 18 electro-pneumatic

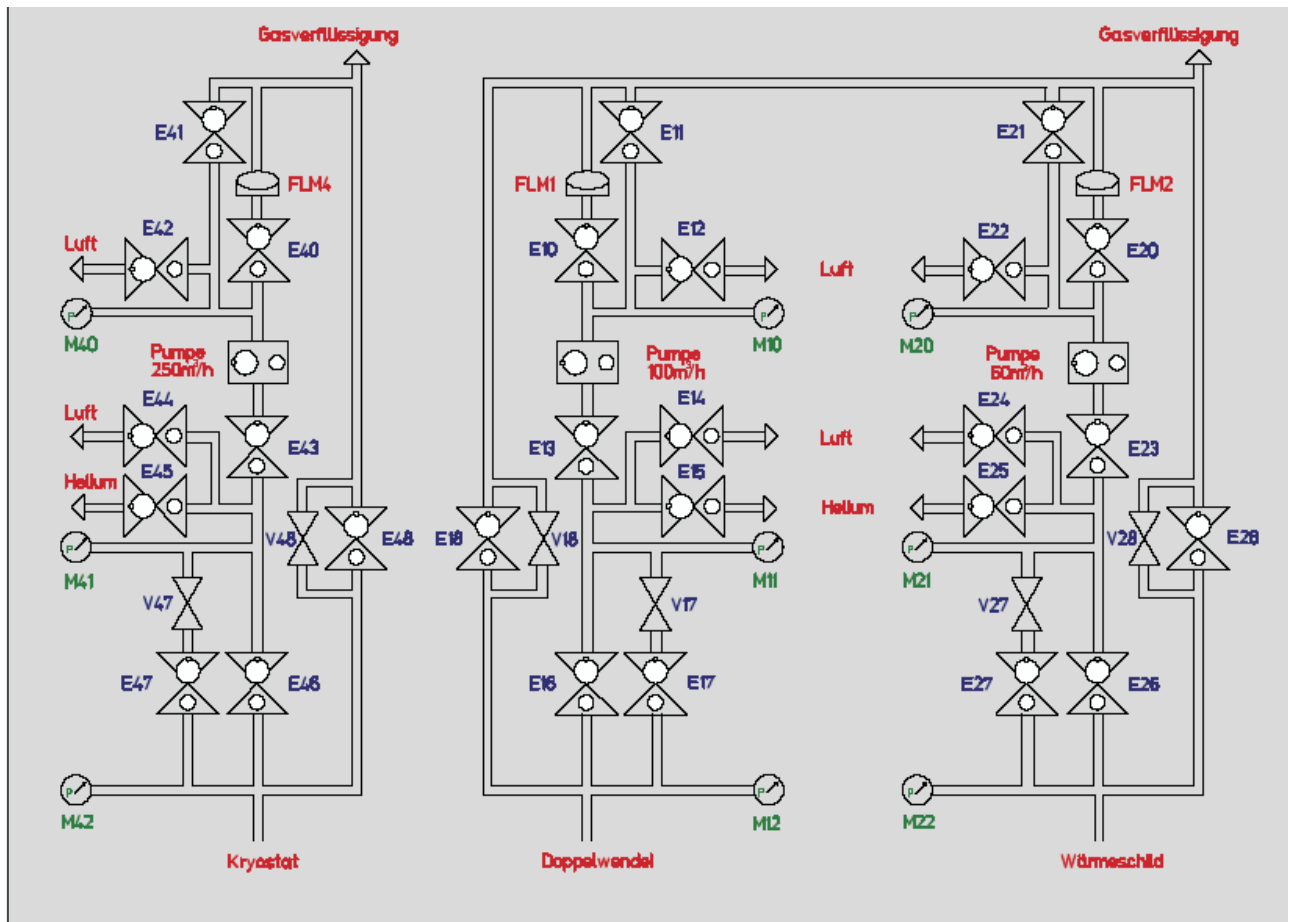


Figure 3.36:  $^4\text{He}$  pre-cooling line control system.

valves from Pfeiffer Vacuum control the system, 2 additional hand valves are used to regulate the flow and another 2 hand valves are used in the bypass of the whole system.

All electro-pneumatic valves are connected to the simatic DI/O modules and can be opened automatically from the LabView interface, or manually by pushing a button in the control panel. Both manual and automatic panel show the actual status of each valve and they allow to open or close them. The pressure sensor, as well as the electric flow meters are connected to an analog input module which is controlled via a Simatic programmable logic controller (PLC).

### <sup>3</sup>He Circulation System

The flow diagram of the <sup>3</sup>He circulation system can be seen in Fig. 3.37. This section will explain the main features of it. For security reasons each electro-pneumatic valve has a manual valve attached to it. Before inserting any <sup>3</sup>He gas a good vacuum has to be archived. A rotary pump called EVAC1 and the roots pumps are used for this propose. Valve 37 is opened to evacuate the hole system. After pumping the recipient to a vacuum of below  $10^{-3}$  mbar the cryostat is precooled to about 1 K using <sup>4</sup>He. Later valves 50 and 51 open and allow <sup>3</sup>He and <sup>4</sup>He gas to go into the cryostat system through valves 52. The out coming gas from the refrigerator is pumped through the big valve V0 by the 5 stage roots pump system (4000...250). It goes via the valves 35 and 32.1 into a cooling trap, Fig. 3.38, used to clean the gas. Valves 31.1 give pass to the flow-meter and finally the gas enters the cryostat again via valve 30. In there it is pre-cooled, goes inside the mixing chamber, gets evaporated in the still, is pumped out by the roots pumps, and the process starts again. There is a parallel line through valves 32.2 and 31.2 that also contains a cooling trap. It is used when the first trap is too dirty. In this case the latter is warmed up and the gas is evacuated using the pump, EVAC2, via valves 33.1 and 33. When the run is finished a compressor, COMP, drives the gas trough valves 54 and 53 to the storage containers.

The whole system contains 39 valves, 1 flow meter, 4 pressure sensors, 4 rotary pumps, 2 cooling traps and the 5 roots pumps that will be explained in the next section.

### Roots Pumps

The five roots pumps and their Simatic control system where developed by the company Pfeifer Vacuum. They have a pumping speed of 4000 m<sup>3</sup>/h, 2000 m<sup>3</sup>/h, 1000 m<sup>3</sup>/h, 500 m<sup>3</sup>/h and 250 m<sup>3</sup>/h respectively. The rotation speed of the biggest one can be changed in order to control the <sup>3</sup>He flow. They are oil free pumps and the leak rate is about  $5 \cdot 10^{-5}$  mbar.l/s. Pressure sensors are connected before and after each pump to monitor the pressure difference. In order to avoid overheating of the compressed gas there are after the high pressure stages integrated water cooled gas coolers.

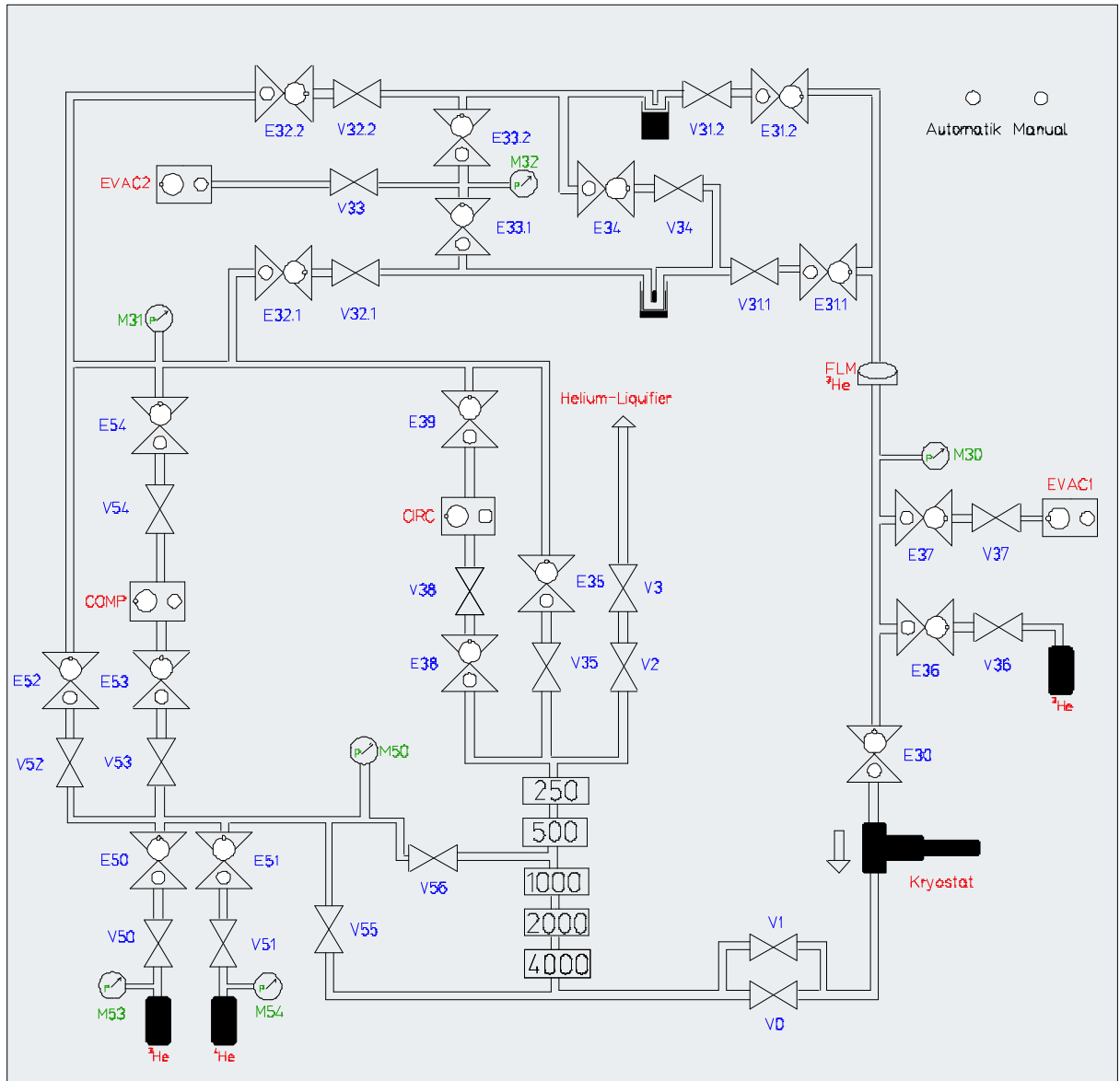
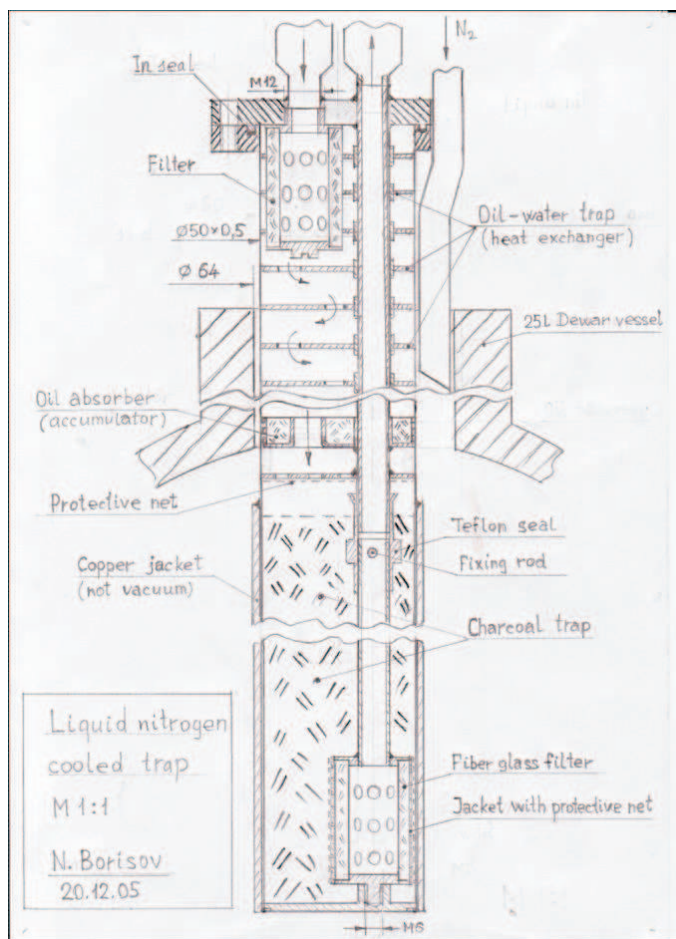


Figure 3.37:  $^3\text{He}$  circulation system.

### Cooling Trap System

A clean and pure  $^3\text{He}$  circulation is of major importance because oil, air or other gases could freeze inside the cryostat and produce important disruptions or damages. For this purpose a dedicated cleaning system was created. Fig. 3.38 displays a schematic view of the cooling trap. The gas flows through different stages where water, oil and other unwanted substances are filtered out. The trap is immersed in liquid nitrogen contained in an isolated dewar. The nitrogen level is weighed by an electric balance connected via RS232 port to a Simatic module. When the measured nitrogen weight is below a certain level the Step7 software of the CPU opens automatically a valve and nitrogen is refilled. It can be also filled manually.



**Figure 3.38:** Schematic view of the liquid nitrogen cooling trap.

### 3.8 Analysis of the Target Polarization in the GDH Experiment 2003

In summer 2003 the GDH experiment on the deuteron was carried out in Mainz. Deuterated butanol (D-Butanol) was chosen as polarized deuterium target. During the first run in June the material was doped with the standard Porphyrexid and polarizations around 35% were achieved. In July a new doping material, called Finland II, was discovered by the Bochum group. By adding 2.7% of this material in the deuterated butanol polarizations of more than 70% were obtained [Goe04b].

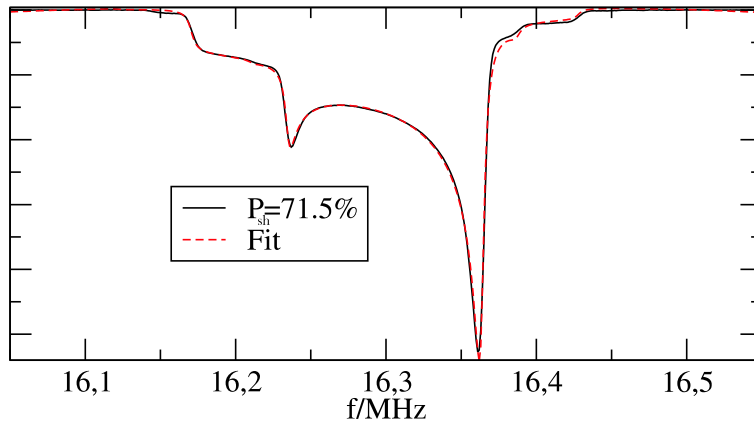


**Figure 3.39:** Example of an NMR signal during the GDH experiment 2003 in July. The black line is the signal, and the red dashed line is the theoretical fit from which the polarization can be obtained.

Using the asymmetric shape of the NMR signal the degree of polarization,  $P_{sh}$ , is obtained, as explained in section 3.5.3, from the line shape fit (Fig. 3.39). On the other hand the degree of polarization is also proportional to the area,  $AU$ , under this signal. If one plots the degree of polarization extracted by the line shape method versus area units (Fig. 3.40) for many NMR signals the proportionality factor  $C$  can be obtained.

$$P_{sh} = C * AU \quad (3.45)$$

Using this factor the degree of polarization is known directly from the measurement of the Area Units. The fits obtained for the June and July data taking runs are:

$$P_{june} = 0.00576(14) * AU \quad (3.46)$$

$$P_{july} = -0.0126(3) * AU \quad (3.47)$$

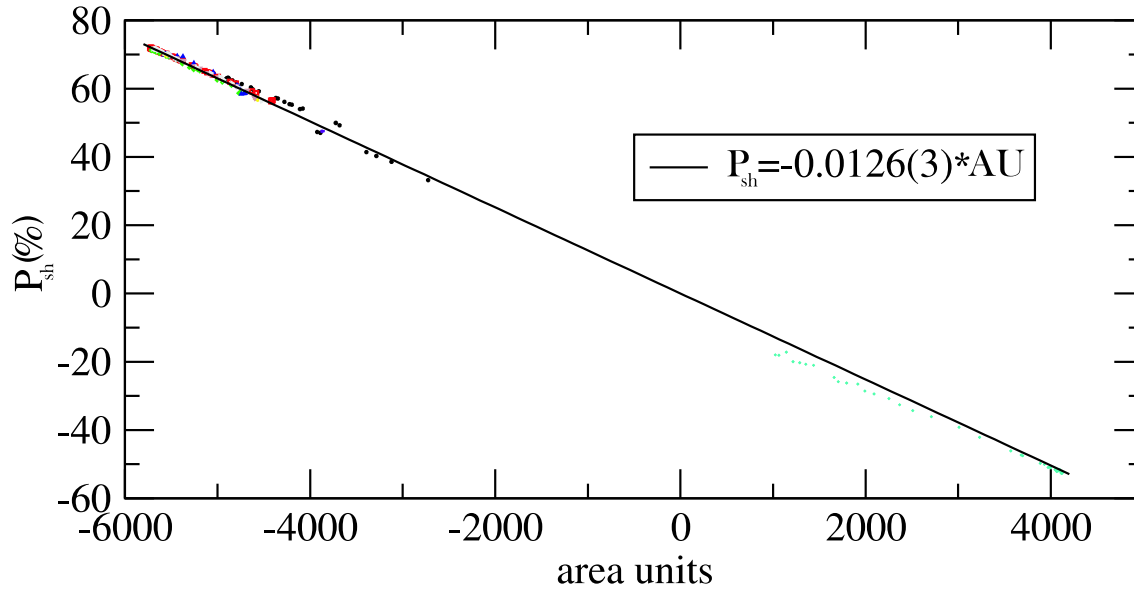


**Figure 3.40:** Fit between the degree of polarization obtained with the theoretical fit on the line shape and the Area Unit under the signal. It was obtained from many NMR measurements in the GDH experiment in Mainz during the run of July.

### 3.8.1 Polarization Analysis

This section will describe briefly the analysis of the target polarization. This parameter is of fundamental interest for the GDH sum rule, as well as for the different partial channels that can be studied with the experimental setup.

In section 3.5.4 the frozen spin principle was explained in detail, here only a short remark is given. First, in the so called *polarizing mode* the target is cooled down to about 300 mK and an external magnetic field of 2.5 T is applied. At this point microwave power is fed into the target in order to increase the degree of polarization via the DNP method. When the maximum degree of polarization is reached the microwaves are switched off and the temperature is reduced to 50 mK by going into *dilution mode*. At this moment the degree of polarization is measured 5 times and the average value calculated. This is the initial degree of polarization  $P_i$ . The external magnet is then removed and the internal holding coil provides 0.4 Tesla to keep the degree of polarization. The cryostat is in stable mode and the data taking can start. The polarization  $P$  of the target material decreases exponentially and can be calculated:

$$P = P_i e^{t/\tau} \quad (3.48)$$



where  $t$  is the time after the initial degree of polarization measurement and  $\tau$  is the relaxation time constant. It is obtained by measuring the final degree of polarization  $P_f$  at the end of the data taking cycle:

$$\frac{1}{\tau} = \frac{1}{T} \ln \left( \frac{P_i}{P_f} \right) \tag{3.49}$$

where  $P_f$  is the average value of 5 NMR measurements, and  $T$  is the duration of this cycle, typically 2 days. Table 3.5 shows the relaxation times for the different cycles.

Under the assumption that the temperature is stable the degree of polarization can be obtained from formula 3.48. The temperature was constantly monitored by many different sensors, and no significant fluctuations were detected in any of the 12 polarization cycles.

Approximately each hour a new data file was taken. A degree of polarization value for each data file was calculated using the formula 3.48. The starting time of each data file is contained in the file itself. Since the relaxation time is about 200 hours (see table 3.5) the degree of polarization changes less than 0.5% within one hour, therefore only one value per data file was given.

### 3.8.2 Error Calculations

The main source of error is coming from the determination of the constant  $C$  from the fit  $P_{AU}$  versus  $P_{AS}$ , it is about  $\Delta C \approx 2.5\%$ . The error in the determination of the  $P_{AU}$  is minimized by averaging 5 measurements and it is about 2 orders of magnitude smaller than  $\Delta C$ . The error of  $P_i$  and  $P_f$  are given by:

$$\Delta P = \sqrt{\left( \frac{\partial P}{\partial C} \Delta C \right)^2 + \left( \frac{\partial P}{\partial P_{AU}} \Delta P_{AU} \right)^2} \cong P_{AU} \Delta C \tag{3.50}$$

The error in the determination of the relaxation time constant  $\tau$  arise from the error in the determination of  $P_i$ ,  $P_f$  and in the measurement of the duration of each polarization cycle  $T$ , which is about 1 minute. It is 2 orders of magnitude smaller than the error of the determination of the polarization.

$$\Delta \tau = \sqrt{\left( \frac{\partial \tau}{\partial P_i} \Delta P_i \right)^2 + \left( \frac{\partial \tau}{\partial P_f} \Delta P_f \right)^2 + \left( \frac{\partial \tau}{\partial T} \Delta T \right)^2} \tag{3.51}$$

Once these errors are calculated the error of the degree of polarization for each data run is coming from the determination of  $P_i$ ,  $P_f$  and the time  $t$  in which this file was recorded. This time  $t$  is given by the computer that takes the data file and its error is negligible compared to the errors of the initial and final degree of polarization measurements. With equation 3.48 and 3.49 one can write:

$$P = P_i \exp \left[ \left( \frac{1}{T} \ln \frac{P_i}{P_f} \right) t \right] \quad (3.52)$$

So the error for each data taking file is given by:

$$\Delta P = \sqrt{\left( \frac{\partial P}{\partial P_i} \Delta P_i \right)^2 + \left( \frac{\partial P}{\partial P_f} \Delta P_f \right)^2 + \left( \frac{\partial P}{\partial t} \Delta t \right)^2} \quad (3.53)$$

The error is typically in the order of 2.5%.

### 3.8.3 Results

Figures 3.41 and 3.42 show the degree of polarization of the target material with its calculated error bars for all data runs taken during June and July of 2003 respectively. The big difference in degree of polarization of July runs versus June is due to the new doping radical used for the target material. Table 3.5 indicates the calculated relaxation times for each of the 12 target runs. The distinction in relaxation time for different runs is due to the unequal temperatures of each period.

Run	$\tau$ (h)	$\Delta\tau$ (h)
June 19 → June 21	172	28
June 21 → June 24	121	14
June 24 → June 26	188	32
June 26 → June 28	223	48
June 28 → June 30	213	44
July 14 → July 15	138	46
July 15 → July 17	219	41
July 17 → July 19	233	41
July 19 → July 21	228	40
July 21 → July 23	229	41
July 23 → July 25	234	42
July 25 → July 29	232	20

**Table 3.5:** Relaxation times of the polarized runs.

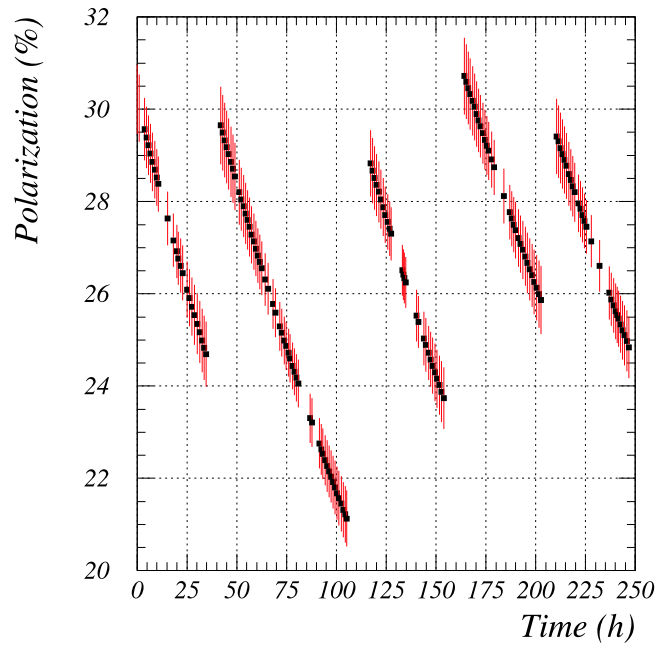


**Figure 3.41:** Calculated target degree of polarization of the 2003 GDH experiment during the June's run.

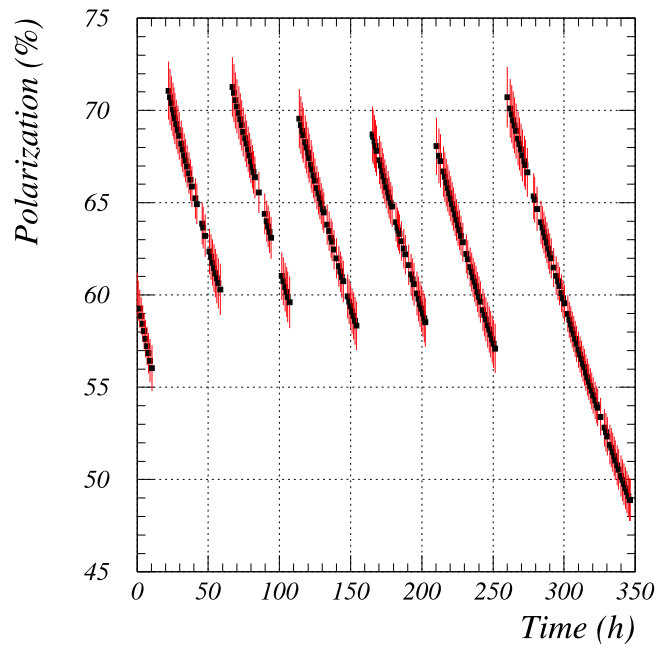


**Figure 3.42:** Calculated target degree of polarization of the 2003 GDH experiment during the July's run.



---

---

# Chapter 4

## Analysis

---

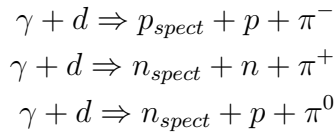
---

*Do not believe in anything simply because you have heard it.  
Do not believe in anything simply because it is spoken and rumored  
by many. Do not believe in anything simply because it is found  
written in your religious books. Do not believe in anything merely  
on the authority of your teachers and elders. Do not believe in  
traditions because they have been handed down for many generations.  
But after observation and analysis,  
when you find that anything agrees with reason  
and is conducive to the good and benefit of one and all,  
then accept it and live up to it.*

The Buddha

### 4.1 Introduction

This chapter will explain in a schematic way the analysis performed to experimentally evaluate both the unpolarized and the helicity dependent differential cross section of three single pion production channels on the deuteron:



The differential cross section ( $d\sigma/d\Omega$ ) measures the likelihood of a particular interaction between particles from a beam and a given target material. This parameter is expressed in units of area and solid angle; in this work it will be given in  $\mu\text{barn/sr}$  (1 barn =  $10^{-24}$   $\text{cm}^2$ ).

In case of single pion production, it can be defined in general as:

$$\frac{d\sigma}{d\Omega}(E_\gamma, \theta) = \frac{N_{emitted}(E_\gamma, \theta)}{N_\gamma N_T} \frac{1}{\Delta\Omega} \quad (4.1)$$

where:

- $N_{emitted}$  is the the number of particles emitted for a given interval in the photon energy  $E_\gamma$  and in the polar emission angle  $\theta$ ;
- $N_\gamma$  is the number of photons with energy  $E_\gamma$  hitting the target;
- $N_T$  is the number of target nuclei per unit area;
- $\Delta\Omega$  is the detection solid angle centered around  $\theta$ ;
- $\theta$  is the polar emission angle of the photoproduced pion.

Since the detectors are never ideal they have a detection efficiency  $\varepsilon$ , given by:

$$\varepsilon = \frac{N_{detected}}{N_{emitted}} \quad (4.2)$$

where  $N_{detected}$  is the number of events detected (or identified) by the experimental setup.

In the study of the data collected using a longitudinally polarized target and a circularly polarized photon beam, an helicity dependent differential cross section can be defined as:

$$\left(\frac{d\sigma}{d\Omega}\right)_{helicity} = \left(\frac{d\sigma}{d\Omega}\right)_{parallel} - \left(\frac{d\sigma}{d\Omega}\right)_{antiparallel} \quad (4.3)$$

where the subindexes *parallel* and *antiparallel* correspond to the relative orientation of the photon helicity and of the target polarization.

The data that will be presented in this thesis were obtained in Mainz during 1998 in the framework of the GDH experiment, in which were carried out the first doubly polarized photoproduction experiments on the proton and the deuteron in order to perform an experimental check of the fundamental Gerasimov-Drell-Hearn sum rule, and to get a deeper insight into the properties of baryon resonances.

The polarized tagged photon beam was produced via bremsstrahlung of longitudinally polarized electrons produced by the MAMI accelerator (section 3.2.1). In order to maximize the degree of photon polarization, two different electron energies ( $E_e = 525$  MeV and  $E_e = 855$  MeV) were used. The Bremsstrahlung photons were tagged using the Glasgow-Mainz spectrometer with an energy resolution of about 2 MeV (section 3.2.2). The experimental events analyzed in this work are coming only from the main hadron detector DAPHNE (section 3.3.1).

The following sections will explain the main features of the data analysis, which are common for all the studied channels. Many of these features are also common for all the different partial-channel analysis performed using the present data. For this reason, additional information on the different analysis techniques can also be found in previous works ([Hei00], [Rov02], [Pre01], [Hol01], [Lang04], [Lan04], [Ros05] and [Jah05]).

A detailed illustration of the particular algorithms applied for the identification of the events coming from the above mentioned  $\pi$ -production channels will be given in 4.3 and following sections.

The photon flux  $N_\gamma$  calculation has already been explained in section 3.2.3. The number of target nuclei per unit volume  $N_T$  is different for each of the two target materials employed in the present experiment. In section 4.2 the relevant geometrical and physical parameters of both targets are given. The detection efficiency  $\varepsilon$  was calculated using a simulation, based on the GEANT code. The most relevant features of this algorithm will be outlined in section 4.12.

## 4.2 Target Parameters

Target	Hydrogen	Deuterium 1997	Deuterium 2003	Butanol	DButanol
$\Delta x_{total}$ (cm)	19.6	19.6	10	1.88	1.88
$\Delta x$ (cm)	15	15	6	1.88	1.88
$\rho$ (g/cm <sup>3</sup> )	0.0708	0.162	0.162	0.94	1.109
$A$ (g/mol)	1.00794	1.99911	1.99911	1.00794	1.99911
$F_f$	1	1	1	0.63	0.63
$F_d$	1	1	1	10.135	0.238
$N_T \cdot 10^{22}$ cm <sup>-2</sup>	63.45	73.20	22.28	8.99	9.42

**Table 4.1:** Target physical parameters.

The number of target nuclei per unit volume can be written as:

$$N_T = \frac{N_A}{A} \rho \Delta x \quad (4.4)$$

where  $N_A=6.022 \cdot 10^{23}$  mol<sup>-1</sup> is the Avogadro number,  $A$  the mass number,  $\rho$  the density and  $\Delta x$  the length of the target.

In the case of the butanol ( $C_4H_9OH$ ) and the deuterated butanol ( $C_4D_9OD$ ) targets, only the numbers of polarized hydrogen and deuteron atoms have to be evaluated respectively since the contributions from unpolarized nuclei vanishes in the difference (Eq. 4.17.)

In the evaluation of  $N_T$  for the deuterated butanol target the effective atomic mass  $A_{eff}$  value has to be taken into account together with the density of the target material  $\rho$  and two additional parameters: i) the filling factor  $F_f$ , which is the percentage of the target volume occupied by the target beads, and ii) the dilution factor  $F_d$ , which is the fraction of the polarizable nucleons inside the target material. In this case, the amount of target nuclei per unit volume can then be written as:

$$N_T = \frac{N_A}{A} \rho \Delta x F_f F_d \quad (4.5)$$

Table 4.1 shows the numerical values of these parameters for the different targets. In this table,  $\Delta x_{total}$  represents the physical length of the target while  $\Delta x$  is the “virtual” target thickness used in the offline analysis code to define an allowed production vertex region for the good candidate events. This last parameter will be discussed in section 4.4.3.

### 4.3 Number of Selected Events

The analysis performed to calculate the number of detected events  $N_{detected}$  varies from one channel to another, but the general ideas are common:

1. Data reduction. For each event, the raw electronic signals recorded from the different detector parts (ADC, TDC, ...) are converted into physical parameters related to the detected particles as emission angles or deposited energies.
2. Geometrical conditions are applied to the particle trajectories to select production vertex coordinates compatible with the physical target region, and to reject events that entered inside some particular detector regions that could induce problems to the correct event identification.
3. All charged particles emitted in each event ( $p, \pi^\pm, e^\pm$ ) are identified using different methods according to the different hit detector zones.
4. Selection of a particular reaction channel. According to the number and nature of the identified charged particles, a particular reaction channel is chosen. Additional conditions can be applied to suppress possible channel misidentification. In the present analysis, for instance, only events induced by photons having an energy below 500 MeV will be considered in order to avoid any significant contribution from the double pion photoproduction processes.
5. Random events subtraction. Events due to accidental hits inside the tagger, i.e events not having a proper electron-photon time correlation, are taken into account and subtracted from the total number of selected events.



6. Evaluation of correction factors and efficiencies. The number of selected events has to be corrected for the known hardware detector inefficiencies and for the fraction of the events lost in the software selection procedure. These parameters are derived from the simulation and from experimental evaluations.
7. Evaluation of the differential cross section. Once the number of good candidate events has been selected and the contribution of accidental events has been subtracted, the differential cross section can be evaluated (Eq. 4.2) taking into account the detector efficiencies. If needed, the unwanted contributions from other partial channels have to be determined and subtracted.

In the case of the polarized experiments, the degrees of polarization of the target ( $P_T$ ) and of the photon beam ( $P_\gamma$ ) have also to be taken into account. The evaluation of the degree of target polarization for the 2003 GDH experiment is explained in detail in section 3.8. A similar analysis was performed for the 1998 data. The degree of photon polarization  $P_\gamma$  is obtained using a polarimeter based on the Møller effect, as shown in section 3.2.4.

In the next sections, all the above mentioned points will be discussed in detail.

## 4.4 General Geometrical Conditions

This section will describe the general geometrical conditions applied to all events in order to properly take into account the target and detector geometrical parameters.

### 4.4.1 Polar Angular Acceptance

The DAPHNE detector covers around 94% of  $4\pi$  and its acceptance in the polar angular region is:

$$21^\circ < \theta < 159^\circ \quad (4.6)$$

However, due to multiple Coulomb scattering effects, some charged particles entering close to the detector edges can leave the detector without depositing properly their energy and, therefore, may not be correctly identified. Because of this reason the software polar angular limits are defined as:

$$23^\circ < \theta < 158^\circ \quad (4.7)$$

### 4.4.2 Azimuthal Angular Acceptance

Each plastic scintillator layer is segmented into 16 sectors covering the full azimuthal angular region. Although each sector is shaped to fit to his neighbors, it is mechanically not possible to mount the sectors perfectly. As shown in Fig. 4.1 there are gaps between two neighboring sectors. Charged particles going through these gaps are not detected. Moreover, particles passing close to a sector border can deposit a fraction of its kinetic energy also in the neighboring sector due to multiple scattering effects.

In order to take both of these effects into account, a secure azimuth region is defined inside the offline code for each sector  $i$  using the wire chamber information (see Fig. 4.1). Only particles entering the detector within the region  $[\varphi_{min}^i, \varphi_{max}^i]$  are accepted. This approach allows to avoid most ambiguities in the track classification.

Since both the unpolarized and the helicity dependent cross sections are not depending on the azimuthal angle, a geometrical global factor can be applied inside the analysis procedure to take into account for the fraction of particles that are then lost. The corresponding azimuthal efficiency is evaluated using a simulation. For the 1998 data the correction factor was determined to be  $\varepsilon_\varphi = 1.18$ . For more details see [Isv93] and [Ped98a].

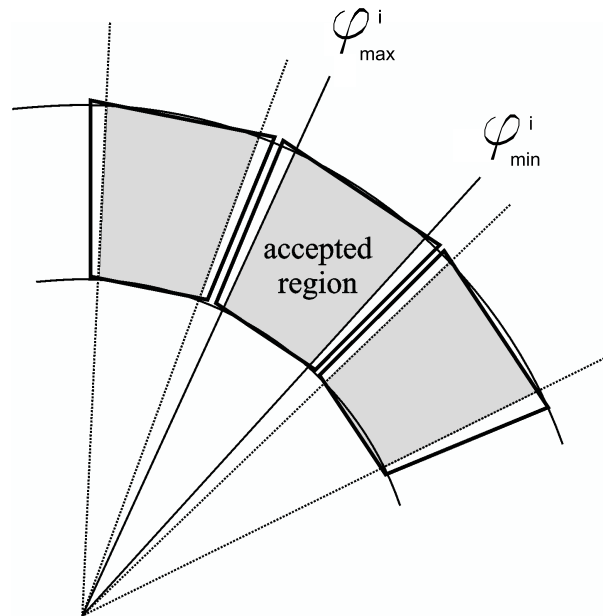


**Figure 4.1:** Gaps in the azimuthal angle.

### 4.4.3 Definition of the Target Geometry

Data taken with two different targets (polarized and unpolarized) are presented in this work. The charged particle track determination given by MWPCs allows a precise reconstruction of the position of the interaction vertex. By imposing some conditions on the position of this vertex, (at least) a relevant fraction of the unwanted contributions coming from the windows that are present along the beam line can be eliminated.

In the case of two charged particle tracks, the vertex is evaluated to be in the middle of the shortest segment connecting the two trajectories. The uncertainty related to this was determined, using cosmic rays, to be within 0.5 and 1.5 mm, depending on the the polar emission angle  $\vartheta$  [Isv93].

In the case of a single charged particle track, the vertex position is defined at that point of the track which has the smallest distance to the beam ( $Z$ ) axis. By taking into account the maximum beam dimensions on the  $XY$  plane (about 0.6 cm in our case) and the lowest detectable emission polar angle ( $\vartheta = 21^\circ$ ) it is possible to evaluate the largest error that can be made on the reconstructed  $z$ -vertex coordinate, it is about 15mm.

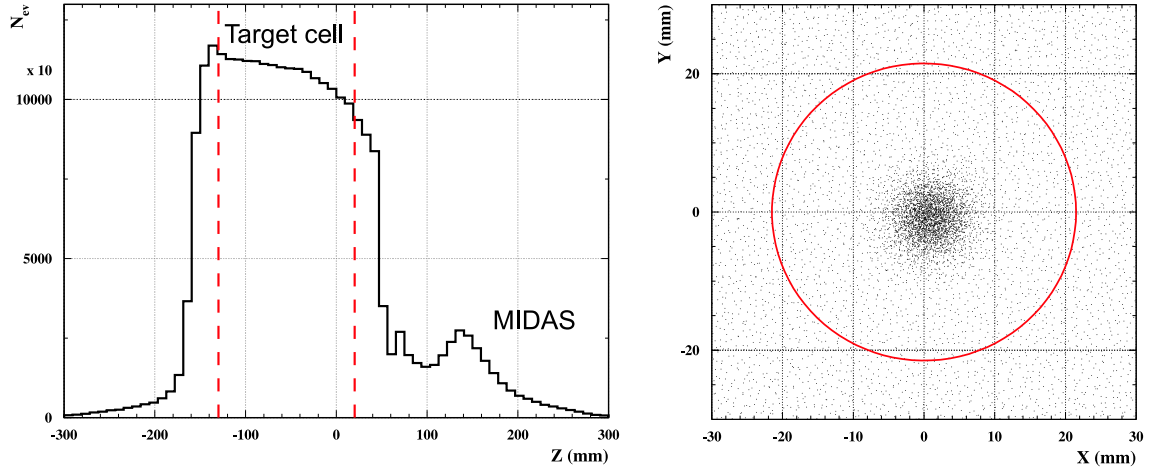


**Figure 4.2:** Interaction vertex distribution along the beam ( $Z$ ) axis and on the ( $XY$ ) plane perpendicular to it in the case of the the liquid deuterium target. Events originating from the entrance window of the forward detector MIDAS can be clearly observed.

Fig. 4.2 shows the interaction vertex distribution along the photon beam axis  $Z$  and in the  $XY$ -plane perpendicular to it obtained in the case of two charged particle tracks and with the unpolarized deuteron target. Events originating from the entrance window of the forward MIDAS detector can be clearly seen. In Fig. 4.3, the same distributions are shown for the polarized butanol target case.

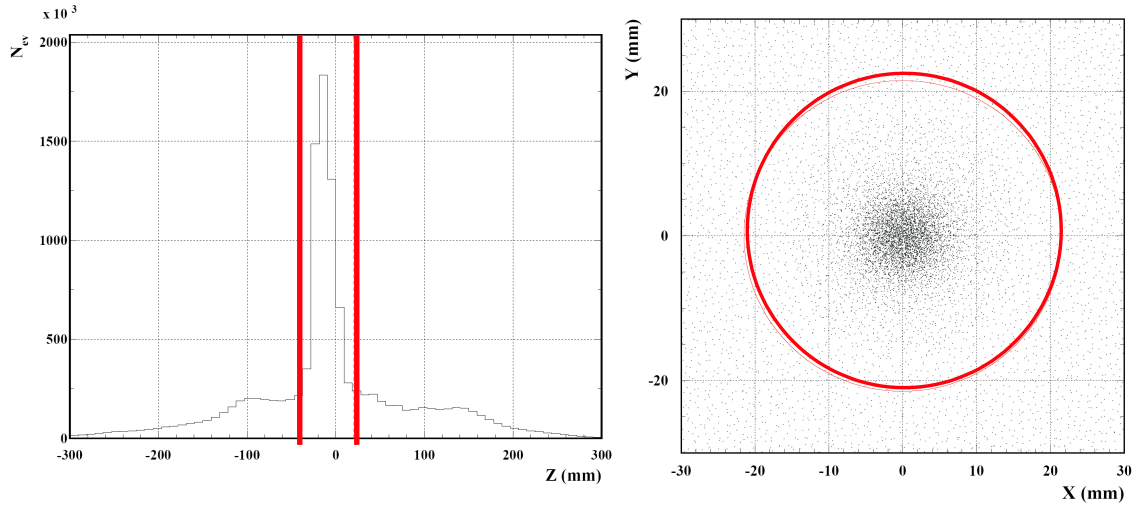


**Figure 4.3:** Event-vertex distribution in the beam axis  $Z$  and in the  $XY$ -plane for the polarized target. The complete target cell is included by the  $Z$ -axis cut.

Due to the low beam dispersion, the diameter of the  $XY$ -beam spot is much smaller than the 43 mm diameter of the physical targets. The circles drawn in the right part of Figs. 4.2 and 4.3 define the cuts applied in the  $XY$ -plane that rejects events originating from outside a cylinder along the  $Z$ -axis of radius  $r = \sqrt{x^2 + y^2} \leq 21.5$  mm.

On the other hand, two different conditions were applied along the  $Z$ -axis depending on the target type. Since the physical length of the unpolarized liquid target (19.6 cm, see table 4.1) is much longer than the largest error (15 mm) that can be made in the determination of the vertex coordinate along the  $z$ -axis, an allowed vertex region (delimited by the two dashed vertical lines in the left part of Fig. 4.2) can be defined within the target to safely cut all contributions coming from the target windows. In this way, no empty target subtraction is needed in the unpolarized data analysis.

On the contrary, the physical length of polarized target cell (18.8 mm, see table 4.2) is of the same order of magnitude as our vertex resolution and, therefore, a different philosophy has to be adopted. In this case, the limits of the allowed region (vertical lines in the left part of Fig. 4.3) are placed outside the physical region in order not to reject any good event. Then background events are also accepted. The contribution of these unwanted events, coming from unpolarized nuclei, will however cancel out in the evaluation of the helicity dependent difference cross sections (Eq. 4.3).

Table 4.2 summarizes the physical lengths of the different targets and the software limits on the  $Z$ -coordinate vertexes applied for each of them.

Target	Physical Z limits (mm)	Geometrical cut (mm)
Hydrogen	[ -153, +43 ]	[ -130, +20 ]
Deuterium (1997)	[ -153, +43 ]	[ -130, +20 ]
Deuterium (2003)	[ -153, -53 ]	[ -130, -70 ]
Butanol	[ -23.4, -4.6 ]	[ -40, +20 ]
DButanol	[ -23.4, -4.6 ]	[ -40, +20 ]

**Table 4.2:** Physical target and software limits for the different targets used in this experiment.

#### 4.4.4 Effective Target Length

There are two geometrical factors that reduce the effective target length, and therefore the number of detected events. On one hand the target volume is not point-like, but it has a finite thickness. On the other side the active elements of DAPHNE are finite cylinders not much longer than the target itself. The first wire chamber is only one third longer than the target cell. Because of these two reasons the detection probability for certain particle paths with the same polar angle  $\vartheta$  depends on the vertex position from which they originate.

To overcome this problem the active detecting element, which determines the extent of the effective solid angle subtended, is modeled with a control cylinder centered in the beam axis with a defined radius  $R = 40$  mm and length  $L = 212$  mm. Tracks that overshoot this cylinder are within the DAPHNE angular acceptance. If only one charged particle is detected its vertex is defined as the closest point of the reconstructed trajectory to the beam axis. In picture 4.4-A this problem is represented. The first track is inside the acceptance while the second one intersects the control cylinder at the edge and defines the maximum  $z_{max}^{eff}$  which is still perceived by the detector. The third track is outside DAPHNE acceptance.

A weight  $w(\vartheta)$  is applied to the yield of events to correct for the angular dependence on the target length  $L_{target}$ , and to normalize all events to the same target thickness. It can be written as:

$$w(\vartheta) = \frac{L_{target}}{L_{eff}} \quad (4.8)$$

where  $L_{eff} = z_{max}^{eff} - z_{min}$  for forward angles  $\vartheta \leq \pi/2$ , and  $L_{eff} = z_{max} - z_{min}^{eff}$  for backward angles  $\vartheta > \pi/2$ .

The error that enters due to the lack of information about the real reaction vertex for a single-track event cancels because of the symmetry of the target cell and the photon beam profile.

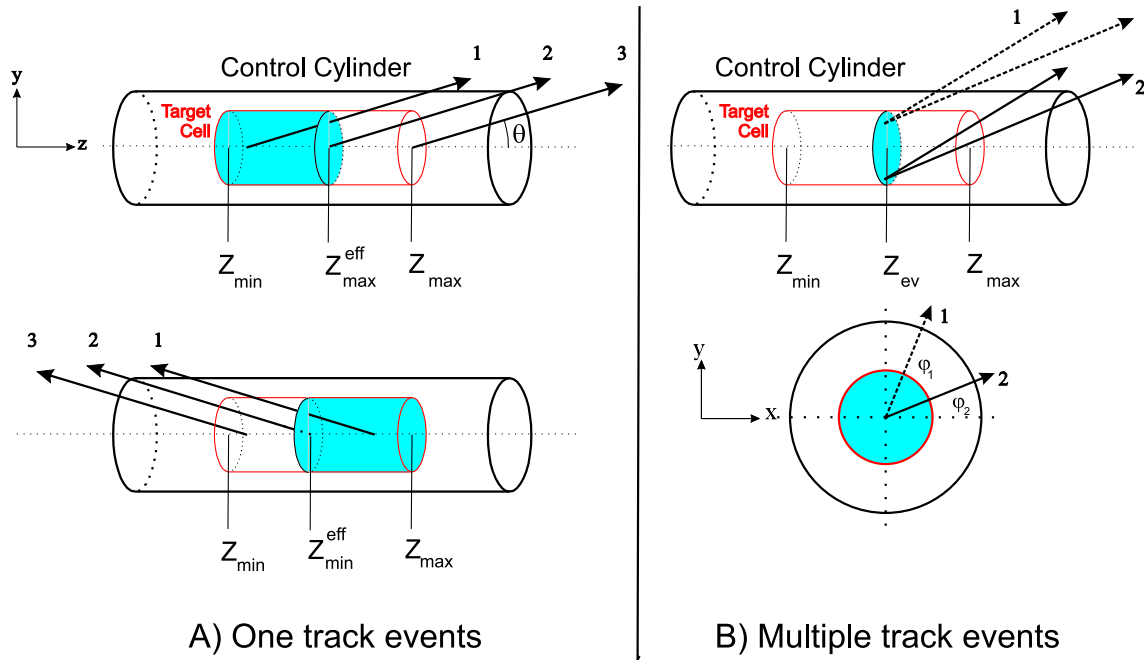


**Figure 4.4:** Effective target length correction.

The situation is more complicated for events with two or more tracks emitted from the target since effects of the azimuthal emission angles and off-axis events need to be taken into account, Fig. 4.4-B illustrates the problem. In this case the vertex is not defined along the beam axis, it can be placed at any point inside the target cell. dashed lines (1) represent the trajectories of two particles produced in a defined vertex in a plane perpendicular to the  $Z_{ev}$  position. Full lines (2) show the same event produced in a different point in this plane. As can be seen one of the particles from (2) is outside the control cylinder. In this case the correction is additionally depending on azimuthal angle,  $w(\vartheta, \varphi)$ , and it is also evaluated from a purely geometrical calculation that can be preformed exactly to give an effective target range for each track.

#### 4.4.5 Random Subtraction

Each detector trigger is placed in coincidence with the tagger to relate the event with the photon energy that induces the reaction. TDC-modules (Time to Digital Converters) register the relative time difference between tagger and detector events. Only events that appear in coincidence with the detection of an electron inside the tagger spectrometer within a time window of 160 ns wide are accepted.

Photo-induced events have a fixed time difference within the time resolution of the

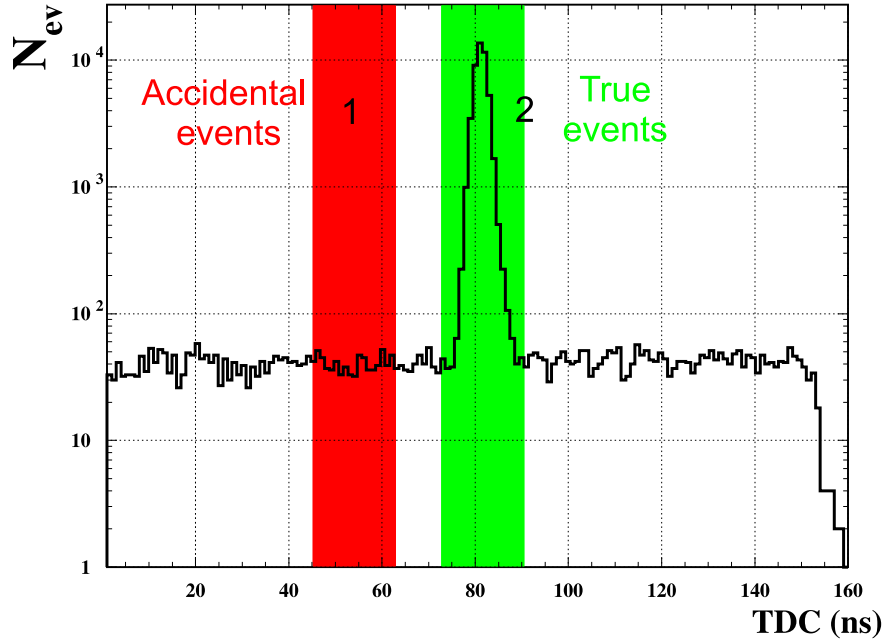


**Figure 4.5:** TDC spectrum. Zone 1, in red contains only the accidental events. The peak inside zone 2, in green, comes from photo-induced reactions that have a stable time-relation between the tagger and the detector.

hadronic trigger, since the electrons and photons have roughly the same velocity. For this reason, a prominent peak in the time difference can be clearly seen in Fig. 4.5. Two regions having the same time width are defined in Fig. 4.5 to correct for accidental time coincidences. Region 1 (from 45 to 63 ns) contains only accidental background while region 2 (from 75 to 93 ns) includes accidental and true events. A simple subtraction of events in region 1 from those of Region 2 corrects for the accidental events.

This second contribution is coming from two different types of events:

- A single electron that produces a Bremsstrahlung photon enters the tagger and by multiple scattering or Møller interaction hits more than one focal plane detector. This effect can be easily recognized and corrected because all the hit tagger channels are adjacent. Only the hit tagger channel corresponding to the lowest photon energy is taken, since, for geometrical reasons, the electrons are preferably scattered into tagger channels that belong to higher electron energies.

- One or more accidental electrons and possibly a "good" one enter the tagger within the time interval. These are true and random events, and are distinguished by the subtraction of the two regions. In the first place we do not reject any of these hits, we just treat them like independent measurements.

## 4.5 Energy Binning

A energy calibration of the tagger channels is needed to present the data as function of the photon energy. By knowing the tagger magnetic field and the position of the covered detectors in the focal plane it is possible to calculate the electron energy that is covered by each channel (Eq. 3.1). Unfortunately the energy width is not constant and it has to be calculated for each detector. In this work the "natural" tagger energy binning has been chosen. The results will be presented in bins of some tagger channels. The theoretical calculations and some old experimental data compared with the present work are given in slightly different energy ranges, therefore a linear interpolation between two bins is done.

## 4.6 Identification Methods for Charged Particles

Three different approaches are used to identify the photoemitted charged particles: the standard  $\Delta E/E$  technique, the range fit method and the geometrical range algorithm. They are explained in detail in the following sections.

### 4.6.1 The $\Delta E/E$ -Method

In the standard  $\Delta E/E$ -technique a thin detector A is placed near the target and in front of a thicker detector B, where all particles are absorbed. These particles lose a certain amount of energy,  $\Delta E$ , inside detector A while the remaining part ( $E_B$ ) of the particle kinetic energy ( $E = \Delta E + E_B$ ) will be deposited inside B.

In the non relativistic regime, according to the well known Bethe-Bloch formula the relative energy deposition inside A and B at a given energy are particle dependent. In the  $\Delta E-E$  plot each charged particle will concentrate inside a specific band depending on its mass.

This method is employed in the DAPHNE detector using the plastic scintillators of the thin layer A and the thick layer B. It is also possible to use it for the slowest charged particles that are stopped inside the A layer. In this case the  $\Delta E$  information is provided by the MWPCs.

The wire chambers are in fact working in the proportional regime, hence the charge collected by the strips is proportional to the primary energy loss of the particle. Fig. 4.6 shows the correlation between the energy deposited inside the MPWCS,  $E_{MPWC}$ , (corrected for the distance traveled inside the material) and the energy deposited inside the A layer,  $E_A$ . Due to the low energy resolution of the MWPC only protons can be separated in practice from the region containing the overlapping pion and electron bands, as shown by the diagonal line of Fig. 4.6. This cut depends on the material between the



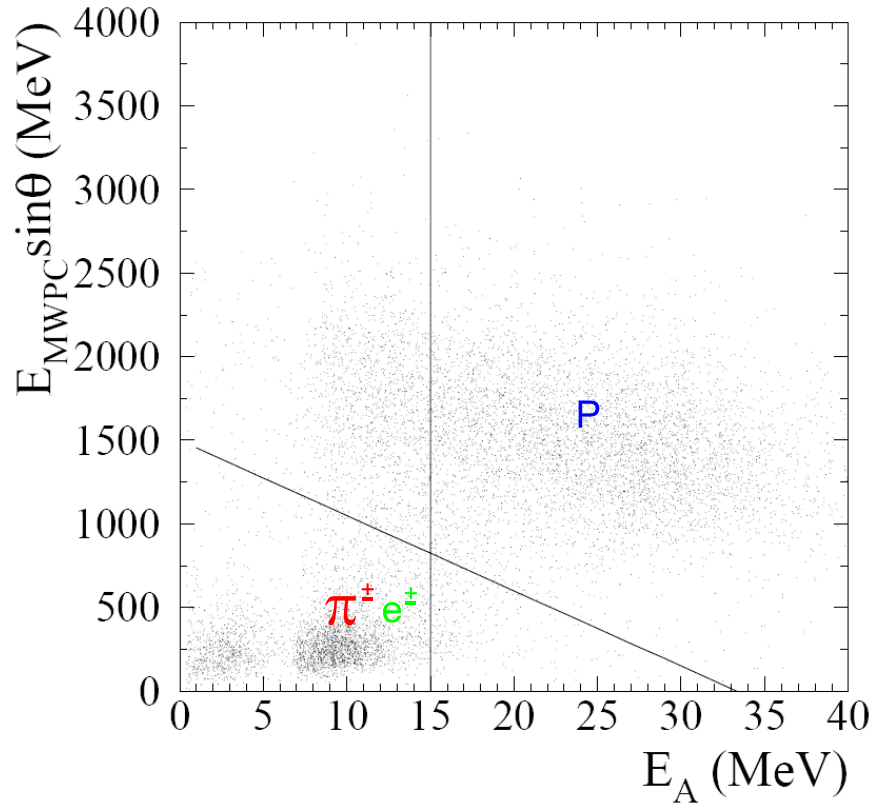


**Figure 4.6:** A typical  $\Delta E/E$ -plot for particles that stop in layer A. Plotted is the energy deposit in the scintillator of the layer A,  $E_A$ , versus the energy information of the MPWC ( $E_{MPWC}$ ) corrected by the angular dependence.

production vertex and the MPWCs and it is different for each target.

Moreover, since all scintillators inside the A layer are read by only one photomultiplier, the detection threshold for charged particles stopped inside this layer depends on the  $Z$ -coordinate of the particle impact point. To overcome this problem only particles with energy deposits above 15 MeV are considered for the proton identification (vertical line of Fig. 4.6). The cuts used to identify protons are:

$$E_A > 15 \text{ MeV} \quad (4.9)$$

$$E_{MWPC} \cdot \sin\vartheta > a_1 E_A + b_1 \text{ MeV} \quad (4.10)$$

with

$$a_1 = -45, \quad b_1 = 1500 \quad \text{for deuterium target}, \quad (4.11)$$

$$a_1 = -40, \quad b_1 = 1020 \quad \text{for deuterated butanol target}. \quad (4.12)$$

### 4.6.2 The Range Fit Method

The range-fit method is an extension of the standard  $\Delta E/E$ -method outlined above when more than 2 scintillators are used for the particle identification. Since the geometry and the physical properties of all detector materials (scintillators, absorbers, ...) are well known, the expected energy deposited by a charged particle ( $\Delta E_{layer}^{theo}$ ) can be evaluated for each layer when its initial kinetic energy,  $E_0$ , is known. From the measurement of the experimentally deposited energy ( $\Delta E_{layer}^{exp}$ ), the  $E_0$  value can be obtained by minimizing the quantity:

$$\chi^2(E_0) = \frac{1}{N-1} \sum_{i=1}^N \frac{|\Delta E_{layer}^{theo}(E_0) - \Delta E_{layer}^{exp}|^2}{\sigma_i^2} \quad (4.13)$$

by a least-square fit having  $E_0$  as a free parameter. In this equation  $N$  represents the layer where the particle stopped (or the last hit layer) and  $\sigma_i$  is the energy resolution of the  $i$ -th layer. This procedure is repeated under the assumption of different particle types in the Bethe-Bloch function and the lowest  $\chi^2$  found correspond to the best fit.

Using this method protons and charged pions are identified and in addition their kinetic energies are obtained. This technique has been developed and successfully tested for the DAPHNE detector over the last 10 years ([Mur93] and [Bra94]). The identification efficiency is angle and momentum dependent, and it is in general between 70-90%. The relative resolution on the evaluated kinetic energies is about 5% and the fraction of events that are systematically misidentified using this is evaluated to be 2% at maximum.

Fig. 4.7 displays a typical  $\Delta E/E$ -plot for particles stopped inside the B layer. Three well separated bands corresponding to protons, pions, and electrons are seen. The protons

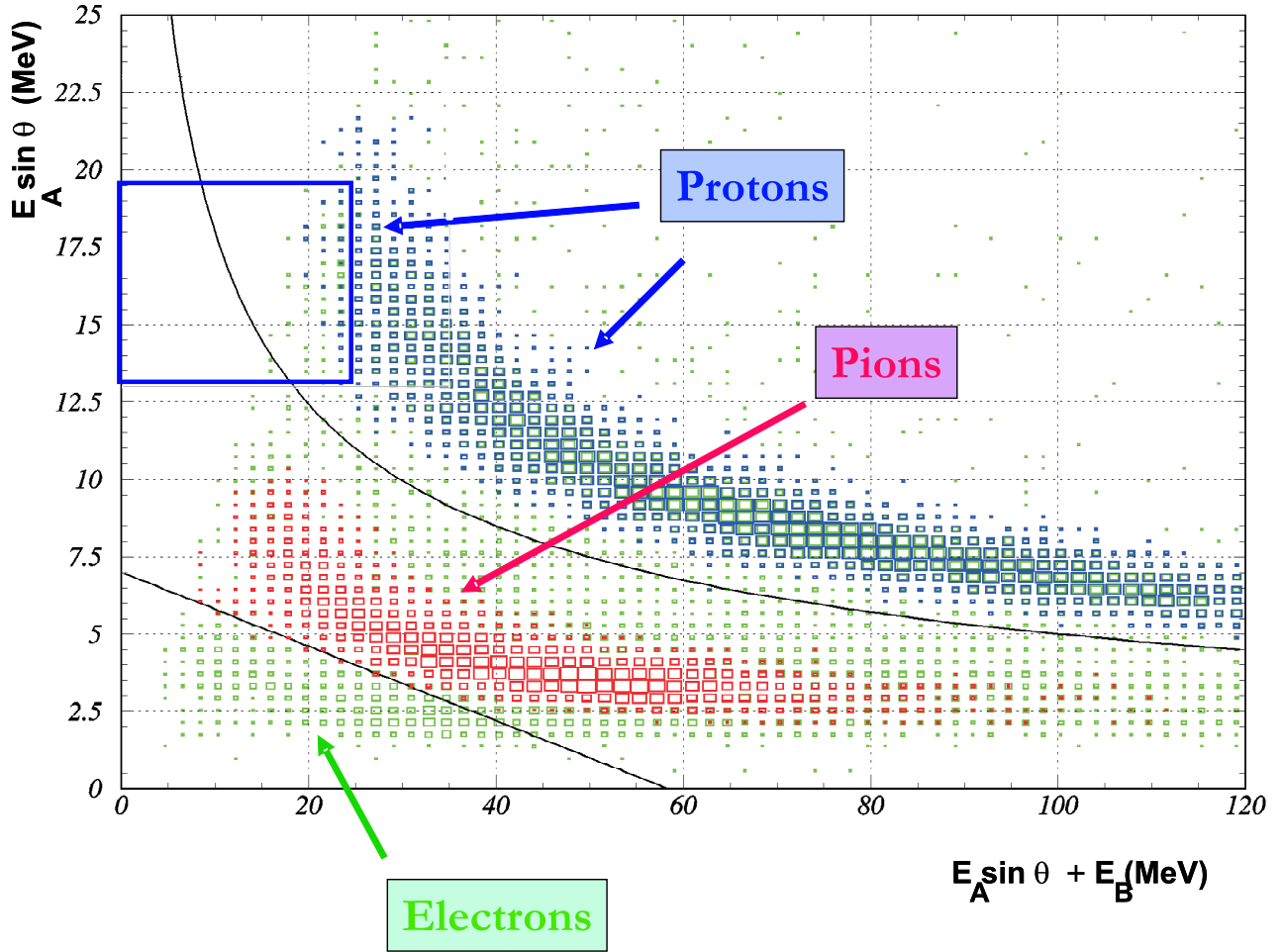


**Figure 4.7:**  $\Delta E/E$ -plot for particles stopped inside the B layer. Three bands corresponding to protons, pions and electrons can be clearly seen. Protons and pions identified with the range fit method are plotted in blue and pink respectively. The diagonal line shows the cut used to preventively remove the largest part of the electron events. The blue box corresponds to protons depositing a small amount of energy inside the B layer

and pions identified using the the range-fit algorithm are superimposed in pink and blue, respectively. The very good agreement between these two technics is a proof of the validity of the range-fit method. The blue box located in the upper left part of Fig. 4.7 corresponds to protons that deposited only a small amount of energy inside the B-layer. In this case, multiple scattering effects play the dominant role for the energy sharing between the A and B layers, hence the range-fit method can not be reliably applied but the  $\Delta E - E$  method can be used to identify them as protons. The limits of this “proton corner” are:

$$12 < E_A \sin\theta < 19 \quad (4.14)$$

$$E_A \sin\theta + E_B < 25 \quad (4.15)$$

From Fig. 4.7 it can also be clearly seen that most of the electron contribution that is located in the lower left part of the plot can also be preventively removed by rejecting events with:

$$E_A \sin\theta < \frac{28}{\sqrt{E_A \sin\theta + E_B}} - 1.5 \quad (4.16)$$

Since at least two energy loss samples along the charged track are needed, the domain of applicability of this method is restricted to particles that penetrate beyond the first scintillator layer. Moreover this method is also not well suited for the identification of the charged particles that have sufficient energy to escape the detector since they start to enter in the relativistic regime, where the Bethe-Bloch formula predicts a very similar behavior for the different particle types. In this case, the particle identification was performed by using the geometrical range method that is described below.

### 4.6.3 The Geometrical Range Method

Charged particles stopped inside the external layers (C, D, E and F) can be identified (without the evaluation of their kinetic energy) by comparing the energy lost in the B-layer (the one with the highest energy resolution) to the geometrical path of the particle through the detector, expressed in equivalent scintillator thicknesses (e.s.t.).

This algorithm is called geometrical range method and it is based on the fact that, at the MAMI-B photon energies, photoproduced protons are still not fully relativistic. This method is shown in Fig. 4.8 for particles stopping inside C, D, E and F layers together with the cuts used to separate pions protons and electrons. As it can be clearly seen, most of the particles arriving to the last layer (F) are pions since they are the most energetic photoreaction products. By contrast, the majority of the protons are stopped in the layer B.

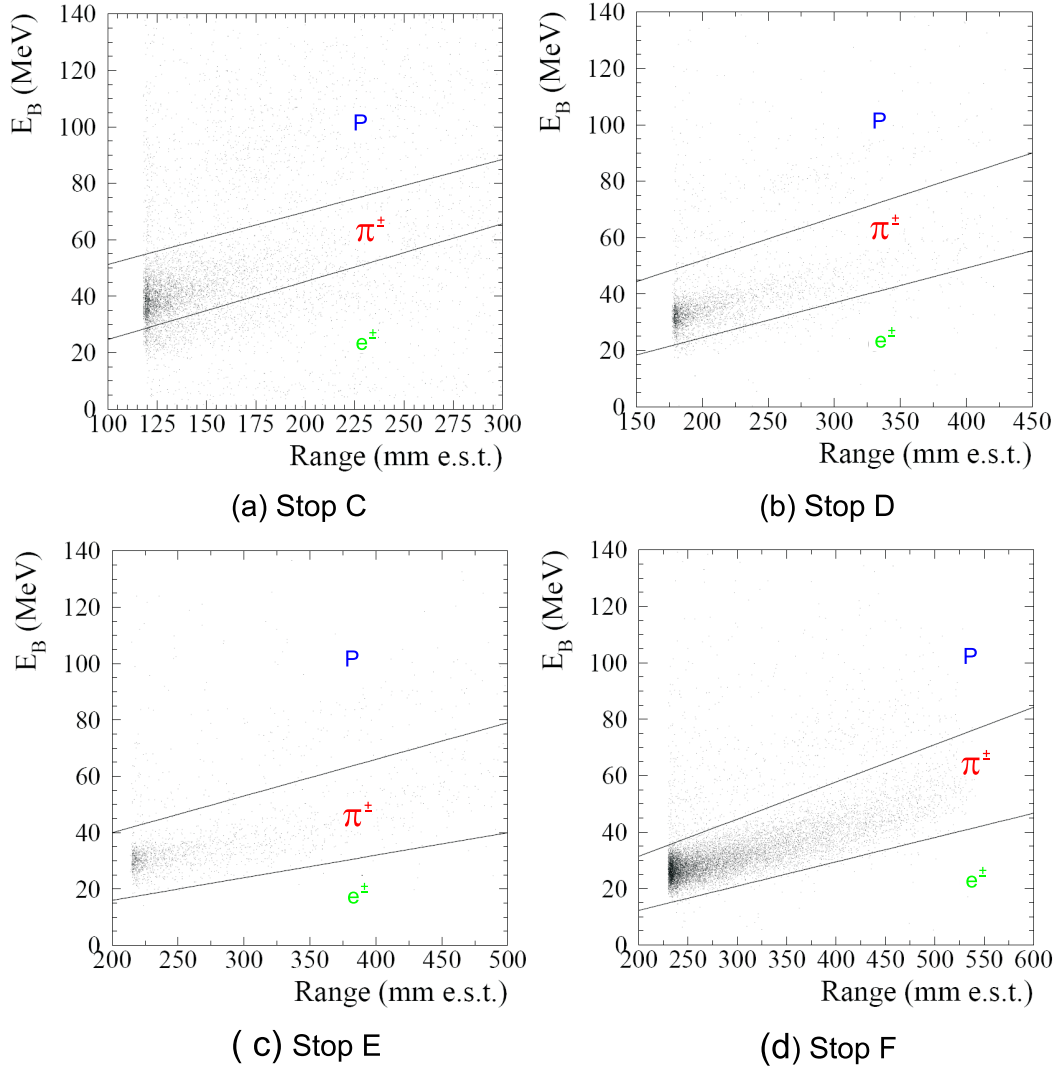


**Figure 4.8:** Example of the geometrical range method. The energy released inside the B layer by particles going through all layers is shown as a function of geometrical path (in equivalent scintillator thickness, e.s.t.). The two diagonal lines delimit the regions used for the particle identification.

## 4.7 Partial Channel Analysis

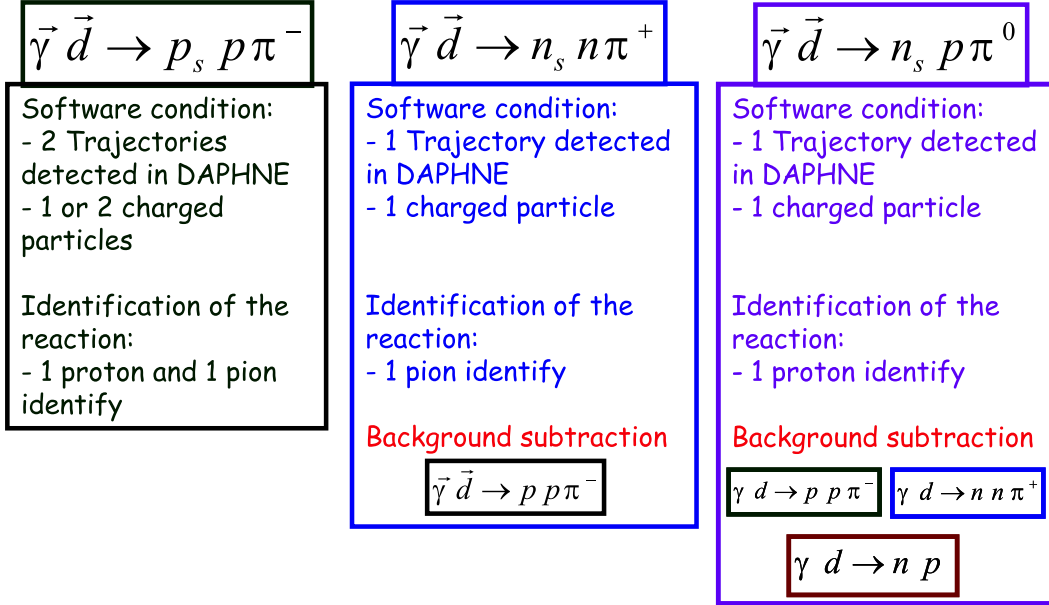


**Figure 4.9:** Schematic summary of the analysis methods used for the analysis of the three considered reaction channels. The kinematics of the  $\pi^-$  channel can be completely determined on an event-by-event basis and this allows the test of the nucleon spectator hypothesis. Additionally it is used for the background subtraction for the  $\pi^+$  reaction identification. In the  $\pi^0$  case, channel only the proton is detected and different sources of background have to be taken into account.

The data used for the analysis of this reaction were taken in 1998 in Mainz within the framework of the GDH experiment. Two different targets were employed: an unpolarized liquid deuterium and a polarized deuterated butanol target, see section 4.4.3. In Fig. 4.9 a schematic view of the different analysis procedures used for the different partial channel analysis is shown. In the following sections the details of each reaction channel will be outlined.

The data taken with the unpolarized deuterium target and beam were both used for calibration purposes and efficiency studies, and for the reproduction of the known unpolarized differential cross sections in order to test the analysis procedures. Once these analysis have been well established, they were applied with minor modifications to obtain information about the polarized reactions.

## 4.8 Analysis of the $\gamma + d \Rightarrow p_{spect} + p + \pi^-$ Reaction

For the identification of this channel the coincident detection of both the proton  $p$  and the negative pion  $\pi^-$  was required. The remaining proton  $p_{spect}$  was assumed to be a reaction spectator, thus remaining inside the target. Using the measured target parameters and the momentum and energy conservation laws, the emission parameters of this undetected proton can be reconstructed in order to check the validity of this assumption, see Fig. 4.10.

Candidate events for this reaction were selected by requiring the presence of two reconstructed trajectories on the MWPC and the presence of at least one charged particle in the allowed azimuthal angular region of the DAPHNE detector.

Then the geometrical cuts described in the previous sections were applied and an additional condition on the beam photon energies, required to be below 500 MeV, was used. This last condition eliminates the contribution of the double pion photoproduction channels that are difficult to separate from the single pion channels and that give a negligible contribution inside the selected energy range.

After these preliminary steps, the identification of the detected charged particles is performed. As discussed in the previous sections, different algorithms have to be used according to the layers where the particles get stopped:

- Stop-A particles: in this case only protons are identified using a  $\Delta E - E$ -plot where the  $\Delta E$  and  $E$  parameters are energy deposited inside the MPWCs and inside A layer, respectively (see Fig. 4.6). After their identification, the energy of stop-A proton was derived from the range-energy relations
- Particles stopped inside layers B, C, D, E: protons and charged pions are identified, with the determination of their kinetic energies, by using the range-fit method. The identification of the Stop-B protons located inside the so-called "proton corner", is obtained from the  $\Delta E - E$ -plot of Fig. 4.7.
- Particles going through all layers (stop-F particles): protons and charged pions are identified, without the determination of their kinetic energies, by using the geometrical range method.

The presence of one identified proton and one pion are required for the identification of this channel. Since all proton emission parameters and at least the pion angular emission parameters are evaluated by the analysis program, the event kinematic can be fully reconstructed on an event-by-event basis using energy and momentum conservation laws, and the emission parameters of the undetected proton can thus be evaluated.

Fig. 4.10 shows the reconstructed momentum distribution of the undetected proton. As it can be clearly seen, the shape of the experimental momentum distribution coincides

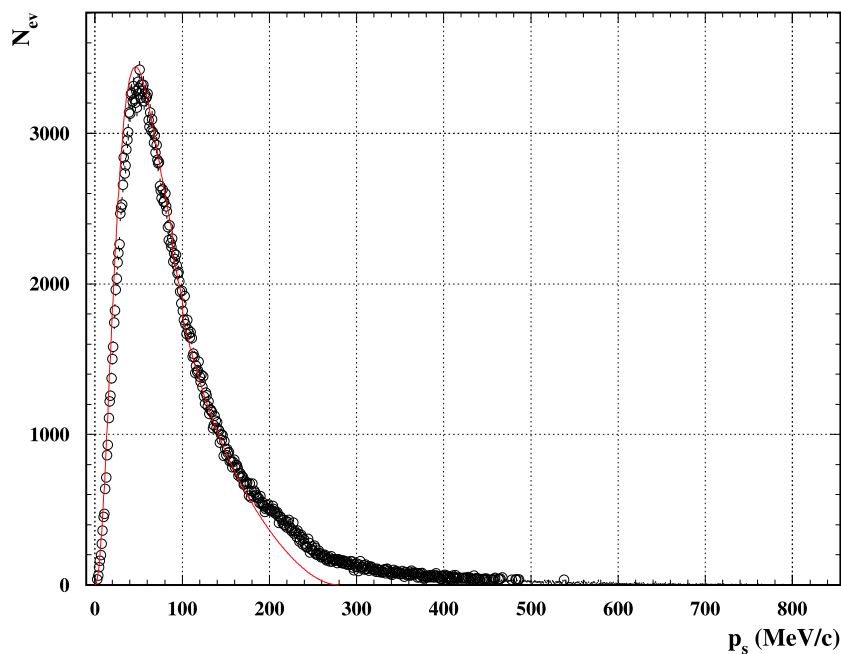


**Figure 4.10:** Evaluated momentum distribution of the undetected proton from the  $\gamma d \rightarrow pp\pi^-$  reaction. The dots are the reconstructed values from the experimental data, while the red line is the theoretical Fermi momentum distribution.

with what is expected purely on the basis of a Fermi motion. This proves the spectator nucleon assumption that was made before, showing that the single pion photoproduction process on the deuteron takes mainly place on a quasi-free nucleon. There is just a small fraction of events at momenta higher than 200 MeV that do not follow this model.

In order to get the differential cross section, the number of identified events  $N_{ev}$  for a given interval in the photon energy and in the  $\pi^-$  polar emission angle (in the lab system) is corrected by:

- i) the effective target weight  $w(\vartheta, \varphi)$  (Eq. 4.8),
- ii) the MWPC efficiency (91.8% for this channel),
- iii) the correction term due to the missed events because of the holes in azimuthal acceptance ( $\varepsilon_\varphi=1.18$ ),
- iv) the efficiency of the different particle identification algorithms that were used. This parameter was evaluated as outlined in section 4.12.

Finally the corrected number of events is multiplied by the number of target nuclei per unit volume given in Table 4.1 and divided by the integrated photon flux values.

The only possible source of background in this channel is coming from the  $\pi^0$  pro-



duction channel followed by the  $\pi^0 \rightarrow \gamma e^+ e^-$  Dalitz decay or by the  $\pi^0 \rightarrow \gamma\gamma \rightarrow \gamma e^+ e^-$  conversion before the MWPCs. The results from simulation have shown that this background is much smaller than 1% of the measured particle yield and was therefore neglected in the present analysis.

## 4.9 Analysis of the $\gamma + d \Rightarrow n_{spect} + n + \pi^+$ Reaction

Events with a single charged track recognized as a pion were selected in order to identify the quasi-free  $n\pi^+$  production. Due to the low DAPHNE detection efficiency, the additional neutron information was not used in this analysis.

The same geometrical and photon energy conditions as in the previous channel were set to define the detector acceptance. The charged pion identification and the differential cross section evaluations were performed using the previously described algorithms with a MWPCs efficiency of 98%.

In this case there is a significant source of background given by the  $\gamma + d \Rightarrow p_{spect} + p + \pi^-$  when only the  $\pi^-$  is detected within the DAPHNE acceptance, since the pion charge can not be determined by our apparatus.

The major part of this background was removed by restricting the cross section evaluation, of reach photon energy bin, to the same angular range for which there is the coincident  $p\pi^-$  detection. Under this condition, the remaining part of the background is given by the fraction of  $p\pi^-$  events in which the proton does not reach the DAPHNE detector due to hadronic interactions inside the target materials. This contamination was evaluated using the previously obtained  $p\pi^-$  differential cross section  $\left(\frac{d\sigma}{d\Omega_{p\pi^-}}\right)$  and the simulated proton hadronic interaction probability ( $\varepsilon_{background}$ ). The obtained differential cross section for the  $n\pi^+$  channel can then be written as:

$$\frac{d\sigma}{d\Omega_{n\pi^+}} = \frac{d\sigma}{d\Omega_{charged\ pion}} - \frac{d\sigma}{d\Omega_{p\pi^-}} * \varepsilon_{background} \quad (4.17)$$

where  $\left(\frac{d\sigma}{d\Omega_{charged\ pion}}\right)$  is the differential cross section obtained with the above mentioned condition, and  $\varepsilon_{background}$  is the probability of identifying a  $p\pi^-$  event as an  $n\pi^+$  event that was obtained with the GEANT simulation:

$$\varepsilon_{background} = \frac{N_{total}^{created\ as\ p\pi^-}}{N_{identified\ as\ n\pi^+}^{created\ as\ p\pi^-}} \quad (4.18)$$

The  $\varepsilon_{background}$  parameter was found to be at maximum around 5% of the measured charged pion yield.

## 4.10 Analysis of the $\gamma + d \Rightarrow n_{spect} + p + \pi^0$ Reaction

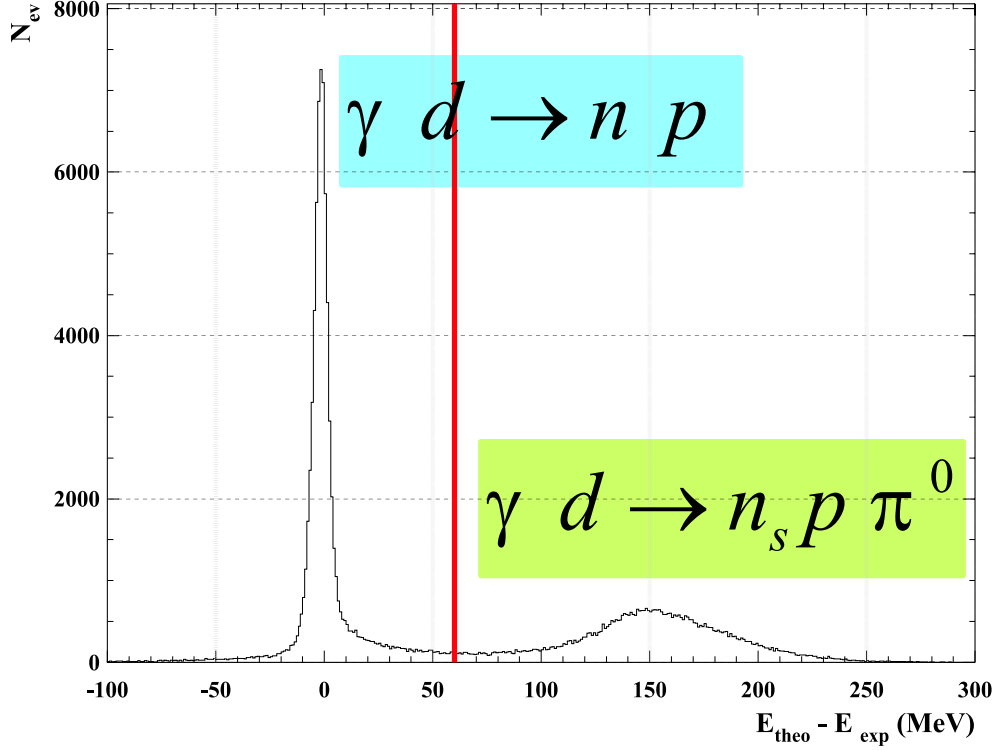


**Figure 4.11:** Missing energy ( $E_{\text{miss}}$ ) spectrum for the reaction  $\vec{\gamma}d \rightarrow pn$ . Events located on the right hand side of the vertical line correspond to the quasi-free  $p\pi^0$  events.

The analysis of this reaction is similar to the previous  $\gamma + d \Rightarrow n_{spect} + n + \pi^+$  analysis. In this case the single charged particle detected is required to be identified as a proton. The different normalization factors needed to obtain the differential cross section are the same as in the previous channels; only the MWPC efficiency value (now 100%) needs to be modified.

Two main different sources of background have in this case to be taken into account:

1. events coming from the reaction

$$\gamma + d \Rightarrow p_{spect} + p + \pi^- \quad (4.19)$$

when only the proton was emitted inside the DAPHNE acceptance

2. events coming from the deuteron photodisintegration process:

$$\gamma + d \Rightarrow n + p \quad (4.20)$$

As in the  $n\pi^+$  case, the first source of background was evaluated using the measured  $p\pi^-$  yield and simulated fraction of  $p\pi^-$  events in which the  $\pi^-$  does not reach the DAPHNE detector due to hadronic interactions inside the target materials.

The background coming from the  $pn$  process is subtracted by applying the missing energy method. Taking into account the kinematic properties of this two body reaction the theoretically expected energy  $E_{theo}$  can be easily calculated. Plotting  $E_{theo}$  minus the experimentally measured energy  $E_{meas}$  Fig. 4.11 is obtained ( $E_{miss} = E_{theo} - E_{meas}$ ). The prominent peak around zero corresponds to the photodisintegration events while  $\pi^0$  production events have positive ( $E_{miss}$ ) values. A cut at  $E_{miss} = E_{theo} - E_{meas} < 80$  (vertical line in Fig. 4.11) is performed to completely suppress the  $pn$  background.

## 4.11 Analysis of the Double Polarization Data

The analysis algorithms of the helicity dependent single pion photoproduction data are basically the same as in the unpolarized case. Apart from trivial changes in the target dimensions, all applied conditions used for the event classification were the same as in the unpolarized case. The only relevant difference is the separation of the events according to the parallel or antiparallel relative beam-target orientation. The difference between these two orientations completely eliminates the contributions coming from the spinless C and O nuclei that could not be fully separated event by event from the polarized deuteron contribution. This subtraction is performed on the raw experimental yields, before the inclusion of the geometrical and the efficiency factors.

In the evaluation of the helicity dependent cross section, the degree of polarization of the photon beam ( $P_\gamma$ ) and of the target ( $P_T$ ) have to be taken into account. The procedure used to determine  $P_\gamma$  has been explained in section 3.2.4 while in section 3.8 a detailed explanation of the target degree of polarization analysis performed for the 2003 GDH experiment is given. This same algorithm was previously used also in the determination of the target degree of polarization for the 1998 data.

## 4.12 Detector Simulation

The estimation of the good pion photoproduction events rejected by all the different conditions applied in the analysis algorithms has been performed using a simulation code based on the GEANT (GEometry ANd Tracking) package [Bru84]. This code accurately

models the detector geometrical set-up. It takes into account the different resolutions and detection thresholds, and includes the same analysis procedures performed on the real data.

Below energies of a few GeV the standard GEANT code is not sufficiently accurate, for this reason some modifications were performed and implemented in the detector geometry [Ped98b]. This was possible by integrating the HADRIN and NUCRIN routines, they simulate the inelastic hadron-nucleon and inelastic hadron-nucleus interactions, respectively, at energies below 5 GeV [Han84].

Different event generators for the single pion photoproduction processes are implemented. Angular distributions from the SAID [Arn02] and HTD [Han98] models can be employed. Effects of the Fermi motion of a target nucleon can also be taken into account.

As it was explained in the previous section the GEANT simulation is not only used to obtain the identification efficiencies, but also to subtract the background contaminations and to simulate the quasi-free nucleon inside the deuteron.

## 4.13 Systematic Errors

Many sources of systematic errors must be considered: the measurement of the photon flux hitting the target has an error of 2%, the multiproportional wire chambers have an error in efficiency of 1%, the particle identification method systematical error is about 2%, and due to the background subtraction an error of 1% is introduced. Taking all this into account our total systematical error is about 3%.

In the case of the polarized channels the polarization parameter errors have also to be taken into account. The degree of polarization of the photon beam is measured using a Møller spectrometer that has 4% systematical error, on the other hand the error in the measurement of the target polarization is 2%. The total systematic error is about 5.5%.

The momentum distribution of the proton has to be taken into account. DAPHNE covers 94% of  $4\pi$ , but a part of the protons goes into forward angles and are thus undetected. Hence only a limited polar angular distribution is presented, and it is not enough to extrapolate reliably the measured differential cross section to get the total cross section. Additionally some protons that are inside the DAPHNE angular acceptance are lost because of their too low momentum.

In the next chapter the results of the analysis presented here are shown. Only statistical errors will be considered there.





---

---

# Chapter 5

## Results

---

---

*Truth is what stands the test of experience.*

Albert Einstein.

*Statistics: The only science that enables different experts  
using the same figures  
to draw different conclusions.*

Evan Esar.

### 5.1 Introduction

This chapter will present the results of the analysis of both the unpolarized and the helicity dependent differential cross section of three single pion photoproduction channels on the deuteron:

$$\begin{aligned}\gamma + d &\Rightarrow p_{spect} + p + \pi^- \\ \gamma + d &\Rightarrow n_{spect} + n + \pi^+ \\ \gamma + d &\Rightarrow n_{spect} + p + \pi^0\end{aligned}$$

All the presented data were taken at Mainz within the framework of the GDH experiment. The experimental setup and the analysis procedure was explained in the previous chapters. The unpolarized results obtained from the analysis are compared to previous data and models to test the analysis procedure. Once this is fixed some minor modifications in the code are done in order to analyse the doubly polarized data. These are the first of their kind and one of the primary results of this thesis.

First an explanation of the results is given for the unpolarized and polarized data. After this the plots and the tabulated tables are shown.

## 5.2 Unpolarized Channels

The unpolarized differential cross section of the three different reaction channels from detection threshold up to 500 MeV photon energy will be presented.

### 5.2.1 Results of the $\gamma + d \Rightarrow p_{spect} + p + \pi^-$ Reaction

Figure 5.2 shows the results of this work in comparison with data from Benz et al. [Ben77] and the model from A. Fix that was explained in chapter 2, for more information about this model refer to [Fix05]. As one can see there is a good agreement between the data themselves and with the theory. This gives us confidence in the analysis procedure and in the theoretical model. According to the model in this channel the impulse approximation dominates while the final state interaction does not have a relevant effect.

Table 5.1 shows the numerical values of the measured differential cross section for all photon energies.

### 5.2.2 Results of the $\gamma + d \Rightarrow n_{spect} + n + \pi^+$ Reaction

In figure 5.3 the differential cross section for the  $\pi^+$  photoproduction on deuterium is compared to the photoproduction on the proton [Pre01] and with the theoretical models for both channels ([Fix05] and [MAID]). The small difference between these two data are just due to the Fermi motion of the proton inside the deuteron, since most of the neutrons act merely like an spectator, as it was proven in section 4.8.

This idea is supported by the work of M. Mac Cormick et al [Cor96]. The total photoabsorption cross section per nucleon for hydrogen and deuterium presented in this work is shown in Fig. 5.1. In the energy region between 300 and 500 MeV, where only the single pion production plays a significant role, it can be clearly seen that for photon energies below 400 MeV the proton cross section is higher than that for the deuteron, while the situation reverses above. The same behavior is seen in the obtained  $\pi^+$  and  $\pi^0$  data (Fig. 5.3 and Fig. 5.4 respectively).

As in the previous channel the theoretical calculations show that the final state interaction effects are negligible, while the quasi-free proton interaction dominates. The agreement between the A. Fix model and the presented data are very good. Table 5.2 shows the numerical values.

### 5.2.3 Results of the $\gamma + d \Rightarrow n_{spect} + p + \pi^0$ reaction

Figure 5.4 shows the differential cross section of the  $\gamma + d \Rightarrow n_{spect} + p + \pi^0$  reaction versus the polar angle of the outgoing proton, since it is the only particle detected in the



analysis. As in the previous channel it is also compared to the photoproduction on the free proton [Pre01]. In this case the agreement data-model is not as good as in the charged pion channels. The theoretical calculations show that mainly the nucleon-nucleon and also the pion-nucleon final state interactions play an important role, hence this channel is more problematic. In order to explain these discrepancies other effects like the interaction between a resonance and the spectator nucleon or inelasticities in the nucleon-nucleon interaction should be taken into account.

The numerical values are presented in Table 5.3.

## 5.3 Polarized Channels

The good agreement of our unpolarized data with previously published data, and with the theoretical model give us confidence in the analysis procedure. With minor changes, it is used to obtain new data on the polarization channels. These results are the first of their kind since no other experiment has measured this before. The data were taken in a pilot experiment in 1998 at Mainz in the framework of the GDH experiment. About 150 hours of data were obtained. Due to the low statistics we are forced to enlarge the bin widths both in energy and in the polar angle in order to get reasonable error bars.

In the figures corresponding to the polarized reactions the helicity dependent differential cross section

$$\left(\frac{d\sigma}{d\Omega}\right)_{\text{helicity}} = \left(\frac{d\sigma}{d\Omega}\right)_{\text{parallel}} - \left(\frac{d\sigma}{d\Omega}\right)_{\text{antiparallel}} \quad (5.1)$$

will be plotted for the different measured channels, where *parallel* and *antiparallel* denote the relative spin orientation between the circularly polarized incoming photon beam and the linearly polarized deuterium target.

### 5.3.1 Results of the Polarized $\vec{\gamma} + \vec{d} \Rightarrow p_{\text{spect}} + p + \pi^-$ Reaction

Figure 5.5 shows the helicity dependent differential cross section versus the polar angle of the pion for several photon energies. The dashed black line is the prediction of this model for the free neutron  $\gamma + n \Rightarrow p + \pi^-$  reaction. As no free polarized neutron target is available models have to be used to get its properties. As one can see the agreement between data and model is reasonable, taking into account the large statistical error of the experimental data. Since this model has proven to reproduce the unpolarized data pretty well and the polarized channel in a reasonable way, one can rely on its predictions on the free neutron target. Table 5.4 contains the numerical values.

### 5.3.2 Results of the Polarized $\vec{\gamma} + \vec{d} \Rightarrow n_{spect} + n + \pi^+$ Reaction

In figure 5.6 one can see the helicity dependent differential cross section for the reaction  $\vec{\gamma} + \vec{d} \Rightarrow n_{spect} + n + \pi^+$  (red dots) compared to the theoretical model represented by the blue line. Data on the complementary free proton channel  $\vec{\gamma} + \vec{p} \Rightarrow n + \pi^+$  from [Pre01] (black triangles) and the MAID model (black dashed line) for this reaction are also shown for comparison. In order to compare properly these two data sets one has to take into account not only the Fermi motion, but also the fact that, due to the d-wave admixture in the deuteron wave function, the degree of polarization of the free proton inside the deuteron is not equal to the degree of polarization of the deuteron. In any case these two effects are smaller than 10%, while the statistical errors are much bigger.

In this case the agreement is not as good as in the unpolarized channel. The version of the MAID model used does not reproduce completely the polarized data on the proton. The model of A. Fix uses MAID as one input. Since MAID does not describe properly the proton this could partially explain the poor agreement of the A. Fix model with our results. On the other hand the tendency of the experimental data and both models are opposite. The MAID model for the proton is lower than the experimental data, while the A. Fix model for the deuteron is higher than the measured data.

In any case the experimental error bars are so large that no definitive conclusions can be extracted. Further theoretical calculations and more accurate experimental data are needed. In table 5.5 the numerical values of the helicity dependent differential cross section asymmetry and its statistical errors are presented.

### 5.3.3 Results of the Polarized $\vec{\gamma} + \vec{d} \Rightarrow n_{spect} + p + \pi^0$ Reaction

Figure 5.7 shows the helicity dependent differential cross section for the  $\vec{\gamma} + \vec{d} \Rightarrow n_{spect} + p + \pi^0$  reaction versus the polar angle of the outgoing proton  $\theta_p$ , which is the only detected particle in this reaction. It is compared with its complementary reaction on the free proton  $\vec{\gamma} + \vec{p} \Rightarrow p + \pi^0$  [Pre01]. In this case the models for both the proton and deuteron do not reproduce the data very precisely. Both of them slightly underestimate the experimental data, but they reproduce the shape correctly.

As in the case of the unpolarized channel final state interactions have an appreciable effect on the model calculations. Deeper theoretical investigations and more accurate data need to be provided. Table 5.6 shows the measured data values.

## 5.4 Unpolarized Results

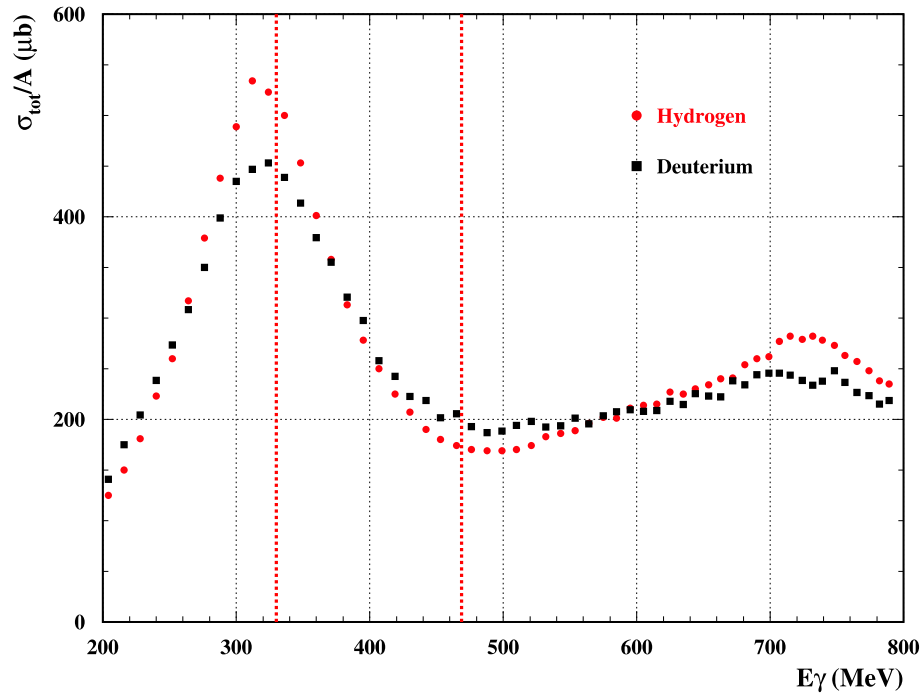


**Figure 5.1:** Total cross section normalized by the atomic mass as function of the incoming photon energy for proton and deuteron. Data from [Cor96]. The spread of the deuteron cross section is due to the Fermi motion. Between 300 and 500 MeV the same effect is seen in our data, see figures 5.3 and 5.4. The vertical lines represent the range of our measurement.

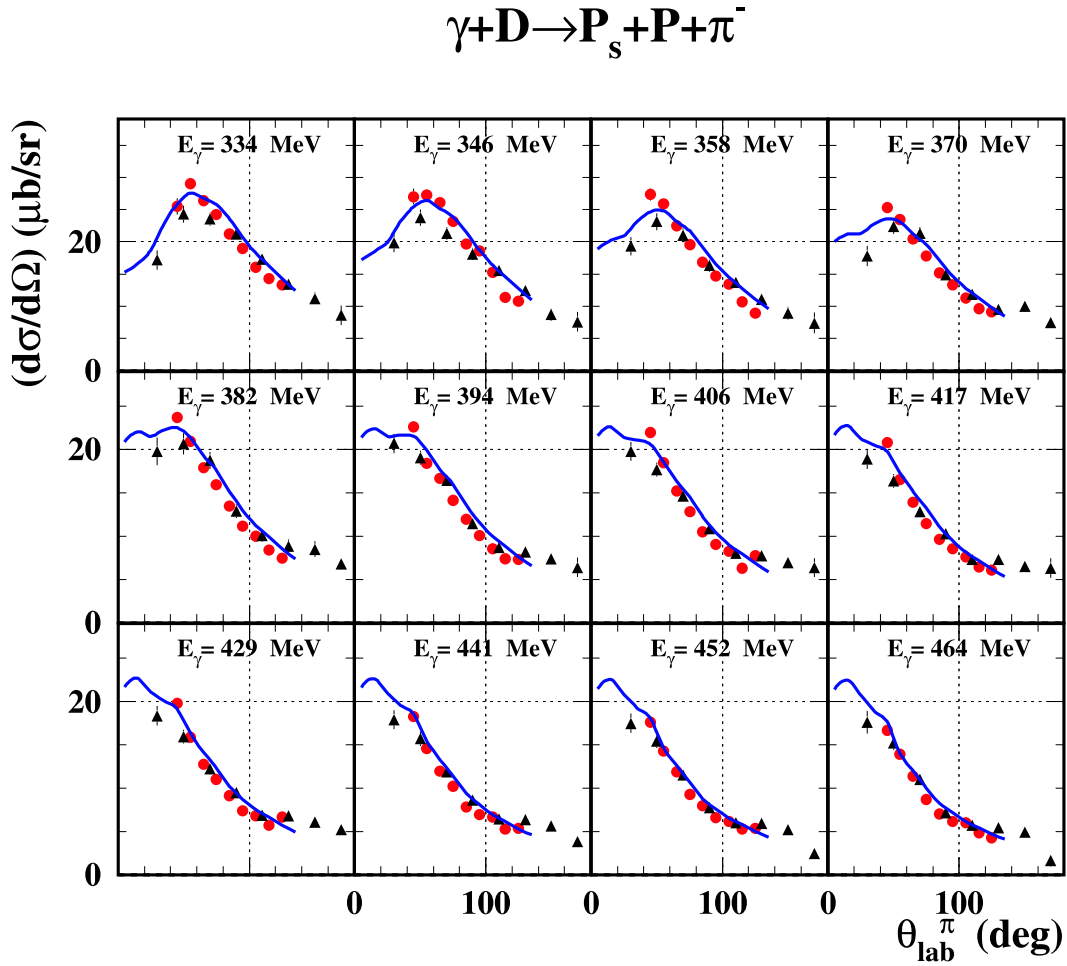


**Figure 5.2:** Unpolarized differential cross section of the  $\gamma + d \Rightarrow p_{spect} + p + \pi^-$  channel versus the polar angle of the pion in the laboratory frame. The red dots are the results of the present work. For comparison the data of [Ben77] represented by the black triangles. The blue line is the model [Fix05].

	$E_\gamma = 334 \text{ MeV}$	$E_\gamma = 346 \text{ MeV}$	$E_\gamma = 358 \text{ MeV}$	$E_\gamma = 370 \text{ MeV}$
$\vartheta_{lab}^\pi$	$\frac{d\sigma}{d\Omega}(\mu b) \pm \text{Error}$	$\frac{d\sigma}{d\Omega}(\mu b) \pm \text{Error}$	$\frac{d\sigma}{d\Omega}(\mu b) \pm \text{Error}$	$\frac{d\sigma}{d\Omega}(\mu b) \pm \text{Error}$
45.00	$16.64 \pm 0.36$	$17.56 \pm 0.37$	$18.22 \pm 0.38$	$19.75 \pm 0.40$
55.00	$13.88 \pm 0.28$	$14.29 \pm 0.28$	$14.52 \pm 0.28$	$15.88 \pm 0.30$
65.00	$11.36 \pm 0.24$	$11.90 \pm 0.25$	$11.95 \pm 0.24$	$12.70 \pm 0.25$
75.00	$8.70 \pm 0.22$	$9.28 \pm 0.22$	$10.17 \pm 0.23$	$11.00 \pm 0.23$
85.00	$7.02 \pm 0.20$	$7.96 \pm 0.21$	$7.83 \pm 0.20$	$9.11 \pm 0.22$
95.00	$6.15 \pm 0.21$	$6.59 \pm 0.21$	$6.92 \pm 0.21$	$7.37 \pm 0.21$
105.00	$6.00 \pm 0.25$	$6.15 \pm 0.24$	$6.68 \pm 0.25$	$6.79 \pm 0.24$
115.00	$4.83 \pm 0.31$	$5.26 \pm 0.32$	$5.27 \pm 0.30$	$5.71 \pm 0.31$
125.00	$4.28 \pm 0.51$	$5.31 \pm 0.51$	$5.37 \pm 0.48$	$6.66 \pm 0.52$
	$E_\gamma = 382 \text{ MeV}$	$E_\gamma = 394 \text{ MeV}$	$E_\gamma = 406 \text{ MeV}$	$E_\gamma = 417 \text{ MeV}$
$\vartheta_{lab}^\pi$	$\frac{d\sigma}{d\Omega}(\mu b) \pm \text{Error}$	$\frac{d\sigma}{d\Omega}(\mu b) \pm \text{Error}$	$\frac{d\sigma}{d\Omega}(\mu b) \pm \text{Error}$	$\frac{d\sigma}{d\Omega}(\mu b) \pm \text{Error}$
45.00	$20.78 \pm 0.42$	$21.90 \pm 0.45$	$22.61 \pm 0.47$	$23.70 \pm 0.50$
55.00	$16.53 \pm 0.29$	$18.46 \pm 0.31$	$18.35 \pm 0.31$	$20.95 \pm 0.34$
65.00	$13.86 \pm 0.25$	$15.18 \pm 0.26$	$16.65 \pm 0.27$	$17.87 \pm 0.27$
75.00	$11.45 \pm 0.23$	$12.83 \pm 0.23$	$14.13 \pm 0.24$	$15.92 \pm 0.25$
85.00	$9.58 \pm 0.21$	$10.51 \pm 0.22$	$11.95 \pm 0.23$	$13.44 \pm 0.24$
95.00	$8.54 \pm 0.22$	$9.06 \pm 0.22$	$10.06 \pm 0.23$	$11.13 \pm 0.23$
105.00	$7.57 \pm 0.25$	$8.21 \pm 0.25$	$8.52 \pm 0.24$	$9.99 \pm 0.26$
115.00	$6.40 \pm 0.30$	$6.26 \pm 0.28$	$7.40 \pm 0.30$	$8.35 \pm 0.31$
125.00	$6.04 \pm 0.46$	$7.76 \pm 0.49$	$7.32 \pm 0.48$	$7.44 \pm 0.44$
	$E_\gamma = 429 \text{ MeV}$	$E_\gamma = 441 \text{ MeV}$	$E_\gamma = 452 \text{ MeV}$	$E_\gamma = 464 \text{ MeV}$
$\vartheta_{lab}^\pi$	$\frac{d\sigma}{d\Omega}(\mu b) \pm \text{Error}$	$\frac{d\sigma}{d\Omega}(\mu b) \pm \text{Error}$	$\frac{d\sigma}{d\Omega}(\mu b) \pm \text{Error}$	$\frac{d\sigma}{d\Omega}(\mu b) \pm \text{Error}$
45.00	$25.29 \pm 0.55$	$27.31 \pm 0.95$	$27.00 \pm 1.19$	$25.53 \pm 1.28$
55.00	$23.43 \pm 0.36$	$25.85 \pm 0.59$	$27.24 \pm 0.76$	$29.03 \pm 0.82$
65.00	$20.39 \pm 0.29$	$22.47 \pm 0.46$	$26.05 \pm 0.61$	$26.36 \pm 0.62$
75.00	$17.76 \pm 0.26$	$19.54 \pm 0.41$	$23.16 \pm 0.54$	$24.19 \pm 0.54$
85.00	$15.16 \pm 0.25$	$16.83 \pm 0.39$	$19.62 \pm 0.50$	$21.18 \pm 0.50$
95.00	$13.36 \pm 0.25$	$14.73 \pm 0.39$	$18.59 \pm 0.51$	$18.93 \pm 0.51$
105.00	$11.30 \pm 0.26$	$13.37 \pm 0.43$	$15.24 \pm 0.53$	$16.03 \pm 0.54$
115.00	$9.60 \pm 0.31$	$10.67 \pm 0.50$	$11.41 \pm 0.59$	$14.30 \pm 0.65$
125.00	$9.08 \pm 0.48$	$8.96 \pm 0.68$	$10.83 \pm 0.85$	$13.35 \pm 0.91$

**Table 5.1:** Results of the differential cross section for the unpolarized  $\gamma + d \Rightarrow n_{spect} + p + \pi^-$  reaction.

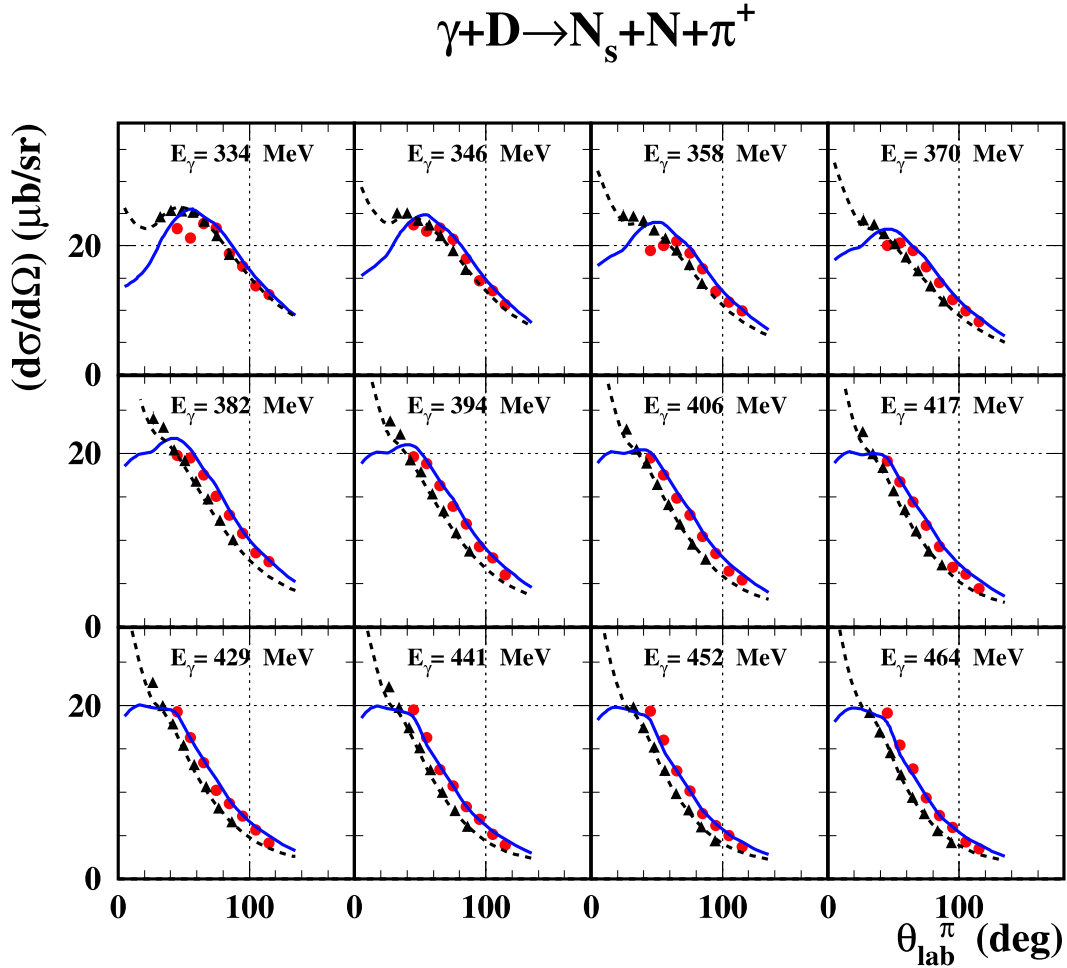


**Figure 5.3:** Unpolarized differential cross section data for the  $\gamma + d \Rightarrow n_{spect} + n + \pi^+$  reaction as function of the polar angle of the pion in the laboratory frame for different incoming photon energies. Red dots are the results of this work, and black triangles the unpolarized differential cross section of the  $\pi^+$  photoproduction on the free proton. The blue line is the model of A. Fix for the deuteron, and the black dashed line is the MAID model for the free proton.

	$E_\gamma = 334 \text{ MeV}$	$E_\gamma = 346 \text{ MeV}$	$E_\gamma = 358 \text{ MeV}$	$E_\gamma = 370 \text{ MeV}$
$\vartheta_{lab}^\pi$	$\frac{d\sigma}{d\Omega}(\mu b) \pm \text{Error}$	$\frac{d\sigma}{d\Omega}(\mu b) \pm \text{Error}$	$\frac{d\sigma}{d\Omega}(\mu b) \pm \text{Error}$	$\frac{d\sigma}{d\Omega}(\mu b) \pm \text{Error}$
45.00	19.10 $\pm$ 0.39	19.31 $\pm$ 0.39	19.47 $\pm$ 0.39	19.27 $\pm$ 0.40
55.00	15.41 $\pm$ 0.31	15.99 $\pm$ 0.32	16.31 $\pm$ 0.32	16.30 $\pm$ 0.32
65.00	12.63 $\pm$ 0.27	12.41 $\pm$ 0.27	12.57 $\pm$ 0.26	13.38 $\pm$ 0.27
75.00	9.31 $\pm$ 0.23	10.13 $\pm$ 0.24	10.68 $\pm$ 0.24	10.22 $\pm$ 0.23
85.00	7.31 $\pm$ 0.21	7.55 $\pm$ 0.21	8.32 $\pm$ 0.21	8.69 $\pm$ 0.22
95.00	5.89 $\pm$ 0.19	6.13 $\pm$ 0.19	6.88 $\pm$ 0.20	7.21 $\pm$ 0.20
105.00	4.29 $\pm$ 0.19	4.95 $\pm$ 0.20	5.12 $\pm$ 0.19	5.66 $\pm$ 0.19
115.00	3.47 $\pm$ 0.19	3.70 $\pm$ 0.19	3.88 $\pm$ 0.19	4.09 $\pm$ 0.19
	$E_\gamma = 382 \text{ MeV}$	$E_\gamma = 394 \text{ MeV}$	$E_\gamma = 406 \text{ MeV}$	$E_\gamma = 417 \text{ MeV}$
$\vartheta_{lab}^\pi$	$\frac{d\sigma}{d\Omega}(\mu b) \pm \text{Error}$	$\frac{d\sigma}{d\Omega}(\mu b) \pm \text{Error}$	$\frac{d\sigma}{d\Omega}(\mu b) \pm \text{Error}$	$\frac{d\sigma}{d\Omega}(\mu b) \pm \text{Error}$
45.00	19.12 $\pm$ 0.40	19.48 $\pm$ 0.41	19.60 $\pm$ 0.40	19.75 $\pm$ 0.40
55.00	16.73 $\pm$ 0.31	17.55 $\pm$ 0.32	18.80 $\pm$ 0.32	19.44 $\pm$ 0.33
65.00	14.40 $\pm$ 0.28	14.81 $\pm$ 0.27	16.27 $\pm$ 0.28	17.53 $\pm$ 0.28
75.00	11.69 $\pm$ 0.24	12.86 $\pm$ 0.24	13.87 $\pm$ 0.25	15.07 $\pm$ 0.25
85.00	9.23 $\pm$ 0.21	10.40 $\pm$ 0.22	11.88 $\pm$ 0.23	12.85 $\pm$ 0.23
95.00	6.88 $\pm$ 0.19	8.47 $\pm$ 0.20	9.27 $\pm$ 0.21	10.77 $\pm$ 0.22
105.00	6.07 $\pm$ 0.19	6.41 $\pm$ 0.20	7.92 $\pm$ 0.21	8.51 $\pm$ 0.21
115.00	4.43 $\pm$ 0.19	5.44 $\pm$ 0.20	5.99 $\pm$ 0.20	7.54 $\pm$ 0.22
	$E_\gamma = 429 \text{ MeV}$	$E_\gamma = 441 \text{ MeV}$	$E_\gamma = 452 \text{ MeV}$	$E_\gamma = 464 \text{ MeV}$
$\vartheta_{lab}^\pi$	$\frac{d\sigma}{d\Omega}(\mu b) \pm \text{Error}$	$\frac{d\sigma}{d\Omega}(\mu b) \pm \text{Error}$	$\frac{d\sigma}{d\Omega}(\mu b) \pm \text{Error}$	$\frac{d\sigma}{d\Omega}(\mu b) \pm \text{Error}$
45.00	20.03 $\pm$ 0.41	19.29 $\pm$ 0.62	23.26 $\pm$ 0.79	22.63 $\pm$ 0.77
55.00	20.47 $\pm$ 0.33	20.03 $\pm$ 0.49	22.26 $\pm$ 0.63	21.23 $\pm$ 0.61
65.00	19.30 $\pm$ 0.29	20.72 $\pm$ 0.45	22.76 $\pm$ 0.55	23.44 $\pm$ 0.55
75.00	16.71 $\pm$ 0.26	18.86 $\pm$ 0.41	21.06 $\pm$ 0.51	22.81 $\pm$ 0.51
85.00	14.34 $\pm$ 0.24	16.40 $\pm$ 0.38	18.02 $\pm$ 0.46	18.77 $\pm$ 0.46
95.00	11.69 $\pm$ 0.22	12.88 $\pm$ 0.35	14.54 $\pm$ 0.42	16.80 $\pm$ 0.45
105.00	9.95 $\pm$ 0.21	11.25 $\pm$ 0.35	13.07 $\pm$ 0.43	13.83 $\pm$ 0.43
115.00	8.27 $\pm$ 0.22	9.88 $\pm$ 0.37	10.86 $\pm$ 0.45	12.47 $\pm$ 0.46

**Table 5.2:** Results of the differential cross section for the unpolarized  $\gamma + d \Rightarrow n_{spect} + n + \pi^+$  reaction.

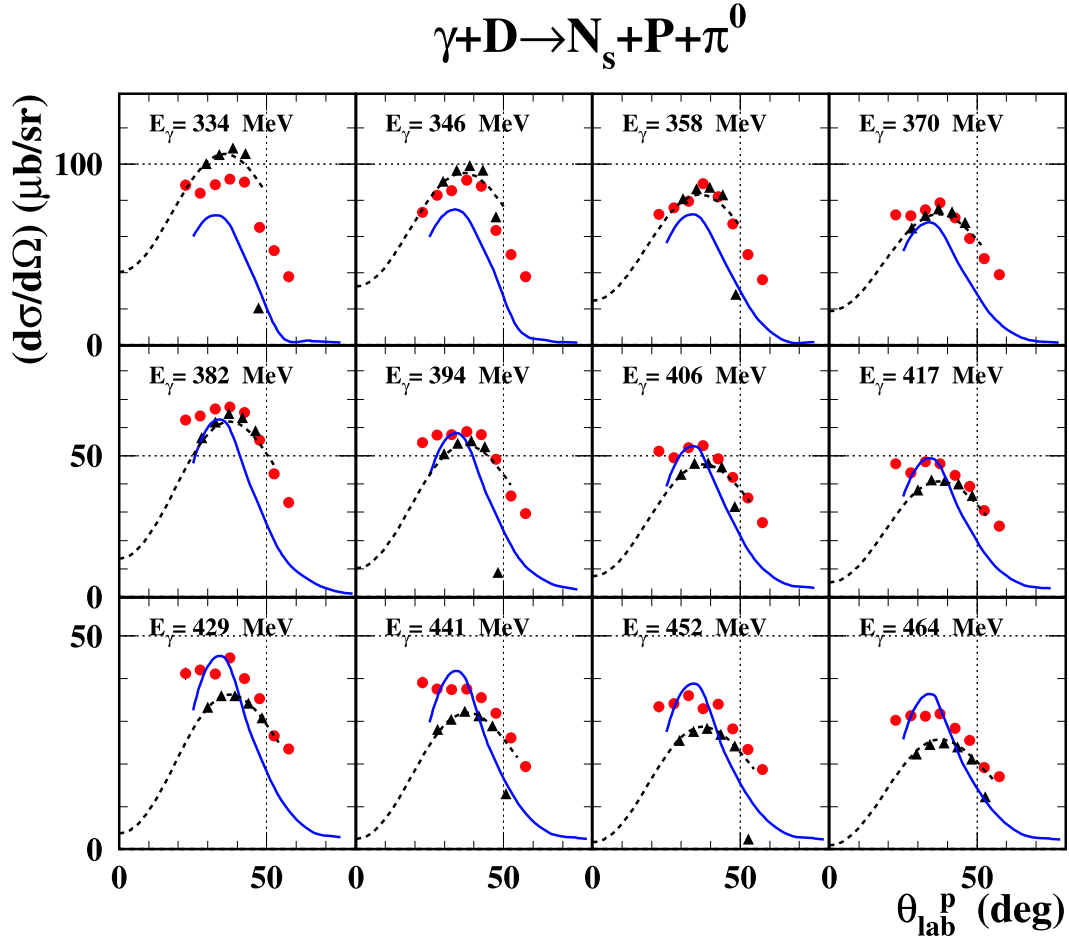


**Figure 5.4:** Unpolarized differential cross section versus polar angle of the proton for different photon energies for the reaction  $\gamma + d \Rightarrow n_{spect} + p + \pi^0$ . Red dots are the present work's results, compared to the A.Fix model represented by the blue line. Black triangles are the results of [Pre01] for the free proton reaction  $\gamma + p \Rightarrow p + \pi^0$  and the corresponding MAID model.



	$E_\gamma = 334$ MeV	$E_\gamma = 346$ MeV	$E_\gamma = 358$ MeV	$E_\gamma = 370$ MeV
$\vartheta_{lab}^p$	$\frac{d\sigma}{d\Omega}(\mu b) \pm \text{Error}$	$\frac{d\sigma}{d\Omega}(\mu b) \pm \text{Error}$	$\frac{d\sigma}{d\Omega}(\mu b) \pm \text{Error}$	$\frac{d\sigma}{d\Omega}(\mu b) \pm \text{Error}$
22.50	$30.20 \pm 1.25$	$33.40 \pm 1.35$	$39.07 \pm 1.43$	$41.19 \pm 1.46$
27.50	$31.33 \pm 0.74$	$34.15 \pm 0.75$	$37.56 \pm 0.77$	$42.00 \pm 0.82$
32.50	$31.21 \pm 0.67$	$36.01 \pm 0.71$	$37.43 \pm 0.71$	$41.04 \pm 0.74$
37.50	$31.81 \pm 0.65$	$32.99 \pm 0.65$	$37.58 \pm 0.67$	$44.83 \pm 0.75$
42.50	$28.37 \pm 0.59$	$33.99 \pm 0.66$	$35.60 \pm 0.65$	$39.98 \pm 0.68$
47.50	$25.53 \pm 0.57$	$28.26 \pm 0.60$	$31.92 \pm 0.63$	$35.28 \pm 0.68$
52.50	$19.15 \pm 0.51$	$23.38 \pm 0.58$	$26.13 \pm 0.63$	$26.62 \pm 0.64$
57.50	$17.01 \pm 0.57$	$18.66 \pm 0.60$	$19.40 \pm 0.61$	$23.49 \pm 0.72$
	$E_\gamma = 382$ MeV	$E_\gamma = 394$ MeV	$E_\gamma = 406$ MeV	$E_\gamma = 417$ MeV
$\vartheta_{lab}^p$	$\frac{d\sigma}{d\Omega}(\mu b) \pm \text{Error}$	$\frac{d\sigma}{d\Omega}(\mu b) \pm \text{Error}$	$\frac{d\sigma}{d\Omega}(\mu b) \pm \text{Error}$	$\frac{d\sigma}{d\Omega}(\mu b) \pm \text{Error}$
22.50	$47.18 \pm 1.48$	$51.56 \pm 1.51$	$54.69 \pm 1.52$	$62.66 \pm 1.59$
27.50	$43.93 \pm 0.80$	$49.26 \pm 0.82$	$57.28 \pm 0.91$	$64.06 \pm 0.94$
32.50	$47.83 \pm 0.79$	$52.89 \pm 0.79$	$57.56 \pm 0.82$	$66.65 \pm 0.88$
37.50	$47.08 \pm 0.73$	$53.60 \pm 0.78$	$58.62 \pm 0.80$	$67.32 \pm 0.87$
42.50	$43.08 \pm 0.70$	$48.95 \pm 0.74$	$57.47 \pm 0.83$	$65.37 \pm 0.89$
47.50	$39.08 \pm 0.71$	$42.44 \pm 0.73$	$48.81 \pm 0.82$	$55.56 \pm 0.90$
52.50	$30.58 \pm 0.68$	$35.01 \pm 0.76$	$35.73 \pm 0.77$	$43.56 \pm 0.91$
57.50	$25.16 \pm 0.72$	$26.41 \pm 0.74$	$29.57 \pm 0.83$	$33.38 \pm 0.97$
	$E_\gamma = 429$ MeV	$E_\gamma = 441$ MeV	$E_\gamma = 452$ MeV	$E_\gamma = 464$ MeV
$\vartheta_{lab}^p$	$\frac{d\sigma}{d\Omega}(\mu b) \pm \text{Error}$	$\frac{d\sigma}{d\Omega}(\mu b) \pm \text{Error}$	$\frac{d\sigma}{d\Omega}(\mu b) \pm \text{Error}$	$\frac{d\sigma}{d\Omega}(\mu b) \pm \text{Error}$
22.50	$71.99 \pm 1.71$	$72.19 \pm 2.58$	$73.43 \pm 3.07$	$88.26 \pm 3.41$
27.50	$71.30 \pm 0.97$	$75.68 \pm 1.51$	$82.67 \pm 1.91$	$83.89 \pm 1.97$
32.50	$74.62 \pm 0.93$	$79.39 \pm 1.44$	$85.36 \pm 1.84$	$88.71 \pm 1.94$
37.50	$78.57 \pm 0.97$	$89.18 \pm 1.58$	$91.03 \pm 1.93$	$91.76 \pm 2.02$
42.50	$70.29 \pm 0.93$	$81.80 \pm 1.61$	$87.69 \pm 2.08$	$90.03 \pm 2.32$
47.50	$58.88 \pm 0.92$	$67.03 \pm 1.61$	$63.38 \pm 1.98$	$64.86 \pm 2.10$
52.50	$47.70 \pm 1.00$	$50.10 \pm 1.63$	$49.99 \pm 2.08$	$52.27 \pm 2.32$
57.50	$38.93 \pm 1.10$	$35.94 \pm 1.65$	$37.74 \pm 1.99$	$37.65 \pm 2.22$

**Table 5.3:** Results of the differential cross section for the unpolarized  $\gamma + d \Rightarrow n_{spect} + p + \pi^0$  reaction.

## 5.5 Polarized Results

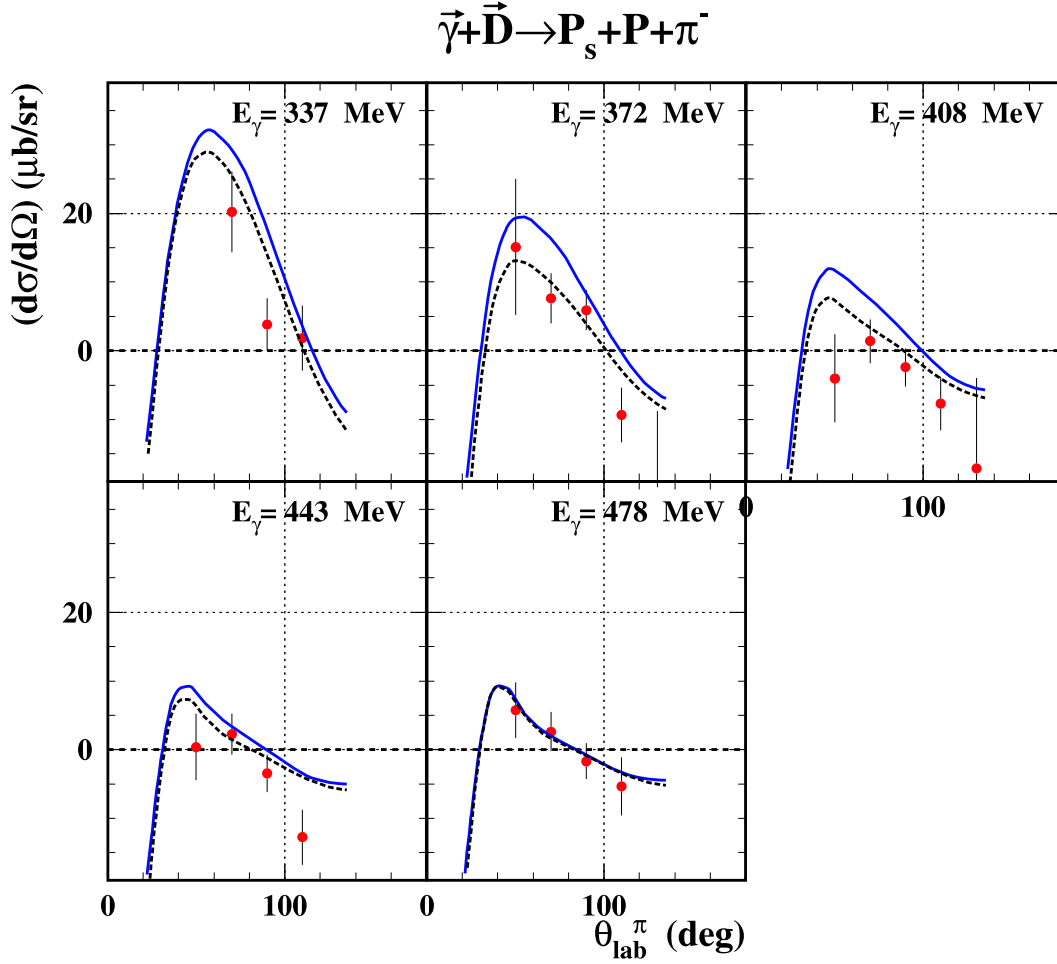


**Figure 5.5:** Helicity dependent differential cross section  $\frac{d\sigma}{d\Omega_{parallel}} - \frac{d\sigma}{d\Omega_{antiparallel}}$  from the polar angle  $\vartheta_{lab}^{\pi}$  of the pion in the laboratory frame. Red dots are the results of this work compared to the blue line of the theoretical model. Black dashed line represent the prediction of this model for the free neutron target reaction:  $\gamma + n \Rightarrow p + \pi^-$ .

	$E_\gamma = 335 \text{ MeV}$	$E_\gamma = 372 \text{ MeV}$	$E_\gamma = 408 \text{ MeV}$
$\vartheta_{lab}^\pi$	$\frac{d\sigma}{d\Omega}(\mu b) \pm \text{Error}$	$\frac{d\sigma}{d\Omega}(\mu b) \pm \text{Error}$	$\frac{d\sigma}{d\Omega}(\mu b) \pm \text{Error}$
50.00	$5.74 \pm 4.09$	$0.39 \pm 4.84$	$-4.01 \pm 6.44$
70.00	$2.61 \pm 2.87$	$2.24 \pm 2.97$	$1.39 \pm 3.18$
90.00	$-1.70 \pm 2.62$	$-3.47 \pm 2.71$	$-2.42 \pm 2.78$
110.00	$-5.37 \pm 4.23$	$-12.77 \pm 4.01$	$-7.71 \pm 3.90$
130.00	$16.20 \pm 17.96$	$-4.46 \pm 14.24$	$-17.14 \pm 13.20$
	$E_\gamma = 443 \text{ MeV}$	$E_\gamma = 478 \text{ MeV}$	-
$\vartheta_{lab}^\pi$	$\frac{d\sigma}{d\Omega}(\mu b) \pm \text{Error}$	$\frac{d\sigma}{d\Omega}(\mu b) \pm \text{Error}$	-
50.00	$15.13 \pm 9.93$	$-36.75 \pm 22.30$	-
70.00	$7.65 \pm 3.64$	$20.23 \pm 5.85$	-
90.00	$5.93 \pm 2.95$	$3.81 \pm 3.83$	-
110.00	$-9.34 \pm 4.01$	$1.84 \pm 4.75$	-
130.00	$-20.59 \pm 11.79$	$-27.38 \pm 13.26$	-

**Table 5.4:** Results of the helicity dependent differential cross section for the polarized  $\vec{\gamma} + \vec{d} \Rightarrow n_{spect} + p + \pi^-$  reaction.

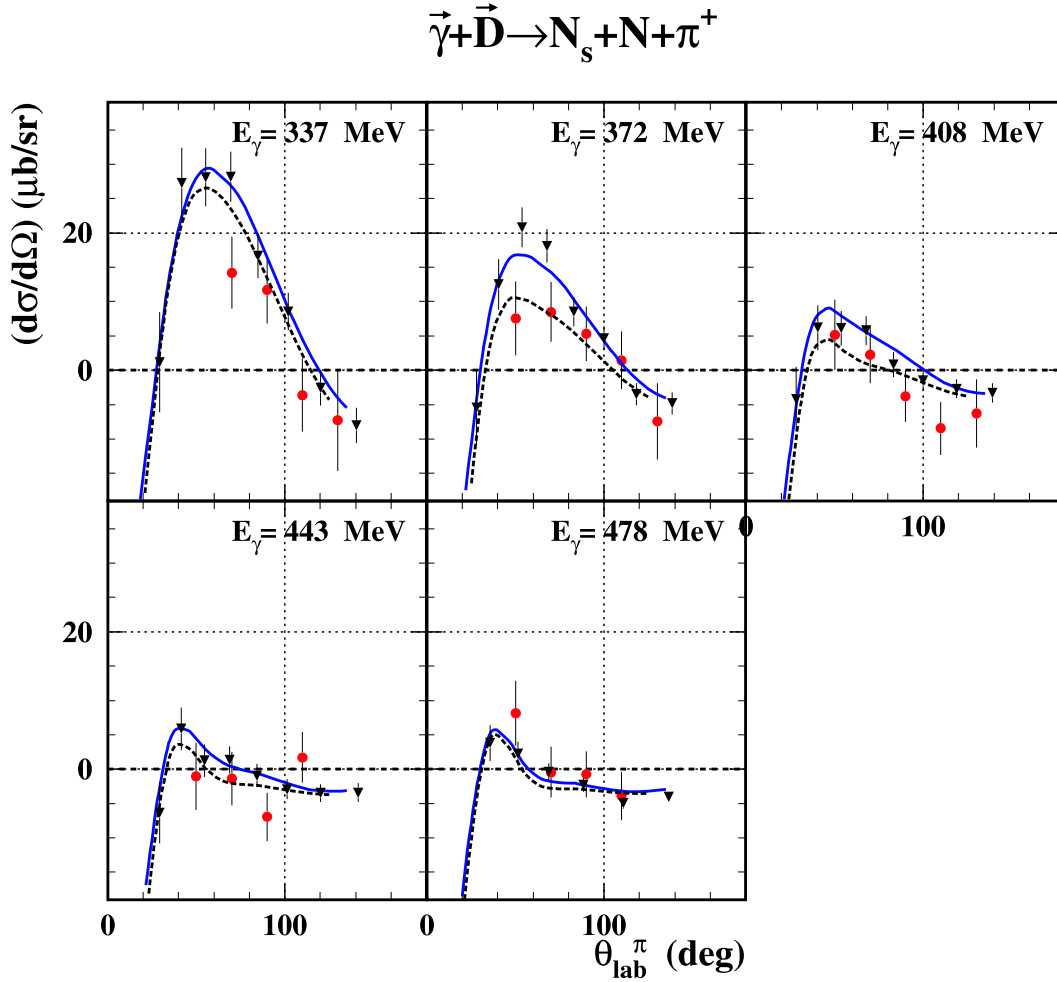


**Figure 5.6:** Helicity dependent differential cross section for the  $\pi^+$  photoproduction on the deuteron versus the polar angle of the outgoing pion for several photon energies. Red dots are the results of this work compared to the model calculations represented by the blue line. Black triangles are data from [Pre01] on the  $\pi^+$  photoproduction on free proton, while dashed black line are the MAID model for this reaction.

	$E_\gamma = 335 \text{ MeV}$	$E_\gamma = 372 \text{ MeV}$	$E_\gamma = 408 \text{ MeV}$
$\vartheta_{lab}^\pi$	$\frac{d\sigma}{d\Omega}(\mu b) \pm \text{Error}$	$\frac{d\sigma}{d\Omega}(\mu b) \pm \text{Error}$	$\frac{d\sigma}{d\Omega}(\mu b) \pm \text{Error}$
50.00	$8.17 \pm 4.71$	$-1.06 \pm 4.87$	$5.13 \pm 5.13$
70.00	$-0.44 \pm 3.67$	$-1.39 \pm 3.89$	$2.21 \pm 4.06$
90.00	$-0.75 \pm 3.38$	$-6.94 \pm 3.52$	$-3.83 \pm 3.72$
110.00	$-3.89 \pm 3.51$	$1.69 \pm 3.69$	$-8.45 \pm 3.86$
130.00	$-20.43 \pm 4.44$	$-13.27 \pm 4.59$	$-6.28 \pm 4.94$
	$E_\gamma = 443 \text{ MeV}$	$E_\gamma = 478 \text{ MeV}$	-
$\vartheta_{lab}^\pi$	$\frac{d\sigma}{d\Omega}(\mu b) \pm \text{Error}$	$\frac{d\sigma}{d\Omega}(\mu b) \pm \text{Error}$	-
50.00	$7.57 \pm 5.40$	$66.36 \pm 6.35$	-
70.00	$8.50 \pm 4.38$	$14.21 \pm 5.28$	-
90.00	$5.29 \pm 3.97$	$11.68 \pm 4.90$	-
110.00	$1.46 \pm 4.19$	$-3.63 \pm 5.30$	-
130.00	$-7.42 \pm 5.55$	$-7.31 \pm 7.33$	-

**Table 5.5:** Results of the helicity dependent differential cross section for the polarized  $\vec{\gamma} + \vec{d} \Rightarrow n_{spect} + n + \pi^+$  reaction.

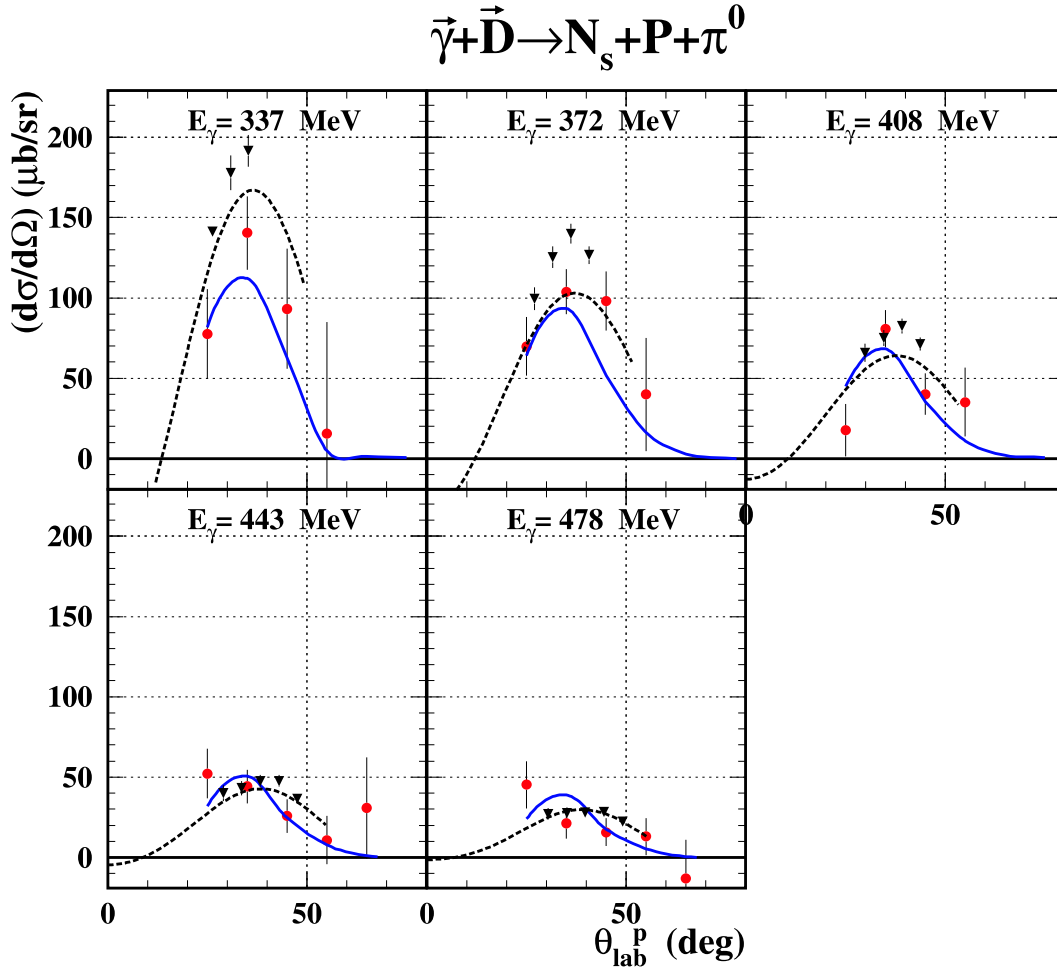


**Figure 5.7:** Results for the helicity dependent differential  $\pi^0$  photoproduction cross section on the deuteron from the polar angle of the proton for several photon energies. The red dots are the results of the present work, the blue line is the model of A. Fix, the black triangle are the data from the  $\pi^0$  photoproduction cross section asymmetry on the proton, and the dashed black line the MAID model for the proton data.

	$E_\gamma = 335 \text{ MeV}$	$E_\gamma = 372 \text{ MeV}$	$E_\gamma = 408 \text{ MeV}$
$\vartheta_{lab}^p$	$\frac{d\sigma}{d\Omega}(\mu b) \pm \text{Error}$	$\frac{d\sigma}{d\Omega}(\mu b) \pm \text{Error}$	$\frac{d\sigma}{d\Omega}(\mu b) \pm \text{Error}$
25.00	$45.21 \pm 14.63$	$52.22 \pm 15.43$	$17.76 \pm 16.27$
35.00	$21.17 \pm 9.57$	$44.17 \pm 10.36$	$80.87 \pm 11.47$
45.00	$15.75 \pm 8.72$	$25.76 \pm 10.41$	$40.05 \pm 12.97$
55.00	$13.11 \pm 11.51$	$10.65 \pm 15.05$	$35.18 \pm 21.28$
65.00	$-12.96 \pm 23.96$	$30.73 \pm 31.55$	$28.65 \pm 45.98$
	$E_\gamma = 443 \text{ MeV}$	$E_\gamma = 478 \text{ MeV}$	-
$\vartheta_{lab}^p$	$\frac{d\sigma}{d\Omega}(\mu b) \pm \text{Error}$	$\frac{d\sigma}{d\Omega}(\mu b) \pm \text{Error}$	-
25.00	$69.88 \pm 18.30$	$77.64 \pm 27.91$	-
35.00	$103.81 \pm 13.97$	$140.42 \pm 22.85$	-
45.00	$98.20 \pm 18.37$	$93.23 \pm 37.43$	-
55.00	$39.84 \pm 35.09$	$15.38 \pm 69.57$	-
65.00	$82.79 \pm 74.70$	$40.20 \pm 132.90$	-

**Table 5.6:** Results of the helicity dependent differential cross section for the polarized  $\vec{\gamma} + \vec{d} \Rightarrow n_{spect} + p + \pi^0$  reaction.





---

---

# Chapter 6

## Conclusions and outlook

---

---

*There is no way to happiness,  
happiness is the way.*

The Buddha.

### 6.1 Conclusions

In this work unpolarized and polarized data on three single pion photoproduction channels were presented and compared with previous measurements and a theoretical model developed by A. Fix and H. Arenhövel.

Both unpolarized charged pion reactions are in good agreement with previous measurement, and the model reproduces them satisfactorily. For the uncharged pion channel the agreement between model and data is not as good as in the charged pion reactions. In this case the nucleon-nucleon and pion-nucleon final state interactions play a relevant role. Further theoretical improvements should include other two body effects, like the interaction between a resonance and the spectator nucleon, or the inelasticities in the nucleon-nucleon interaction.

Unpolarized data on deuterium compared to data on the free proton show the effect of the fermi motion of the target nuclei also observed by previous experiments.

New doubly polarized data on the single pion photoproduction on the deuteron are presented. These data have been obtained using a circularly polarized photon beam from the MAMI accelerator and a longitudinally polarized deuteron target. These are the first of their kind since such an experiment has never been carried out before.

The helicity dependent differential cross section for three single pion photoproduction channels was presented, and compared with a theoretical model and with the data on the free proton. Due to the low statistics collected in this pilot experiment error bars larger than in the unpolarized channels results.

Within the error bars a relatively good agreement with the model is obtained for the  $\pi^-$  and the  $\pi^0$  channels. In the  $\pi^+$  channel an unexplained effect is observed. The model on the free proton underestimated the data, while the opposite behavior is seen with the deuteron data and its corresponding model. This effect is more visible at low photon energies. In any case the error bars are so large that no definitive conclusion can be extracted. For all polarized channels the model reproduces correctly the shape of the experimental data. Further theoretical investigations and more accurate polarized data are urgently needed.

The analysis of the target degree of polarization measurement of the 2003 nGDH sum rule experiment carried out at Mainz were presented. These data contribute directly, not only to the evaluation of the GDH sum rule, but also to the analysis of the different partial reaction channels.

An extensive explanation of the different theoretical aspects of a frozen spin target, and the actual status of the new Mainz frozen spin target (MaiFroST) are presented. The microwave system is tested and ready to be used. The nuclear magnetic resonance system is currently being built in close collaboration with Bochum and Zagreb groups. The final version of the circuit is designed, and all the necessary electronics pieces and devices are in Mainz. The superconducting magnet that will be used for the polarization of the target is tested and working reliably. All the helium circuits and the roots pumps are leak tested, and ready to be used. The hardware and software control system is reliably working and monitoring all important parameters. The cryostat was tested with liquid nitrogen, and no leak was found.

## 6.2 Outlook

The data taken in the GDH sum rule experiment performed at Mainz in 2003 are currently under analysis. They will bring more accurate results. A reduction of the error bars by a factor of 4 is expected.

The final test of the dilution cryostat will be done in Mainz soon. A complete test of the MaiFroST have to be performed before it can be installed in the experimental hall.

New proposals for a transversely polarized target are currently under study. Additionally, the tensor polarization contribution to the helicity dependent differential cross section could be measured.





# List of Figures

---

---

2.1	Kinematics of the pion photoproduction. . . . .	9
2.2	Feynman diagrams of the theoretical model. . . . .	11
3.1	Floor plan of MAMI-B. . . . .	18
3.2	The Glasgow-Mainz tagger. . . . .	20
3.3	The pair detector. . . . .	21
3.4	Polarization transfer via Bremsstrahlung. . . . .	23
3.5	The Møller polarimeter. . . . .	24
3.6	A2 experimental hall. . . . .	26
3.7	DAPHNE detector. . . . .	27
3.8	MWPC: Impact reconstruction. . . . .	28
3.9	MWPC: Track reconstruction. . . . .	29
3.10	MIDAS detector. . . . .	31
3.11	Čerenkov detector. . . . .	32
3.12	Unpolarized target cell. . . . .	34
3.13	Energy levels electron-nucleon. . . . .	38
3.14	Level transitions. . . . .	39
3.15	Dynamical nuclear polarization process. . . . .	40
3.16	NMR circuit. . . . .	42
3.17	Energy level deuteron, quadrupole interaction shift. . . . .	44
3.18	Deuteron NMR signal. . . . .	45
3.19	Vapor pressure of liquid $^3\text{He}$ and $^4\text{He}$ . . . . .	47
3.20	Labda line diagram. . . . .	49
3.21	Flow diagram of a dilution cryostat. . . . .	53
3.22	Internal magnetic field in superconductors . . . . .	55

3.23	Bonn's cryostat. . . . .	56
3.24	Bonn's holding magnet. . . . .	58
3.25	Dubna-Mainz cryostat. . . . .	60
3.26	High temperature heat exchangers. . . . .	62
3.27	Tube-in-tube heat exchangers. . . . .	62
3.28	Low temperature heat exchangers. . . . .	63
3.29	Cinter heat exchangers. . . . .	63
3.30	Polarizing magnet . . . . .	65
3.31	Simulated magnetic field. . . . .	66
3.32	Microwave system. . . . .	67
3.33	Parameters first microwave source. . . . .	69
3.34	Parameters second microwave source. . . . .	69
3.35	Cryostat control system. . . . .	71
3.36	$^4\text{He}$ pre-cooling line. . . . .	73
3.37	$^3\text{He}$ line. . . . .	75
3.38	Cooling trap . . . . .	76
3.39	NMR signal, July 2003. . . . .	77
3.40	NMR fit, July 2003, . . . . .	78
3.41	Target polarization June 2003. . . . .	81
3.42	Target polarization July 2003 . . . . .	81
4.1	Holes in $\varphi$ . . . . .	88
4.2	Geometrical cuts unpolarized target. . . . .	89
4.3	Geometrical cuts polarized target. . . . .	90
4.4	Effective target length. . . . .	92
4.5	TDC spectrum. . . . .	93
4.6	$\Delta E/E$ -plot. . . . .	95
4.7	Banana plot. . . . .	97
4.8	Geometrical range method. . . . .	99
4.9	Partial channel analysis. . . . .	100
4.10	Proton spectator momentum. . . . .	102
4.11	Missing energy plot. . . . .	104
5.1	Hydrogen and deuterium total cross section. . . . .	113
5.2	Unpolarized differential cross section $\gamma + d \Rightarrow p_{spect} + p + \pi^-$ . . . . .	114

---

5.3	Unpolarized differential cross section $\gamma + d \Rightarrow n_{spect} + n + \pi^+$ . . . . .	116
5.4	Unpolarized differential cross section $\gamma + d \Rightarrow n_{spect} + p + \pi^0$ . . . . .	118
5.5	Helicity dependent differential cross section $\vec{\gamma} + \vec{d} \Rightarrow p_{spect} + p + \pi^-$ . . . . .	120
5.6	Helicity dependent differential cross section $\vec{\gamma} + \vec{d} \Rightarrow n_{spect} + n + \pi^+$ . . . . .	122
5.7	Helicity dependent differential cross section $\vec{\gamma} + \vec{d} \Rightarrow n_{spect} + p + \pi^0$ . . . . .	124





# List of Tables

---

3.1	MAMI RTM parameters . . . . .	19
3.2	MWPC parameters . . . . .	29
3.3	MWPC efficiencies . . . . .	30
3.4	g-factor and magneton . . . . .	36
3.5	Relaxation time . . . . .	80
4.1	Target parameters . . . . .	85
4.2	Target thickness . . . . .	91
5.1	Differential cross section $\gamma + d \Rightarrow n_{spect} + p + \pi^-$ . . . . .	115
5.2	Differential cross section $\gamma + d \Rightarrow n_{spect} + n + \pi^+$ . . . . .	117
5.3	Differential cross section $\gamma + d \Rightarrow n_{spect} + p + \pi^0$ . . . . .	119
5.4	Helicity dependent differential cross section $\vec{\gamma} + \vec{d} \Rightarrow n_{spect} + p + \pi^-$ . . . . .	121
5.5	Helicity dependent differential cross section $\vec{\gamma} + \vec{d} \Rightarrow n_{spect} + n + \pi^+$ . . . . .	123
5.6	Helicity dependent differential cross section $\vec{\gamma} + \vec{d} \Rightarrow n_{spect} + p + \pi^0$ . . . . .	125



# Bibliography

---

- [Abe97] K. Abe et al., *Precision Determination of the Neutron Spin Structure Function  $g_1^n$* , Phys. Rev. Lett. **79** (1997) 26
- [Abe98] K. Abe et al., *Measurements of the Proton and Deuteron Spin Structure Functions  $g_1$  and  $g_2$* , Phys. Rev. **D58** (1998) 112003
- [Abr78] A. Abragam and M. Goldman, *Principles of dynamic nuclear polarisation* Rep. Prog. Phys. **41** (1978) 395
- [Ack98] K. Ackerstaff et al., *Determination of the Deep Inelastic Contribution to the Generalized Gerasimov-Drell-Hearn Integral for the Proton and Neutron*, Phys. Lett. **B444** (1998) 531
- [Ack99] K. Ackerstaff et al., *Flavor Decomposition of the Polarized Quark Distributions in the Nucleon from Inclusive and Semi-inclusive Deep-inelastic Scattering*, Phys. Lett. **B464** (1999) 123
- [Ada97] D. Adams et al., *Spin structure of the proton from polarized inclusive deep-inelastic muon-proton scattering*, Phys. Rev. **D56** (1997) 5330
- [Ade96] B. Adeva et al., *Large Enhancement of Deuteron Polarization with Frequency Modulated Microwaves*, Nucl. Instr. Meth. **372** (1996) 339
- [Ade98] D. Adeva et al., *Spin asymmetries  $A_1$  and structure functions  $g_1$  of the proton and the deuteron from polarized high energy muon scattering*, Phys. Rev. **D58** (1998) 112001
- [Agu05] P. Aguar Bartolomé, *Prestudy for the use of the polarised  $^3\text{He}$  target at the photon beam of MAMI*, Diploma Thesis, University of Mainz, 2005.
- [Ahr00] J. Ahrens et al., *Helicity Dependence of  $\gamma p \rightarrow N\pi$  below 450 MeV and Contribution to the Gerasimov-Drell-Hearn Sum Rule*, Phys. Rev. Lett. **84** (2000) 5950

- [Ahr01] J. Ahrens et al., *First measurement of the Gerasimov-Drell-Hearn integral for  $^1\text{H}$  from 200 to 800 MeV*, Phys. Rev. Lett. **87** (2001) 022003
- [Air98] A. Airapetian et al., *Measurement of the Proton Spin Structure Function  $g_1^p$  with a Pure Hydrogen Target*, Phys. Lett. **B442** (1998) 484
- [Air00] A. Airapetian et al., *Measurement of the Spin Asymmetry in the Photoproduction of Pairs of High- $p_T$  Hadrons at HERMES*, Phys. Rev. Lett. **84** (2000) 2584
- [Alt00] S. Altieri et al., *A Compact Solid State Detector for Small Angle Particle Tracking*, Nucl. Instr. Meth. **A452** (2000) 185
- [Ann96] J. R. M. Annand, I. Anthony and B. Oussena, *ACQU a data acquisition and analysis system for medium energy physics experiments*, Nucl. Instr. Meth. **A368** (1996) 385
- [Ant91] I. Anthony et al., *Design of a tagged photon spectrometer for use with the Mainz 840 MeV microtron*, Nucl. Instr. Meth. **A301** (1991) 230
- [Ant96] P. L. Anthony et al., *Deep Inelastic Scattering of Polarized Electrons by Polarized  $^3\text{He}$  and the Study of the Neutron Spin Structure*, Phys. Rev. **D54** (1996) 6620
- [Arn02] R. A. Arndt et al., *Analysis of pion photoproduction data*, Phys. Rev. **C66** (2002) 055213  
available at <http://gwdac.phys.gwu.edu/>
- [Ash88] J. Ashman et al., *A measurement of the spin asymmetry and determination of the structure function  $g_1$  in deep inelastic muon-proton scattering*, Phys. Lett. **B206** (1988) 364
- [Ash89] J. Ashman et al., *An investigation of the spin structure of the proton in deep inelastic scattering of polarized muons on polarized protons*, Nucl. Phys. **B328** (1989) 1
- [Aud91] G. Audit et al., *DAPHNE: a large-acceptance tracking detector for the study of photoreactions at intermediate energies*, Nucl. Instr. Meth. **A301** (1991) 473
- [Aul99] K. Aulenbacher et al., *The MAMI source of polarized electrons*, Nucl. Instr. Meth. **A391** (1997) 498
- [Bar57] J. Bardeen, L. N. Cooper and J. R. Shieffer, *Theory of superconductivity*, Phys. Rev. **108** (1957) 1175

- [Baz98] N. A. Bazhanov et al., *Frozen spin solid targets developed at the Laboratory of Nuclear Problems (JINR, Dubna)*, Nucl. Instr. Meth. **A402** (1998) 484
- [Ben77] P. Benz et al., *Measurements of the reaction  $\gamma d \rightarrow \pi^- pp$ , and determination of cross section for the reaction  $\gamma n \rightarrow \pi^- p$ , at photon energies between 0.2 and 2.0 GeV*, Nucl. Phys. **B65** (1973) 158
- [Ber67] F. A. Berends, A. Donnachie and D. L. Weaver, *Photoproduction and electroproduction of pions. (I) Dispersion relation theory*, Nucl. Phys. **B4** (1967) 1
- [Blo77] I. Blomqvist and J. M. Laget, *A non-relativistic operator convenient for analysis of pion photoproduction on nuclei in the  $\Delta(1236)$  region*, Nucl. Phys. **A280** (1977) 405
- [Bra94] A. Braghieri et al., *A Range telescope technique for particle discrimination and energy reconstruction*, Nucl. Instr. Meth. **A343** (1994) 623
- [Bra99] C. Bradtke, *A new Frozen Spin Target for the measurement of the helicity asymmetry of the total photoabsorption cross-section*, Ph.D. Thesis, University of Bonn, 1996.
- C. Bradtke et al., *A new frozen-spin target for  $4\pi$  particle detection*, Nucl. Instr. Meth. **A436** (1999) 430
- [Bru84] R. Brun et al., *GEANT3 Users's guide*, CERN DD/EE 84-1, 1987
- [Car53] T. R. Carver and C. P. Slichter, *Polarization of Nuclei in Metals*, Phys. Rev. **92** (1953) 212
- [Cha90] P. Chaumette et al., *Dilution refrigerator and solenoid for the Fermilab spin physics facility*, Adv. Cryog. Eng. **35B** (1990) 1067
- P. Chaumette et al., *First use of the polarized target facility at Fermilab*, Proc. of the 9th Intern. Symp. on High Energy Spin Phys. **2** (1990) 237
- [Che51] G. F. Chew and H. W. Lewis, *A Phenomenological Treatment of Photomeson Production from Deuterons*, Phys. Rev. **84** (1951) 779
- [Che57] G. F. Chew, M. L. Goldberger, F. E. Low and Y. Nambu, *Relativistic Dispersion Relation Approach to Photomeson Production*, Phys. Rev. **106** (1957) 1345
- [Cor96] M. MacCormick et al., *Total photoabsorption cross section for  $^1H$ ,  $^2H$  and  $^3He$  from 200 to 800 MeV*, Phys. Rev. **53** (1996) 41

- [Dar03] E. M. Darwish, H. Arenhövel and M. Schwamb, *Influence on final state interaction on incoherent pion photoproduction on the deuteron in the region of the  $\Delta$ -resonance*, Eur. Phys. J. **A16** (2003) 111  
E. M. Darwish, H. Arenhövel and M. Schwamb, *Final-state interaction in spin asymmetry and GDH sum rule for incoherent pion production on the deuteron*, Eur. Phys. J. **A17** (2003) 514
- [Das65] P. Das, R. De Bruyn Ouboter and K. W. Tachonis, *Proc. 9th Int. Conf. on Low Tem. Phys.*, Plenum Press London (1965) 1253
- [Dre66] S. D. Drell and A. C. Hearn, *Exact sum rule for nucleon magnetic moments*, Phys. Rev. Lett. **16** (1966) 908
- [Dul96] C. M. Dulya, Ph.D. Thesis, University Los Angeles, 1996.  
C. M. Dulya et al., *A Line shape analysis for spin 1 NMR signals.*, Nucl. Instr. Meth. **A398** (1997) 109
- [Dut95] H. Dutz et al., *An internal superconducting "holding-coil" for frozen spin targets*, Nucl. Instr. Meth. **A356** (1995) 111
- [Dut03] H. Dutz et al., *First Measurement of the Gerasimov-Drell-Hearn Sum Rule for  $^1H$  from 0.7 to 1.8 GeV at ELSA*, Phys. Rev. Lett. **91** (2003) 192001
- [Dut04] H. Dutz et al., *Experimental Check of the Gerasimov-Drell-Hearn Sum Rule for  $^1H$* , Phys. Rev. Lett. **93** (2004) 032003
- [Dut05] H. Dutz et al., *Measurement of the Helicity-Dependence Photoabsorption Cross Sections on the Neutron from 815 to 1825 MeV*, Phys. Rev. Lett. **94** (2005) 162001
- [Emm95] H. Emmerich, Ph.D. Thesis, University of Mainz, 1995.
- [Fix05] H. Arenhövel and A. Fix, *Incoherent pion photoproduction on the deuteron with polarization observables. I. Formal expressions*, Phys. Rev. **C72** (2005) 064004  
A. Fix and H. Arenhövel, *Incoherent pion photoproduction on the deuteron with polarization observables. II. Influence of final state rescattering*, Phys. Rev. **C72** (2005) 064005
- [Fri77] J. L. Friar, *Low-energy theorem for Compton scattering and the Drell-Hearn-Gerasimov sum rule: Exchange currents*, Phys. Rev. **C16** (1977) 1504
- [Fub65] S. Fubini, G. Furland and C. Rossetti, *A Dispersion Theory of Symmetry Breaking*, Nuovo Cim. **40** (1965) 1171

- [Fuc95] A. Fuchs, Ph.D. Thesis, University of Tübingen, 1994.
- [Ger66] S. B. Gerasimov, *A sum rule for magnetic moments and the damping of the nucleon magnetic moment in nuclei*, Sov. J. Nucl. Phys. **2** (1966) 430
- [Gin50] V. L. Ginzburg and L. D. Landau, *On the theory of superconductivity*, Zh. Eksp. Teor. Fiz. **20** (1950) 1064
- [Goe02] St. Goertz, W. Meyer and G. Reicherz, *Polarized H, D and  $^3\text{He}$  Targets for Particle Physics Experiments*, Nucl. Phys. **49** (2002) 403
- [Goe04a] St. Goertz, *The dynamic nuclear polarization process*, Nucl. Ins. Meth. **526** (2004) 28
- [Goe04b] S. Goertz, W. Meyer and G. Reicherz, *Polarized solid targets and techniques. Proceedings, 9th International Workshop, Bad Honnef, Germany, October 27-29, 2003*, Nucl. Instr. Meth. **A526** (2004) 1
- [Gol75] M. Goldman, J. Mag. Res. **17** (1975) 393
- [Hai84] J. Haidenbauer and W. Plessas, *Separable representation of the Paris nucleon-nucleon potential*, Phys. Rev. **C30** (1984) 1822
- [Hal96] S. J. Hall et al., *A focal plane system for the 855 MeV tagged photon spectrometer at MAMI-B*, Nucl. Instr. Meth. **A368** (1996) 698
- [Han84] K. Hänssgen and S. Ritter, *The Monte Carlo code decay to simulate the decay of baryon and meson resonances*, Comp. Phys. Comm. **31** (1984) 411
- K. Hänssgen and J. Ranft, *The Monte Carlo code HADRIN to simulate inelastic hadron-nucleon interactions at laboratory energies below 5 GeV*, Comp. Phys. Comm. **39** (1986) 37
- K. Hänssgen and J. Ranft, *The Monte Carlo code NUCRIN to simulate inelastic hadron-nucleus interactions at laboratory energies below 5 GeV*, Comp. Phys. Comm. **39** (1986) 53
- [Han98] O. Hanstein et al., *Multipole analysis of pion photoproduction based on fixed  $t$  dispersion relations and unitarity*, Nucl. Phys. **A632** (1998) 561
- [Hei00] E. Heid, *Erste Untersuchungen zur Messung helizitätabhängiger  $\gamma\text{N}$ -Wirkungsquerschnitte für das GDH-Experiment*, Ph.D. Thesis, University of Mainz, 2000.
- [Her76] H. Herminghaus et al., *The design of a cascade 800-MeV normal conducting C.W. racetrack microtron*, Nucl. Instr. Meth. **138** (1976) 1

- [Her89] H. Herminghaus, *Bau und Betrieb von MAMI, Arbeits- und Ergebnisbericht 1987-1989*, SFB 201, 1989.
- [Hol01] H. Holvoet, *Study of the helicity dependence of double pion photoproduction on the proton*, Ph.D. Thesis, University of Gent, 2001.
- [Isv93] V. Isbert, *Photodésintégration de l'  $^3\text{He}$  entre 200 et 800 MeV*, Pd.D. Thesis, DAPHNIA/SPhN 93 51, 1993.
- [Jah05] O. Jahn, *Measurement of the Helicity Dependence of Deuteron Photodisintegration for Photon Energies below 450 MeV*, Ph.D. Thesis, University of Mainz, 2005.
- [Kop86] K. Koptzki, *Einführung in die Festkörperphysik*, Teubner, 1986.
- [Kro54] N. M. Kroll and M. A. Ruderman, *A Theorem on Photonmeson Production near Threshold and the Suppression of Pairs in Pseudoscalar Meson Theory*, Phys. Rev. **93** (1954) 233
- [Kru99] B. Krusche, *Single and double  $\pi^0$ -photoproduction from the deuteron*, Eur. Phys. J. **A6** (1999) 309
- [Lag77] J. M. Laget, *The effect of pion rescattering through the  $\Delta(1236)$  on the  $\gamma D \rightarrow pp\pi^-$  reaction for high nucleon momentum*, Phys. Lett. **B68** (1977) 58
- [Lag78] J. M. Laget, *Electromagnetic properties of the  $\pi NN$  system (III): The  $\gamma d \rightarrow pn$  reaction*, Nucl. Phys. **A312** (1978) 265
- [Lag82] J. M. Laget, *Pion photoproduction on few-body systems*, Phys. Rev. **69** (1981) 1
- [Lan04] B. Lannoy, *Experimental verification of the Gerasimov-Drell-Hearn sum rule*, Ph.D. Thesis, University of Gent, 2004.
- [Lang04] M. Lang, *Aufbau des GDH-Experiments und Messung der Helizitätabhängigkeit von  $\vec{\gamma}\vec{p} \rightarrow p\pi^+\pi^-$  von der Schwelle bis 800 MeV*, Ph.D. Thesis, University of Mainz, 2004.
- [Lax52] M. Lax and H. Fechbach, *Photoproduction of Mesons in Deuterium*, Phys. Rev. **88** (1953) 509
- [Leh95] F. Lehar et al., *The movable polarized target as basic equipment for high energy spin physics experiments at the JINR-Dubna accelerator complex*, Nucl. Instr. Meth. **A356** (1995) 58



- [Lev96] M. I. Levchuk, V. A. Petrun'kin and M. Schumacher,  $\pi^0$  photoproduction on quasi-free neutrons in the reaction  $\gamma d \rightarrow \pi^0 np$  in the  $\Delta$  region, *Z. Phys.* **A355** (1996) 317
- [Lev00] M. I. Levchuk, M. Schumacher and F. Wissmann, *The inclusive reaction  $d(\gamma, \pi)NN$  in the first resonance region*, nucl-th/0011041, (2000)
- [Log00] A. Loginov, A. Sidorov and V. Stibunov, *Effect of rescattering on polarization observables of the reaction  $\gamma d \rightarrow pp\pi$  in the delta-resonance region*, *Phys. Atom. Nucl.* **63** (2000) 391
- [Lon51] H. London, *Proc. Int. Conf. on Low Tem. Phys.*, Oxford (1951) 157
- [Lou74] O. V. Lounasmaa, *Experimental Principles and Methods Below 1K*, Academic Press, 1974.
- [Mah99] T. Mahmoud, *Inbetriebnahme und Test des DAPHNE-Kryo-Targetsystems zur Messung der  $\eta$ -Photoproduktion an flüssigem Helium 3*, Diploma Thesis, University of Mainz, 1999.
- [MAID] D. Drechsel, O. Hanstein, S. S. Kamalov and L. Tiator, *A Unitary Isobar Model for Pion Photo- and Electroproduction on the Proton up to 1 GeV*, *Nucl. Phys.* **A645** (1999) 145  
available at <http://www.kph.uni-mainz.de/>
- [Mar03] M. Martínez Fabregate, *Setup and test of a 70 GHz microwave apparatus for a polarized target*, Diploma Thesis, University of Mainz, 2003.
- [Mou04] M. Mouahid, *Aufbau und Test einer Vakuumapparatur für die Vorkühlstufen des  $^3\text{He}/^4\text{He}$ -Mischkryostaten eines polarisierten Targets*, Diploma Thesis, University of Mainz, 2004.
- [Mur93] L. Murphy, *Double Pion Photon Production on Single Nucleons from Threshold up to 780 MeV*, Ph.D. Thesis, DAPHNIA/SPhN 93 49, 1993.
- [Neg66] B. S. Neganov, N. S. Borisov and M. Yu. Liburg "Frozen Spin" Polarized Target, *JETP* **50** (1966) 1445
- [Neg68] B. S. Neganov, *Vestn. Akad. Nauk SSSR* **12** (1968) 49
- [Nii76] T. O. Niinikoski and F. Udo, "Frozen Spin" Polarized Target, *Nucl. Instr. Meth.* **134** (1976) 219
- [Noz90] S. Nozawa, B. Blankleider and T. Lee, *A dynamical model of pion photoproduction on the nucleon*, *Nucl. Phys.* **A513** (1990) 459

- [Ols59] H. Olsen and L. C. Maximon, *Photon and Electron polarization in High-Energy Bremsstrahlung and Pair Production with Screening*, Phys. Rev. **114** (1959) 887
- [Ols75] M. G. Olsson and E. T. Osypowski, *A pole model calculation of the photoproduction multipoles in the  $\Delta(1220)$  region*, Nucl. Phys. **B87** (1975) 399
- [Ols78] M. G. Olsson and E. T. Osypowski, *Vector-meson-exchange and unitarity effects in low-energy photoproduction*, Nucl. Phys. **D17** (1978) 174
- [Ove53] A. W. Overhauser, *Polarization of Nuclei in Metals*, Phys. Rev. **92** (1953) 411
- [Ped98a] P. Pedroni, *Holes in  $\varphi$  and other geometrical corrections*, Internal Note, 1998
- [Ped98b] P. Pedroni, *Simulation of the inelastic hadron collisions below 5 GeV: a modification of the GEANT3 package*, INFN/BE-88/3, 1998
- [Uso04] Y. Usov, *Frozen spin solid targets developed at JINR Dubna*, Nucl. Instr. Meth. **A526** (2004) 153
- [Pob96] F. Pobell, *Matter and Methods at Low Temperatures*, Springer-Verlag Berlin Heidelberg, 1996.
- [Pre01] I. Preobrazhensky, *Untersuchung der Helizitätabhängigkeit der Einpionphoproduktion am Proton*, Ph.D. Thesis, University of Mainz, 2001.
- J. Ahrens et al., *Helicity Dependence of  $\gamma p \rightarrow N\pi$  below 450 MeV and Contribution to the Gerasimov-Drell-Hearn Sum Rule*, Phys. Rev. Lett. **84** (2000) 5950
- [Rei95] G. Reicherz et al, *The Bonn polarized target NMR-system*, Nucl. Instr. Meth. **A356** (1995) 74
- [Roc02] H. Rochholz, *Entwicklungsarbeit für einen Frei-Elektronen-Laser auf der Basis des Smith-Purcell-Effectes im infraroten Spektralbereich*, Diploma Thesis, University of Mainz, 2002.
- [Roh04] C. Rohlof, *Entwicklung polarisierter Targets zur Messung der Gerasimov-Drell-Hearn Summenregel an ELSA*, Ph.D. Thesis, University of Bonn, 2004.
- [Ros57] E. M. Rose, *Elementary Theory of Angular Momentum*, Wiley New York, 1975
- [Ros05] T. A. Rostomyan, *Experimental verification of the GDH sum rule on the neutron*, Ph.D. Thesis, University of Gent, 2005.
- [Rov02] C. Rovelli, *Contributo ed importanza dei canali parziali nella regola di somma di Gerasimov Drell Dearn*, Diploma Thesis, University of Pavia, 2002.

- [Sac91] Saclai, *Automatisme DAPHNE mode d'emploi pour le vide et la cryogenie*, Internal paper.
- [Sai69] S. Saito, *Low-energy Theorem for Compton Scattering*, Phys. Rev. **184** (1969) 1894
- [Sau96] M. Sauer et al., *The ring shaped plastic scintillator detector STAR for forward angle reconstruction*, Nucl. Inst. Meth. **A378** (1996) 143
- [Sch65] T. J. Schugge and C. D. Jeffries, *High Dynamic Polarization of Protons*, Phys. Rev. **138** (1965) A1785
- [Sch85] W. Schweiger, J. Haidenbauer and W. Plessas, *Separable model for the antinucleon-nucleon elastic and annihilation interaction*, Phys. Rev. **C32** (1985) 1261
- [Sch96] R. Schmidt, H. Arenhövel and P. Wilhelm, *Quasifree pion photoproduction on the deuteron in the  $\Delta$  region*, Z. Phys. **A355** (1996) 421

